LIFT AND DRAG OF YAWED ELLIPTICAL CAVITIES WITH VARYING DEPTHS

(Spine Title: LIFT AND DRAG OF YAWED ELLIPTICAL CAVITIES)

(Thesis format: Monograph)

by

Thomas Hering

Graduate program in Engineering Science

Department of Mechanical & Materials Engineering

A thesis submitted in partial fulfillment of
the requirements for the degree of
Master of Engineering Science

Faculty of Graduate Studies
The University of Western Ontario
London, Ontario, Canada

THE UNIVERSITY OF WESTERN ONTARIO

FACULTY OF GRADUATE STUDIES

CERTIFICATE OF EXAMINATION

Supervisor   Examiners

_____   _____

Dr. Eric Savory   Dr. Gregory A. Kopp

                                              _____

Supervisory Committee   Dr. Anthony G. Straatman

_____   _____

                                              Dr. Chao Zhang

The thesis by

Thomas <u>Hering</u>

entitled:

Lift and Drag of Yawed Elliptical Cavities with Varying Depths

is accepted in partial fulfillment of the requirements for the degree of

Master of Engineering Science

Date_____   Dr. Liying Jiang
13 December 2006

                                              Chair of the Thesis Examination Board

ABSTRACT

The present investigation is an experimental study of low velocity turbulent boundary layer flow over cavities of elliptical planform areas. Surface pressure measurements and wake velocity measurements were carried out to examine the effects of yaw angle and cavity depth on the resulting flow regimes. Different flow regimes were identified which were highly dependent on yaw angle and cavity depth. These regimes displayed similar flow characteristics to yawed rectangular cavities. A Strong asymmetric flow regime occurred for certain yaw angles, which displayed a trailing vortex configuration at certain cavity depths. This trailing vortex configuration was associated with a high drag coefficient. A frequency analysis of the time series revealed a broad range of frequencies in the wake of the trailing vortex associated with high turbulence in that region. Depth mode resonance was observed for deep cavities, while cavity feedback resonance was not found for any of the configurations. Good agreement was found between previous studies and the current investigation.

Keywords: Cavity, elliptical, turbulent flow, boundary layer, wind tunnel, hot-wire, wake velocity, pressure measurement, flow regime, trailing vortex, asymmetry, yaw angle, cellular structure, high drag, oscillation, cavity feedback resonance, depth mode resonance.

ACKNOWLEDGEMENTS

TABLE OF CONTENTS

LIST OF TABLES

LIST OF FIGURES

LIST OF SYMBOLS AND ABBREVIATIONS

A	Dimensionless drag parameter (function of h/D)
A_{base}	Planform area of cavity
B	Dimensionless drag parameter (function of M)
c	Speed of sound
C_D	Drag coefficient
ΔC_D	Incremental drag coefficient due to cavity presence
c_f	Local skin friction coefficient
C_L	Lift coefficient
ΔC_L	Incremental lift coefficient
Cp_{mean}	Mean pressure coefficient, $(P - P_{static}) / P_{dynamic}$
Cp_{rms}	Root-mean-square pressure coefficient
D	Cavity minor axis
D'	Effective streamwise cavity length
E_a	Acquired voltage from hot-wire
E_{corr}	Temperature corrected voltage of hot-wire
f	Frequency of oscillation
F_D	Drag force
F_L	Lift force
h	Cavity depth
H	Boundary layer shape factor, δ_* / δ_θ
k_r	Real part of wave number
L	Cavity length
m	Oscillation mode number
M	Mach number
N	Mode number (positive integer)
P	Measured pressure
$P_{dynamic}$	Freestream dynamic pressure
P_{static}	Freestream static pressure

PSD	Power Spectral Density
rms	Root-mean-square, e.g. $\sqrt{\overline{u}^2}$
Re $_D$	Reynolds number based on cavity minor axis, U_oD/ν
T$_a$	Ambient temperature during acquisition
T$_o$	Reference ambient temperature
T$_w$	Wire temperature
W	Cavity width (spanwise)
U$_o$	Freestream velocity
u	Instantaneous streamwise velocity
u'	Rms value of fluctuating streamwise velocity
U	Mean streamwise velocity
u_*	Friction velocity
v	Instantaneous vertical velocity
V	Acquired voltage
x	Streamwise length coordinate
y	Vertical length coordinate
z	Lateral (spanwise) coordinate
γ	Vortex sound pulse lag-time factor
δ	Boundary layer thickness (based on $U = 0.99U_o$)
δ_*	Boundary layer displacement thickness
δ_θ	Boundary layer momentum thickness
θ	Angular coordinate
κ	Ratio of vortex convection velocity to freestream velocity
ρ	Density of air
τ	Wall shear stress
τ'	Shear stress across cavity mouth
ν	Kinematic viscosity

1 Introduction

The study of flow over cavities has been investigated since the early 1930's. As new developments in the airplane industry expanded, a need to reduce overall drag for better fuel consumption lead to the investigation of the drag of different surface irregularities (Hoerner, 1965). Surface irregularities were mostly caused by design or manufacturing constraints on different aerodynamic vehicles. These include landing gear wells, weapons bays, flap recesses, rivet depressions and recessed windows (Friesing, 1936). In the case of depressions or cavities, simple geometries were initially investigated to examine the effects of different cavity dimensions on drag. Early investigators noticed highly complex flow regimes associated with these simple shaped cavities and found them not only to depend upon geometry but also on the upstream approaching boundary layer. Gaudet and Winter (1973) concluded that "due to the complexity of the three-dimensional flow pattern within a hole, it is highly unlikely that a simple analysis will produce methods for describing all the possible combinations".

Studies of two-dimensional cavities with rectangular planform areas were examined and classic definitions of the different flow regimes with varying depth to length ratio were introduced (Charwat et al, 1961). The flow regimes not only vary with geometry but also are also strongly affected by boundary layer parameters and Mach number effects (ESDU, 2004). The change in the flow regimes result in different drag and lift forces on the structure containing the cavity. This becomes important for successful weapon deployment from bomb bays in military aircraft and drag reduction techniques. These classic definitions could be applied to cavities with different planform areas to aid in the understanding of the effects of geometry and boundary layer parameters on the drag and lift.

Later studies identified self sustained oscillations within rectangular cavities, which were created by a complex feedback system set up within the cavity. Investigators developed different empirical models in order to be able to predict the frequencies of these oscillations (Rossiter, 1966). Although these models were sometimes successful at predicting excited frequencies under certain conditions, they were unable to predict their corresponding amplitudes. Subsequently, studies where conducted to identify the

specific conditions required to set up this feedback condition within the cavity. These resonant oscillations can cause structural fatigue and have been known to increase the drag by as much as 250% (McGregor and White, 1970) when compared to a non resonating cavity. Thus, methods to suppress such oscillations have become an important field within the cavity research area in recent years. With the increased CFD work done on cavity flow regimes, simulations used in the design of different mechanisms to suppress such oscillations have also been examined.

Few investigators have examined the flow regimes and resulting drag of cavities with elliptical planform areas. An early investigation by Friesing (1936) lead to the discovery of the effect of cavity depth and aspect ratio for elliptical cavities. Friesing (1936) also noticed a peak in the resulting drag for certain cavity depths in the 1:1 elliptical cavity data, which was associated with an asymmetric flow pattern. Elliptical cavities yawed to the flow were first investigated by Savory and Toy (1993a), who noticed an increase in drag for certain yaw angles.

Although some similarities have been found between rectangular and elliptical cavity flow regimes the effect radius of curvature is not fully understood and so far only limited number of yaw angles have been investigated. The effect of wall radius of curvature has been an important parameter in producing the asymmetric flow pattern for circular cavities, thus the effects of changing the wall radius of curvature on the flow field needs to be addressed.

1.1 Aim of thesis

The main objective of this thesis is examine the flow regimes associated with yawed elliptical cavities. The resulting flow regimes will be compared to flow regimes associated with rectangular and circular cavities, which have been investigated more extensively.

The objectives of the current investigation are:

- To identify flow regimes for a 2:1 aspect ratio elliptical cavity with varying yaw angle and cavity depth.

- To relate the flow regimes back to known flow regimes associated with rectangular cavities.
- To identify a link between the large increase in drag for circular cavities at a certain cavity depth and yawed elliptical cavities.
- To examine the effects of wall radius of curvature on the resulting flow regime.
- To observe the effects of yaw angle and cavity depth on the lift and drag of elliptical cavities.
- To examine cavity resonance for yawed elliptical cavities.

1.2 Approach of the current investigation

An experimental approach was chosen to examine the proposed objectives of the current investigation. Due to the limited available data on elliptical flow regimes, a CFD approach would not have been beneficial as sufficient data is not available for comparison and verification of the simulation results. The experiments were conducted in a low speed closed loop wind tunnel with a thick boundary layer. A cavity with a 2:1 elliptical planform area was chosen for the investigation, which could be altered to study the effects of yaw angle and cavity depth. Two different experimental techniques were used to examine the flow field and resulting lift and drag of the cavity. These included pressure measurements, using pressure transducers and wake velocity measurements, using hot-wire anemometry. These techniques were found to be effective in providing sufficient information regarding the flow regimes to successfully complete the objectives of this thesis.

1.3 Organization of the thesis

The following chapter reviews the literature relevant to the current work. The classification of the resulting flow fields over nominally two-dimensional cavities is first introduced. This is followed by a discussion of the different cavity resonance

mechanisms found under certain flow conditions. The end of the chapter discusses the recent trends in cavity research.

Chapter three provides details of the equipment setup used for the experimental investigation of yawed elliptical cavities. A description of the wind tunnel facility and approaching boundary layer is introduced first. This is followed by a description of the pressure transducer and microphone set up used to examine the pressure field. A description of wake measurement apparatus is presented at the end of the chapter. The next chapter provides a detailed description of the different techniques used to convert the collected data from each of the measurements to physical quantities.

In chapter five the current findings from the different experiments is presented. The different flow regimes found for yawed elliptical cavities are discussed first which is followed by a description of the cavity oscillations found in the current study. An initial numerical study of turbulent flow over a circular cavity is presented in Appendix D, which aids in the understanding and evaluation of the resulting mean pressure data of the current experimental results.

The main conclusions and findings form the current investigation are presented in chapter six. Suggestions for future work are also included in this chapter.

1.4 Summary

This chapter discussed some of the key characteristics of cavity flows. The lack of knowledge of the flow regimes associated with yawed elliptical cavities is one of the major objectives of the current study. An overview of the organization of the thesis and major features of each chapter was outlined. The next chapter, reviews previous cavity flow research and summarises the key findings and gaps in our knowledge.

2 Literature Review

2.1 Introduction

The next section serves as an introduction into the study of cavity flows. The general flow regimes observed in two-dimensional rectangular cavity flows are discussed first. This knowledge is then applied to three-dimensional cavities in order to help explain the differences between them. Next, the different parameters and their corresponding effects on the flow regimes are introduced. This is followed by a discussion of different lift and drag characteristics of rectangular, circular and elliptical cavities. Due to their simple geometries, rectangular and circular cavities have been studied in more depth than elliptical cavities. Therefore, the gaps in the research into elliptical cavities will be explained, wherever possible, by establishing similarities to rectangular or circular cavities.

Examining the unsteady nature of cavity flows leads to a discussion on the different mechanisms, which produce oscillations within cavities. Special attention is paid to the cavity feedback oscillation mechanism. This is followed by a discussion on the requirements for this oscillation to occur.

In the following section L refers to the streamwise length of a cavity, W is the width of that cavity in the span wise direction and h is the depth of a cavity. Figure 2-1 displays these general cavity variables for a yawed rectangular cavity. As seen in Figure 2-1, a cavity at 0° yaw has its major axis normal to the flow and yaw angles range from 0° to 90° for symmetric cavities.

The following section will provide an overview of the steady and unsteady components of cavity flows which highlight the main concepts of the work presented later in the thesis.
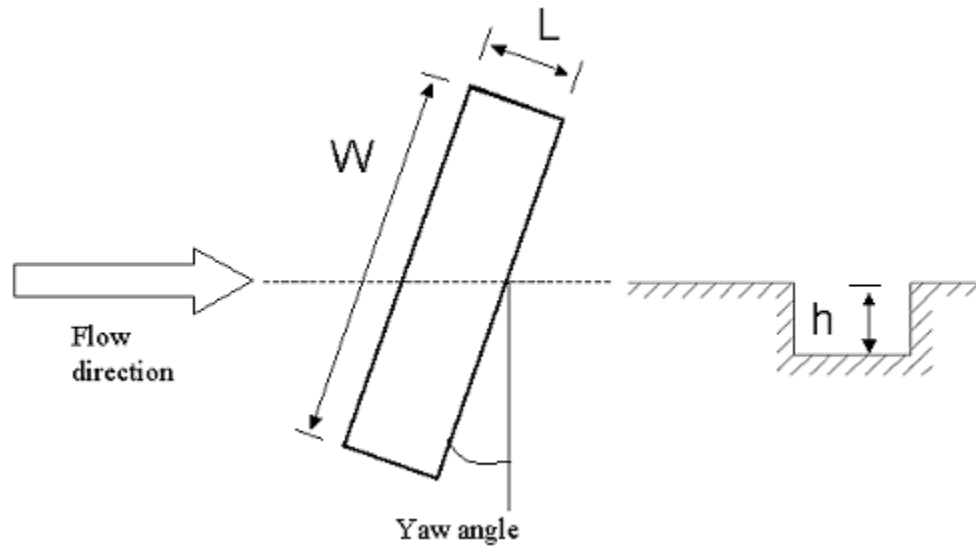
Figure 2-1 General cavity variables shown for a rectangular cavity, top view (left), side view (right)

2.2 Flow regimes of cavities

Cavity flow patterns have been observed to change as the approaching boundary layer or cavity geometry is altered. Distinct flow patterns arise for certain conditions and in general cavity flows have been classified into 2 distinct categories, "open" and "closed" cavities. These categories are based upon rectangular two-dimensional cavities, where the width (W) is much larger than the length (L) and end effects can be neglected. This classification of cavity flows was first introduced by Charwat et al (1961). Although the terms were first proposed for two-dimensional rectangular cavities, they are used to classify cavities with different planform areas.

The term "closed" cavity refers to a cavity where the shear layer separates at the leading cavity lip and impinges on the cavity base somewhere near the middle of the cavity, seen in Figure 2-2. The shear layer then separates from the cavity base in order to pass over the downstream wall of the cavity. A stagnation point exists near the cavity lip of the downstream wall (ESDU, 2004). These cavity flow types mostly occur for shallow cavities where the cavity length is much greater than the cavity depth. "Open" type cavity flows occur for deep cavities, typically L/h < 10 for rectangular cavities. For this type of flow pattern, the shear layer separates at the upstream cavity lip and bridges the cavity opening. The stagnation point occurs slightly closer to the cavity lip on the

downstream cavity wall than for closed flow (ESDU, 2004). A stable vortex forms inside the cavity volume for open type flows as noted by Roshko (1955), although different stable vortex configurations are possible depending on the h/D ratio. This captive stable vortex is driven by the separated shear layer spanning the cavity (Roshko 1955, Ukeiley and Murray, 2005). For subsonic conditions, a gradual transition zone exists between "open" and "closed" cavity flows and is usually termed "transitional" type flow, first introduced by Stallings and Wilcox (1987). For subsonic flows the transition from closed to open is more abrupt and occurs over a smaller range of L/h ratios than for supersonic flows.
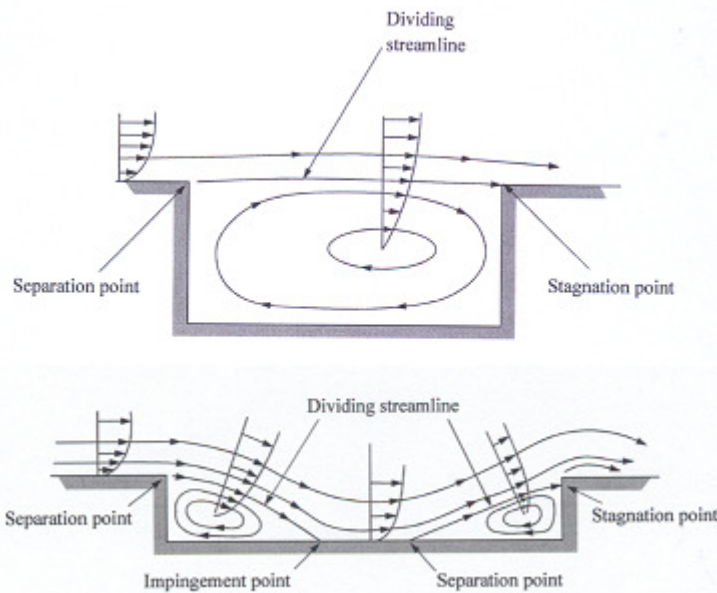
Figure 2-2 Cavity flow types: open (top), closed (bottom) (ESDU, 2004)

The transition from closed to open flow for supersonic velocities is more gradual than for subsonic conditions and two distinct transitional flow patterns can be observed. Supersonic closed flow contains two shock waves, one created by the impingement of the separated shear layer on the cavity bottom and the other created by the second impingement on the downstream cavity wall (ESDU, 2004). As the length of the cavity is decreased toward an open flow, two transitional flow patterns are seen. The first, transitional-closed, is identifiable by a single shock near the impingement region of the cavity, as seen in Figure 2-3. This single shock is a result of the two shocks moving

toward one another and coalesces as the cavity length was decreased. As the length is further decreased, the shear layer no longer impinges on the cavity floor and the single shock is broken down into expansion and compression wavelets. This flow type is termed transitional-open (ESDU, 2004). The final open cavity configuration is reached as the cavity length is further decreased and an open flow configuration, similar to subsonic conditions, is attained.
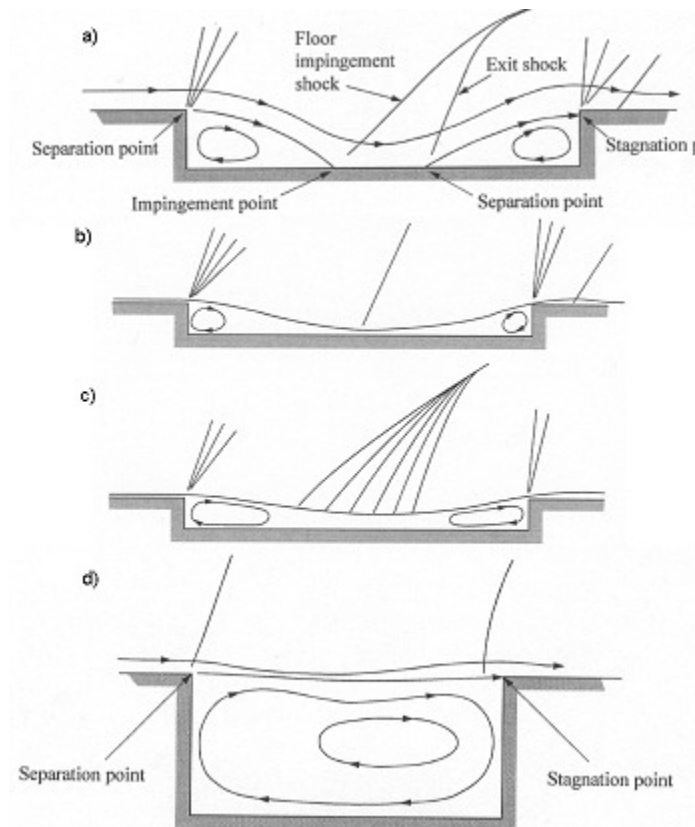
Figure 2-3 Supersonic cavity flow types: (a) closed, (b) transitional-closed, (c) transitional-open, (d) open (ESDU, 2004)

Classification of different cavity geometries into these two distinct cavity flow types is mostly based upon flow visualization techniques and pressure data. Stallings and Wilcox (1987) reported a strong correlation between flow type and mean pressure distributions on the cavity base for supersonic flows. This method of identifying cavity flows based upon cavity base mean pressure distributions was applied to subsonic flow

and may result in the proper identification of flow regime, although "the accurate interpretation of the results usually requires considerable skill and experience" (EDSU, 2004). The use of fluctuating pressure data can also aid in the identification process since discrete frequencies may exist for certain cavity flows. The idea of discrete frequencies generated by the presence of the cavity will be further explained later in this section.
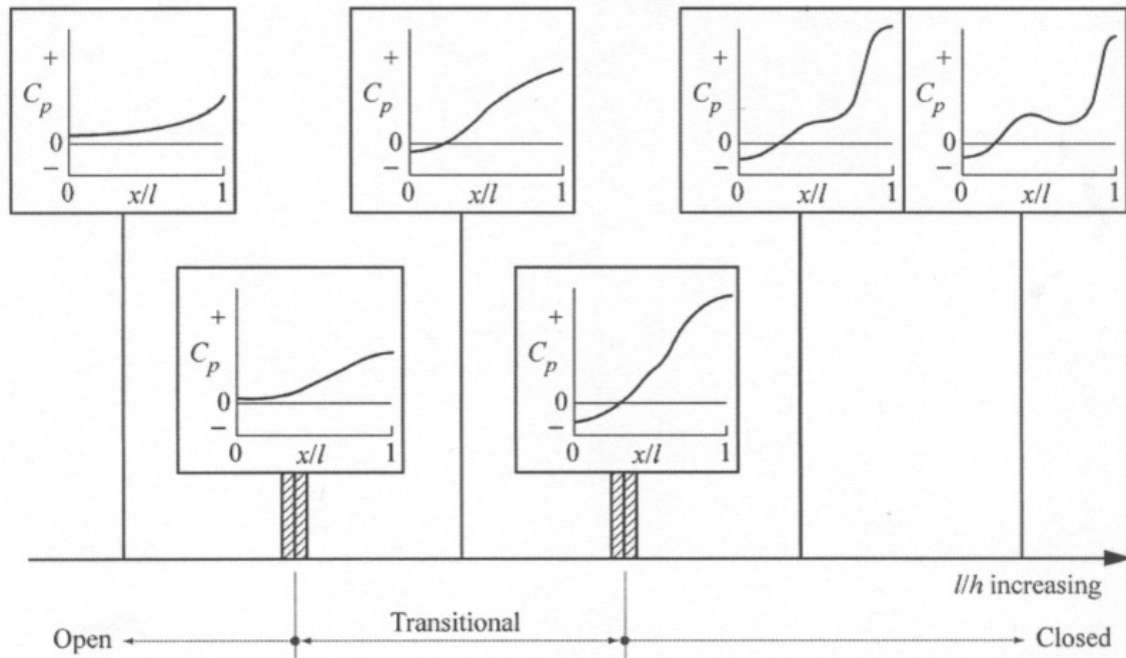
**Figure 2-4 Cavity base centreline pressure profiles as described by
Plentovich et al (1993) (image from ESDU, 2004)**

Plentovich et al (1993) studied rectangular cavities at subsonic velocities and their resulting pressure distributions along the cavity centreline in order to classify the corresponding cavity flows. This work provided important information regarding the specific pressure distributions observed for open and closed cavities along the cavity centreline. As seen in Figure 2-4, the main difference between open and closed cavities is the negative pressure near the upstream cavity wall for closed cavities. Another distinct feature of closed cavities is the high pressure region near the downstream cavity wall due to the shear layer impingement in this region. Although this work was completed for a rectangular cavities immersed in a thin boundary layer, the general trends in the pressure measurements along the centreline can be applied to other cavity geometries and boundary layer conditions.

2.2.1   Effect of cavity geometry on flow regime

Altering a specific cavity geometry has a substantial effect on the resulting cavity flow regime. The following discussion relates to rectangular cavities, although similar trends can be observed for other cavity geometries. As seen in Figure 2-4, the type of resulting flow regime is very much dependent on the length to depth ratio of the cavity. This ratio has the greatest effect on flow regimes. Plentovich et al (1993) found that for their rectangular cavities the limiting L/h ratio was 8 for open cavities and 10 for closed cavities for M = 0.20. Several other investigators of rectangular cavities have also noticed the strong dependence on the L/h ratio in determining the resulting cavity flow (Savory et al 1993b, Czech 2000).

The cavity width is an important parameter in determining if three-dimensional effects will be observed in the resulting flow field. For cavities where W/L < 1, end effects tend to dominate and a three-dimensional flow is observed (ESDU, 2004). By increasing the width of a cavity, a two-dimensional cavity flow regime could be obtained. Although this is not always the case, Maull and East (1963) noticed cell like three-dimensional flow structures in open cavities far from the cavity walls for cavities with W/L = 4.75. Maull and East (1963) identified two key features of large aspect rectangular cavities. First, the separation at the upstream cavity edge was not constant along the span of the cavity. Using oil flow visualization they noticed that the separation line, associated with the stable vortex, on the cavity base was not straight but formed a regular "wave" pattern. Second, by changing the width of the cavity they were able to establish that for certain depths the flow regime inside the cavities broke down into a number of cells. Each cell was a mirror image of the adjacent and the spanwise length of each cell remained constant for that specific h/L ratio. By increasing the width of the cavity the number of cells would be increased. These cell like structures were also observed by Czech (2000) for W/L ratios of 4.85 and 6.38 and also by Ashcroft and Zhang (2005) for W/L ratios of 4.55, 6.0 and 9.0. The effects of the cavity width was also studied by Stallings et al (1987), who noticed that small width cavities transitioned to closed flow at slightly lower L/h ratio than cavities with a larger width.

Plentovich (1990) examined the effects of free stream velocity and boundary layer thickness on resulting cavity flows. When varying the free stream velocity from M = 0.3

to M = 0.85, there was no noticeable difference in the pressure distributions on the cavity walls for closed cavities. For open cavities a lower pressure region was observed on the cavity base near the downstream wall for M = 0.3, which was not seen in the other higher velocity flows. Plentovich (1990) also altered the boundary layer thickness from $\delta/L = 0.021$ to $\delta/L = 0.014$, the results indicated that as the boundary layer thickness was decreased the pressure distributions on the cavity base near the downstream wall increased. This was most likely caused by higher velocity flow being entrained into the cavity. Plentovich (1990) only studied the boundary layer effects for closed (shallow) cavities. Although the results of Plentovich (1990) provided some insight into the effects of boundary layer thickness and free stream velocity no conclusive trends could be found. This was mostly due to the limited tests performed, as the boundary layer thickness was increased only slightly and still remained thin, $\delta/L \ll 1$. Also there were no other velocities examined between M = 0.3 and M = 0.6, the two extremes in the flow pattern.

2.3 Drag and lift of cavities

Over a wide range of studies of different cavity geometries and approaching boundary layer conditions some trends in drag coefficient have been observed and documented. Tani et al (1961) classified open and closed regimes according to their corresponding drag values. The lower drag for open cavities is mainly the result of the free shear layer spanning the cavity opening, with only the lower part of the shear layer, slower velocity region, impinging on the downstream wall of the cavity. The following section will deal mostly with open cavities and the parameters, which can affect the resulting drag.

A study of rectangular and circular cavities by Gaudet and Winter (1973), described a model where the investigators reasoned that the separated shear layer along the opening of the cavity was the main driving force behind the complex flow regimes inside cavities. They also noted that this separated shear layer is somehow related to the upstream boundary layer approaching the cavity. They used this model to explain that the drag of cavities is proportional to an effective shear stress (τ') arising from the separated shear layer spanning the cavity opening. In order to account for the upstream

boundary layer this effective shear stress was made non-dimensional by the approaching boundary layer shear stress (τ). They defined a normalized incremental or net drag coefficient ($\Delta C_D / c_f$) due to the presence of the cavity as:

$$\frac{\Delta C_D}{c_f} = \frac{\tau^{'} - \tau}{\tau}$$

Equation 2-1

where $\tau' - \tau$, is effectively the extra drag caused by the presence of the cavity and c_f is the local skin friction coefficient. The investigators have effectively accounted for the different approaching boundary layers by incorporating τ into their equation. Thus this definition has become a standard way of comparing drag results obtained from different approaching boundary layers.

McGregor and White (1970) examined boundary layer thickness and Mach number effects on overall drag of two-dimensional rectangular cavities from $M = 0.3$ to 3.0. A decrease in overall drag was noticed as the boundary layer thickness was increased for all Mach numbers, which is similar to the findings of Plentovich (1990). The effect of increasing Mach number also resulted in a lower cavity drag. Gaudet and Winter (1973) noted that the drag of a cavity was a function of the Reynolds number, Mach number and cavity depth. Examining the data for circular cavities over a wide range of velocities and cavity depths from different investigations, Gaudet and Winter (1973) showed that the data would collapse onto one single trendline by applying the following equation:

$$\frac{\Delta C_D}{c_f} = A \left(\frac{u_* D}{v} \right)^B$$

Equation 2-2

where u_* is the friction velocity, D is the diameter of the cavity and v is the kinematic viscosity of the fluid. A is dependent on the h/D ratio and Mach number while B is only dependent on the Mach number. Equation 2-2 showed that a single method for determining the drag of circular cavities existed (Young and Paterson, 1981).

2.3.1   Cavities aligned with the flow

The drag of elliptical cavities was first studied by Friesing (1936), who examined elliptical cavities with different aspect ratios with their major axes normal to the flow.

He noticed a large drag occurring for circular cavities (1:1 ellipse) at h/L ≈ 0.5, which was not observed for any of the other elliptical cavities, seen in Figure 2-5. Friesing (1936) showed that increasing the aspect ratio would decrease the resulting drag for shallow cavities, h/L < 0.8. Thus, as the elliptical cavity became more two-dimensional, the resulting drag would decrease. Friesing (1936) also found that as h/L was increased above 0.8 drag coefficient for all the ellipses converged onto a mean line. A later review of Friesing's (1936) work by Young and Paterson (1981) provided more conclusions about the drag associated with elliptical cavities. Young and Paterson (1981) noticed that if the large deviation in drag for circular cavities for h/L ≈ 0.5 was removed, all the curves of drag vs h/L for elliptical cavities displayed a similar trend. Thus, Young and Paterson (1981) concluded that the drag of elliptical cavities "may be obtained by correcting circular hole drag in some way".

Another investigation of elliptical cavities was completed by Savory and Toy (1993a). The experiments conducted examined 2:1 elliptical cavities yawed to the flow. The resulting drag was calculated using the pressure data along the cavity walls. The results were compared to compared to Friesing's (1936) data, as seen in Figure 2-5. Savory and Toy (1993a) attributed the discrepancy between the values to the difference in boundary layer thickness used in each of the investigations. Friesing (1936) used a very thin boundary layer, δ/L << 1, in his experiments while the approaching boundary layer for Savory and Toy (1993a) was thick, δ/L ≈ 4.6. The effects of the approaching boundary layer as discussed in the previous section is an important parameter in determining the resulting cavity flow regime which in effect alters the drag of the cavity. The variation in drag due to the boundary thickness was examined by Tillman (1951) for circular cavities, who noticed that thinner boundary layers produced higher drag values than thick boundary layer flow.

The large increase in drag for circular (1:1 ellipse) cavities has been attributed to asymmetric flow at this specific configuration as first observed by Friesing (1936) and studied later by several other investigators (Gaudet and Winter 1973, Hiwada et al 1983, Savory et al 1996, Dybenko 2005). Friesing (1936) noticed that as the depth of circular cavities was increased, to about h/L ≈ 0.5, a substantial change in flow characteristics occurred. The resulting flow was asymmetric along the streamwise axis of the cavity
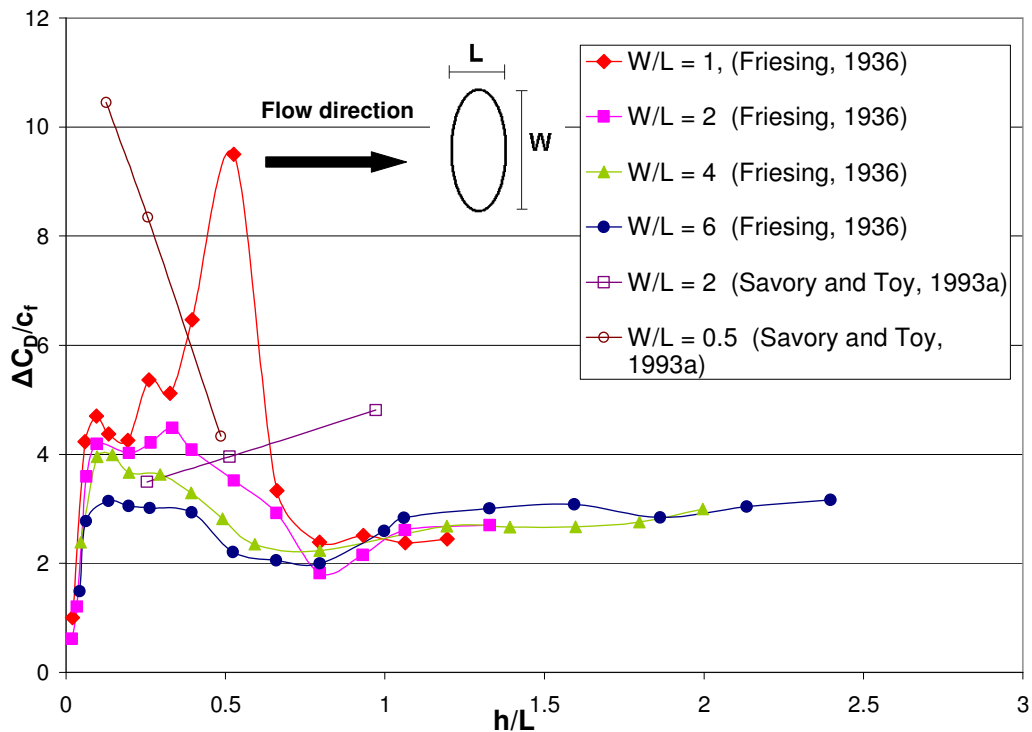
**Figure 2-5 Normalized drag coefficient of different aspect ratio
elliptical cavities**
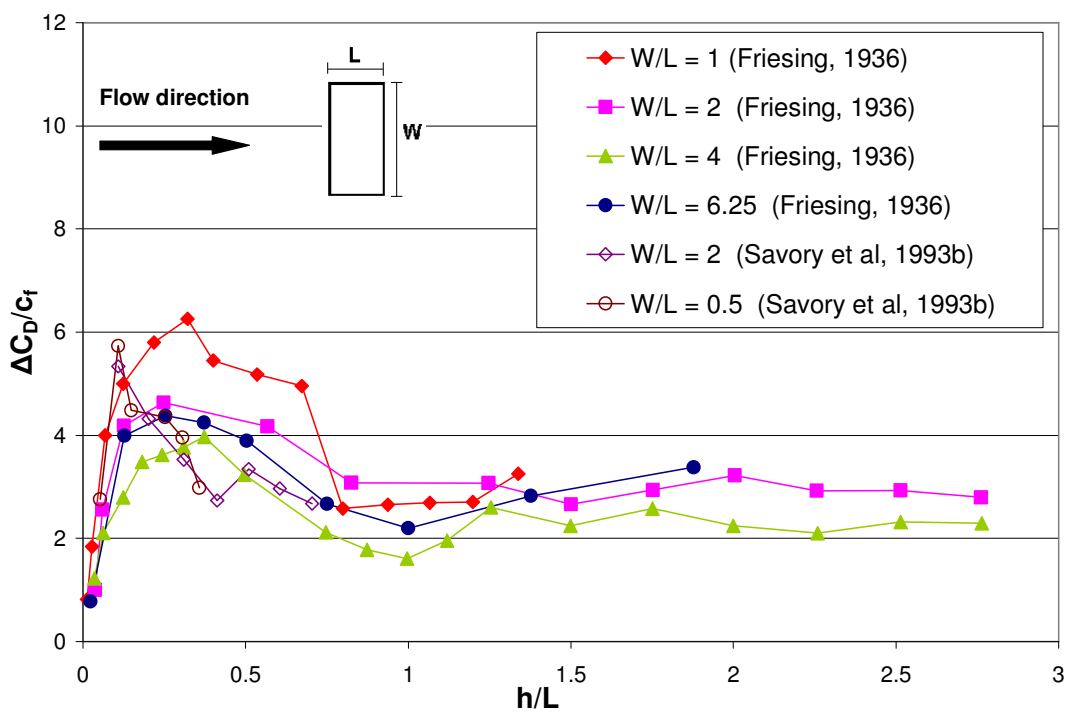
**Figure 2-6 Normalized drag coefficient of different aspect ratio
rectangular cavities**

when examining the pressure distributions along the cavity walls. The asymmetric flow is "associated with strong vorticity shedding and high drag" (Savory et al, 1996). Although Friesing (1936) conducted his experiments in a very thin boundary layer, the asymmetry has also been observed in thick boundary layers by Savory et al (1996), $\delta/D = 4.27$ and Dybenko (2005), $\delta/D = 0.72$. Therefore, the asymmetry appears to be independent of the approaching boundary layer.

Similar conclusions, as for elliptical cavities, could be drawn from Friesing's (1936) rectangular cavity data, which showed good agreement with the results obtained by Savory et al (1993b). When examining the drag vs h/L, a similar trend was seen for all aspect ratios except for the square cavity (rectangle 1:1), seen in Figure 2-6. The general shape of the curves was similar to the elliptical data in that the maximum drag occurred below h/L = 1 and the curves fluctuated around a mean line above h/L =1. The main difference was in the square cavity, where the maximum drag occurred at around h/L ≈ 0.3, as opposed to h/L ≈ 0.5 and was lower in amplitude when compared to the circular cavity.

Savory and Toy (1993a) also examined elliptical cavities with their major axis aligned with the flow, W/L = 0.5 in Figure 2-5. The results showed that as the depth was increased the drag decreased. The decrease was much less than for cavities with their major axis normal to the flow. Savory and Toy (1993a) explained that the large drag associated with shallow cavities is due to the separated shear layer impinging on the downstream cavity wall closer to the base than for deep cavities. These trends are also seen in rectangular cavities. Another study by Savory et al (1993b) was conducted for 2:1 rectangular cavities which showed similar trends to elliptical cavities when the major axis was aligned with the flow, as seen in Figure 2-7, where D' is the effective streamwise length. As previously mentioned the cavity flow regime can influence the resulting drag of the cavity. Thus the maximum drag occurred in Savory and Toy's (1993a) data for elliptical cavities at h/L = 0.125 corresponding to L/h = 8. This value is near the region of transitional flow as described by Plentovich et al (1993) in Section 2.2. This L/h configuration is the closest to a closed cavity and thus would have the largest drag associated with it. The maximum drag in the rectangular cavity study (Savory et al,

1993b) was seen at h/L = 0.05 (or L/h = 20), which is in the bounds of an open cavity regime described by Plentovich et al (1993).
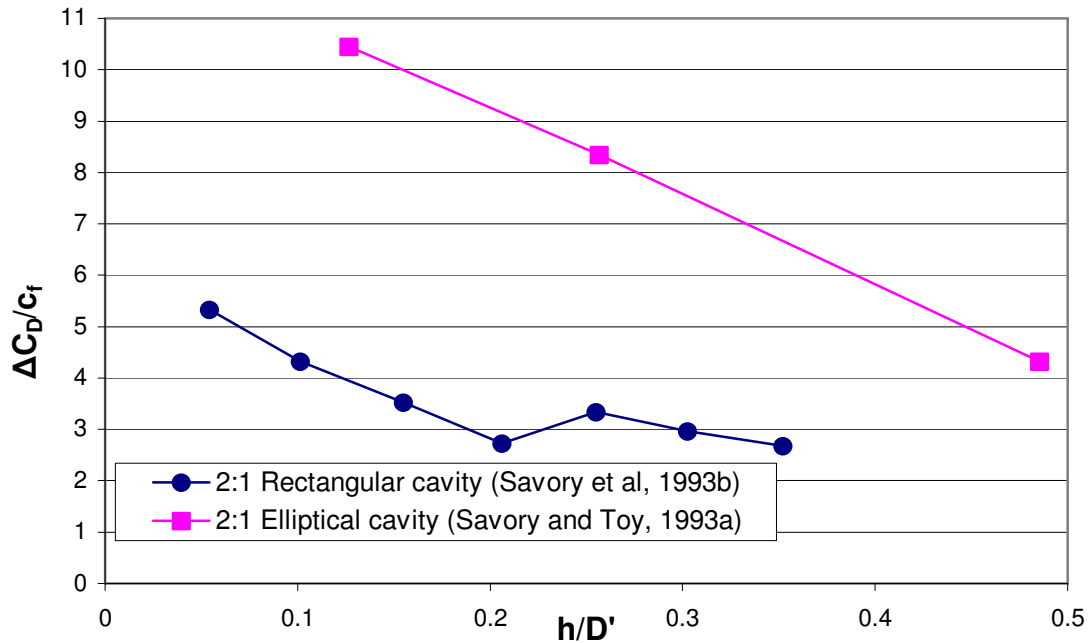
Figure 2-7 Drag of cavities with their major axis aligned with the flow (yaw 90°)

2.3.2   Cavities yawed to the flow

The yaw angle is also another important parameter, which can influence drag and flow patterns in cavities. The study by Savory et al (1993b) also examined the effects of yawing the cavity with respect to the flow direction. The investigators found that drag was not only dependent upon h/L but also on the yaw angle of the cavity. In their investigation the yaw angle was defined as the angle between the free stream direction and the cavity minor axis. Thus a cavity with its major axis normal to the flow was termed yaw 0°, while a cavity with its major axis aligned with the flow was termed yaw 90°. The investigators found that as the yaw angle increased, the mean pressure distribution would change along the cavity walls, resulting in a highly asymmetric flow. Also, higher pressure values were observed near the lip of the downstream cavity wall, indicating that higher velocity flow was being entrained and impinging on the wall.
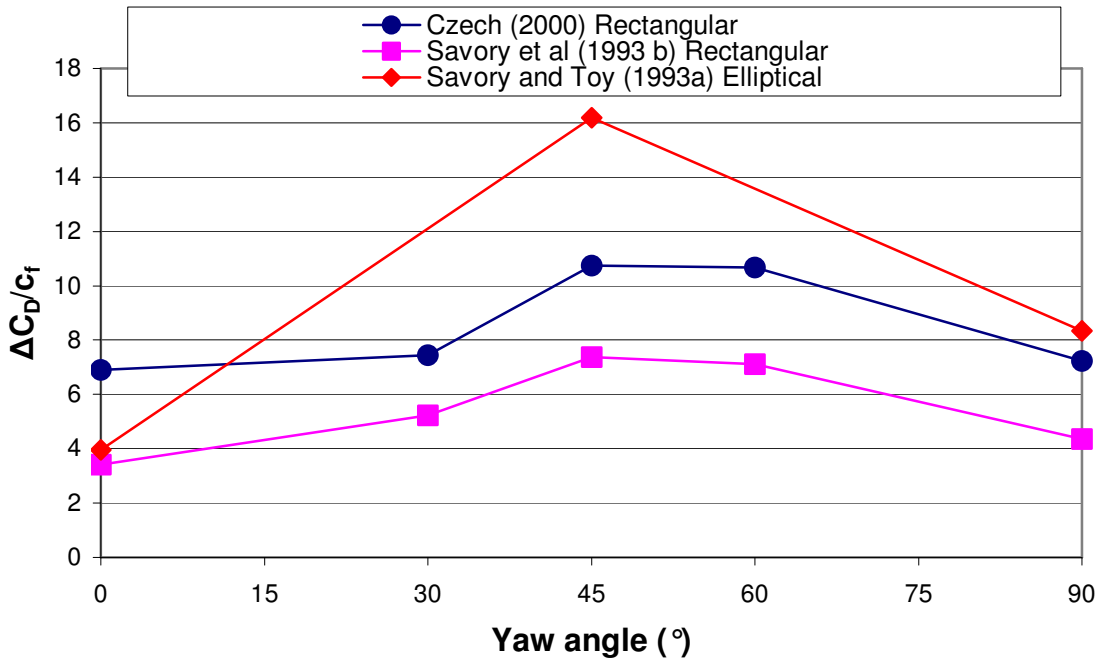
Figure 2-8 Drag of cavities at yaw (h/D = 0.5)

The resulting drag was highly dependent on the cavity depth for yawed cavities. The maximum drag occurred for cavities with h/W ≈ 0.5 at a yaw angle between 45° and 60°. Similar trends were observed by Czech (2000), who examined 2:1 yawed rectangular cavities with h/W = 0.5 using comparable boundary layer conditions to Savory et al (1993b). These trends are also apparent in elliptical cavities as observed by Savory and Toy (1993a). Although the investigation incorporated only one yaw angle, the maximum drag was found for h/W = 0.5 and yaw angle = 45° when compared to the normal and aligned configurations. This is in agreement with the trends found for rectangular cavities, seen in Figure 2-8.

2.3.3   Lift of rectangular cavities

The lift of cavities, in particular of 2:1 rectangular cavities, have only been investigated and documented in a few studies (Savory et al 1993b, Czech 2000). The lift coefficient was calculated by integrating the mean pressure values on the cavity base in both studies. A negative lift coefficient indicated a net downward force on the cavity base according to the sign convention used in both studies. Savory et al (1993b) also examined the effect of depth on lift as seen in Figure 2-9. They found that lift coefficient

was unaffected by yaw angles up to about 45° for shallow cavities (h/W <0.3). As the yaw angle increases to 90°, major axis aligned with the flow, the lift coefficient decreased even more. This is due to the effective L/h ratio increasing and the cavity flow regime becoming more closed. Thus, higher pressures in the aft cavity base region are observed for transitional cavities, as seen in Figure 2-4, which creates a larger downward force than for smaller yaw angle flows.
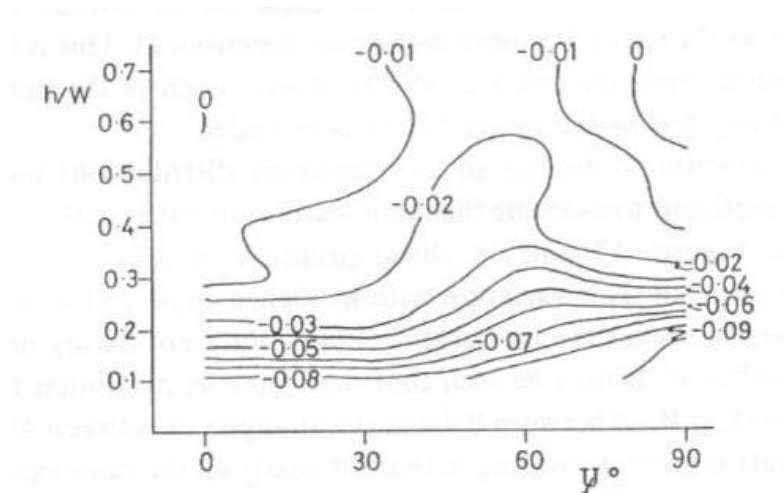
Figure 2-9 Lift coefficient of 2:1 rectangular cavities (Savory et al 1993b)

2.4 Cavity flow oscillations

Flow oscillations due to the presence of a cavity have become a very important study in recent years. Oscillations may produce resonance, which can lead to structural fatigue of the object containing the cavity.

Several different mechanisms can generate flow oscillations. For cavity flow oscillations, Rockwell and Naudascher (1978) defined 3 main categories: fluid-resonant, fluid-dynamic and fluid-elastic. The last type, fluid-elastic occurs when the walls of the cavity begin to oscillate due to the instabilities in or around the cavity. This type of resonance is not significant when the walls are made of a rigid material, which was the case in the current study. The other two main types will be explained in more detail in the following sections.

2.4.1 Fluid-resonant oscillations

Oscillations of this type arise from free-surface wave phenomenon, which are dependent on the specific cavity geometry (Rockwell and Naudascher, 1978). Shear layer instabilities at the leading edge may produce standing wave patterns inside the cavity. If the wavelengths associated with the instabilities are short enough or the corresponding cavity geometry is long enough, resonance will occur (ESDU, 2005). In rectangular cavities for example, the cavity may then resonate in width, length or depth modes depending on which length is appropriate to set up standing wave patterns.

This type of resonant frequency may be calculated for cavities according to air column resonance having both ends closed, depending if the resonance is depth, width or length mode and is given by the following equations (Sen, 1990):

$$f = \frac{Nc}{2L}$$

Equation 2-3

(both ends closed)

$$f = \frac{Nc}{4L}$$

Equation 2-4

(one end open)

where c is the speed of sound, N is an integer (mode number) and L is the length of the air column. Equation 2-4 assumes that an antinode exists at the open end of the air column. This is not the case as some sound is emitted out of the air column and perfect reflection of sound is not achieved (Sen,1990). An end correction can be applied to correct this discrepancy, to give:

$$f = \frac{Nc}{4(L+0.3D)}$$

Equation 2-5

where D is the diameter of the air column. This type of resonance is generally found in deep cavities for M < 0.2 and is termed "normal" mode resonance (Czech, 2000). Normal mode resonance occurs usually for deep cavities where L << h (ESDU, 2005). The shear layer spanning the cavity opening excites a natural or normal mode of the cavity. Usually the depth mode is excited.

2.4.2   *Fluid-dynamic oscillations*

These types of oscillations are caused by the fluctuations in the flow in or around the cavity. Some examples include velocity fluctuations in the turbulent boundary layer upstream of the cavity, which can result in broadband fluctuations to be observed on the walls of the cavity or surrounding ground plane (Dybenko, 2005). Another major source of oscillation is due to the captive vortex within the cavity (Lin and Rockwell, 2001). The frequency is dependent on the recirculating velocity of the vortex as shown by Ashcroft and Zhang (2005) using PIV measurements in a two-dimensional open rectangular cavity.

2.4.3   *Cavity feedback resonance*

This is a special type of fluid-dynamic oscillation where the free shear layer is the main driving source of the oscillations. Resonance occurs when a feedback loop develops along the cavity length, which amplifies distinct frequencies inside the cavity due to the instabilities in the free shear layer (Rockwell and Naudascher, 1978). The mechanism involved in this type of resonance is shown in the following figure:
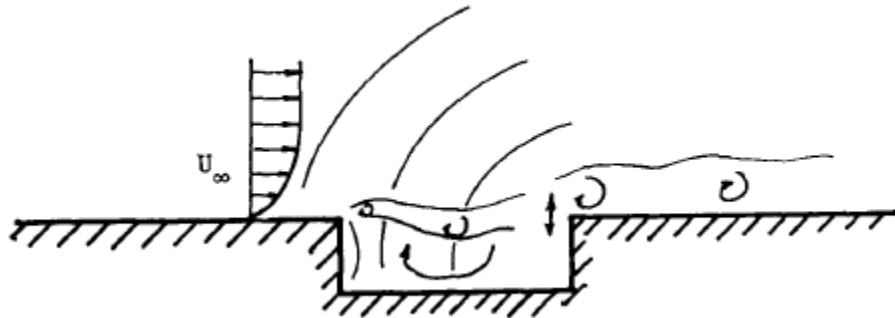
Figure 2-10 Feedback resonance visualized (Block, 1976)

According to Block (1976), the feedback loop is set up in the following manner:

i)   The free shear layer spanning the cavity impinges on the downstream cavity wall.

ii)   The stagnation pressure produces an acoustic pulse, which propagates upstream, as seen in Figure 2-10.

iii)   A pressure difference is created between a part of the acoustic wave reflected by the upstream cavity wall below the shear layer and the continuing upstream propagating acoustic wave above the shear layer.

iv)   This pressure difference causes the unstable shear layer to roll up and form a vortex, which is then shed downstream.

v)   The shed vortex impinges on the downstream cavity wall, closing the feedback loop.

Kirshnamurty (1955) was the first to notice this type of oscillations in rectangular cavities. He established that the frequency of the resonance increased with free stream velocity and decreased as the cavity length increased for rectangular cavities. He also noticed that below a certain critical cavity length, these oscillations ceased to exist. He hypothesized that at this critical length the shear layer completely bridged the cavity opening and did not impinge on the downstream cavity wall (ESDU, 2005). He found that this minimum length decreased with increasing Mach number. Hankey and Shang (1979) calculated this critical length using a simple shear layer stability analysis and found that for resonance to occur, $L \geq 6\delta$. The main idea behind this concept was that a critical level of oscillation must be present in the free shear layer in order to excite and set up this type of resonance. Although $L \geq 6\delta$ was only a rough estimate, it showed that the ratio between cavity length and boundary layer thickness had a significant effect on the existence of cavity feedback resonance.

A later study by Ahuja and Mendoza (1995) examined the effects of the upstream boundary layer on cavity feedback resonance. The investigators increased the upstream boundary layer thickness for a rectangular cavity at M = 0.4. They also noted that all cavity feedback frequencies were completely eliminated when $\delta/L > 0.066$.

Rossiter (1966) was one of the first researchers to develop an empirical equation to predict the distinct cavity feedback resonance frequencies for a rectangular cavity immersed in a turbulent boundary layer. This equation, referred to as Rossiter's equation, has become the basis in predicting cavity resonance for different boundary layer conditions and cavity geometries. The Rossiter equation is defined as:

$$f = \frac{U_0}{L} \frac{m - \gamma}{M + 1/\kappa}$$

Equation 2-6

where f is the frequency of the cavity feedback resonance, U_o is the free stream velocity, L is the streamwise length of the cavity, m is an integer (referred to as the mode number), M is the mach number of the free stream flow and κ is the ratio between the vortex convection velocity and the free stream velocity. The variable γ is a factor which accounts for the time lag between the impact of a vortex and the emission of an acoustic wave at the downstream cavity wall. Rossiter found this parameter to vary with the length to depth ratio of the cavity and found it to increase as the cavity became shallower. Rossiter found good agreement between his experimental results and the predicted frequencies.

Researchers who followed Rossiter mostly modified Rossiter's equation. Block (1976) noticed that the resonant frequency increased as the length to depth ratio increased for a given Mach number. Block (1976) assumed that the acoustic waves reflected from the cavity base were also a key component in the feedback mechanism and had to be accounted for in Rossiter's equation. This had a significant effect on predicted frequencies for velocities of $M < 0.4$.

Block's formula is equal to:

$$f = \frac{U_0}{L} \frac{m}{\dfrac{1}{k_r} + M\left(1 + \dfrac{0.514}{L/D}\right)}$$

Equation 2-7

where k_r is the real part of the wave number of the disturbance travelling downstream along the cavity length. At high Mach numbers both Block's (1976) and Rossiter's equation predict the same frequencies.

There are several key physical parameters which influence the presence and frequency of this cavity feedback resonance. These effects have all been found when examining rectangular cavities. The most important are M, δ_*/L, δ_θ/L and W/L (Rockwell and Naudascher, 1978), all defined upstream of the cavity. A more detailed study of parameters affecting the existence and strength of cavity feedback resonance was conducted by Ahuja and Mendoza (1995) for rectangular cavities. The investigators found that by decreasing W/L, giving a more three-dimensional cavity, the cavity feedback resonance frequencies were unchanged although the overall strength of the cavity noise over the entire spectra decreased by as much as 15 dB for all Mach numbers

investigated. Ahuja and Mendoza (1995) contributed this reduction in strength to the end effects of a three-dimensional cavity, as the cavity free shear layer is not being excited coherently along the cavity span. Ahuja and Mendoza (1995) also studied the critical W/L ratio required for two-dimensional cavities by placing small nylon tufts on the cavity inner surface to study flow patterns. These tufts became chaotic in nature, especially near the leading edge when the cavity width was reduced. The investigators concluded that for W/L > 1, the flow was two-dimensional over most of the cavity span. They assumed a two-dimensional flow was a requirement for cavity feedback resonance to occur.

Tracy et al (1992) studied the effects of Mach number and Reynolds number on existence and amplitude of the cavity feedback resonance. The boundary layer thickness was kept nearly constant for all the velocities tested in order to isolate Reynolds and Mach number effects. There were no noticeable effects of Reynolds number on the cavity feedback resonance for the flow velocities tested from M = 0.2 to 0.9. The resonant frequencies decreased in amplitude and became broadband as the Mach number was decreased. All cavity resonant frequencies were eliminated below M = 0.4.

A study by Tracy and Plentovich (1993) showed that the oscillations were also present in yawed cavities. The investigators found that feedback resonance existed in cavities yawed at 15° to the free stream direction, although the amplitude was reduced when compared to the aligned case. No concrete conclusions could be made about the effect of yaw angle since the maximum yaw angle studied was only 15°.

Several studies have documented a transition from feedback resonance to normal mode resonance (East 1966, Tam and Block 1978) at approximately M ≈ 0.2. Normal mode resonance is usually excited at very low Mach numbers (East, 1966) and is dependent on the depth of the cavity. Thus, a standing wave pattern is set up along the cavity depth. This limiting Ma number was verified by Tam and Block (1978) and the investigators found a gradual transition between the two modes.

The effect of rounding the upstream and downstream cavity wall edges was studied by Block (1976). Cavities with a square and a circular plan form area were compared with the length of the square cavity equal to the diameter. Figure 2-11 shows the acoustic response of the cavities at the lowest velocity tested by Block (1976),

although higher velocity flows showed similar trends. Block (1976) found two important observations regarding the effects of curved cavity wall edges on cavity acoustics. First, unlike the square cavity, the circular cavity did not display any distinct peaks, which could be attributed to feedback resonance as the square cavity did. Secondly, the circular cavity generated much more overall noise as compared to the square cavity. Block (1976) concluded that in order for strong feedback to be present the upstream and downstream walls must be parallel to each other as altering one or both of the edges significantly alters the type of mechanism generating most of the noise.
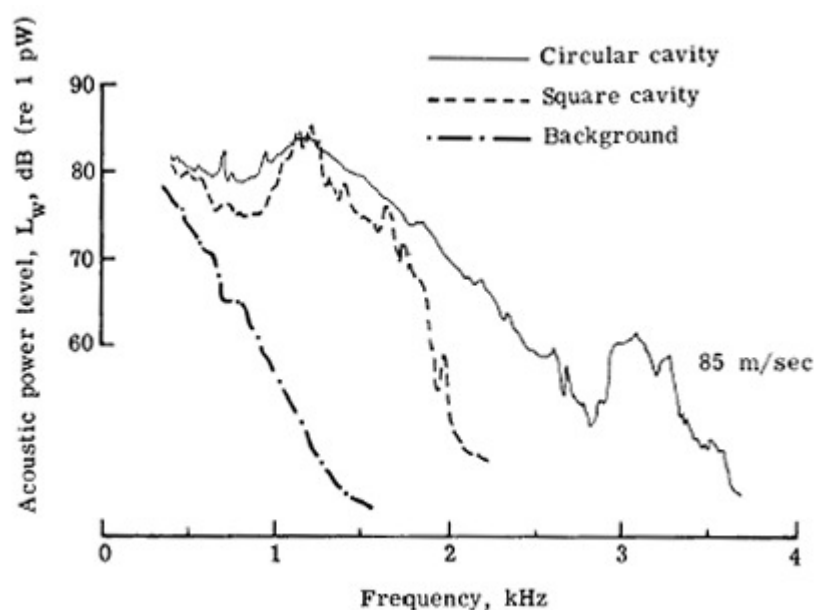
Figure 2-11 Noise comparison between a square and circular cavity with same streamwise dimension (Block, 1976)

2.5 Control of cavity oscillation

Recent research of cavities has been concentrated in the areas of control of flow induced oscillations. Most of the research concentrates on the attenuation of the cavity feedback resonance, since it is usually occurs at lower frequencies than standing wave resonance for most cavity geometries. A review of the different control mechanisms by Cattafesta (2003) indicates that all the research in this area examines mainly open type two-dimensional rectangular cavities. As mentioned in Section 2.4.3, cavity feedback

resonance has been observed to occur for two-dimensional rectangular cavities with thin upstream boundary layers above M ≈ 0.2.

The suppression techniques include open and closed feedback loops with active or passive systems. The separated shear layer is the main driving mechanism behind cavity feedback flow oscillations (Rossiter 1966, Block 1976). Therefore, the majority of suppression techniques attempt to disturb the separated shear layer in such a way as to inhibit cavity feedback resonance for that specific cavity geometry and flow condition. Sarno and Franke (1994) was the first to propose the idea of suppressing resonance by forcing the separated shear layer at much different frequencies as compared to the resonant frequencies. Most investigators attempted to force the shear layer at selected frequencies by the mass addition (pulsed jets) or actuators (piezoelectric most common). Cattafesta et al (1997) were the first to show, that forcing the shear layer at a different frequency, which is not a multiple, or near the predicted feedback resonant frequency, would attenuate the cavity resonance.

The idea of just disturbing the shear layer at no specific frequency has also been examined. Several investigators have attempted to suppress oscillations by steady mass addition into the shear layer upstream of the cavity edge (Cattafesta et al, 2003). This method indirectly increases the boundary layer thickness, which has been known to eliminate cavity feedback resonance. A disadvantage of this method is that large mass injection flow rates are required to properly eliminate unwanted resonant frequencies.

A study by Ukeiley et al (2003) examined mass addition in combination with high frequency forcing. They attempted to disturb the shear layer impingement on the downstream cavity sidewall. They accomplished this by installing a vertical row of small slender slots in the upstream cavity sidewall. Along with the mass addition from these "whistles", a high frequency oscillation is superimposed on the jet. The jets were projected at the region of shear layer impingement on the downstream wall. The investigators were successful at disturbing the feedback loop, thus suppressing cavity resonance. A lower amount of mass flow rate was required to disrupt the flow as opposed to other mass addition methods.

Passive control devices alter the characteristics of the shear layer spanning the cavity in such a way as to suppress resonant tones (Cattafesta et al, 2003). The most

common passive devices are fences or spoilers installed upstream of the cavity edge. Spoilers attempt to deflect the shear layer over the entire cavity so that impingement occurs on the ground plane downstream of the cavity. Adding a fence upstream of the cavity, which in effect increases the boundary layer thickness, has been observed to suppress cavity tones (Cattafesta et al, 2003). The disadvantage of these types of control mechanisms is the increase in the overall drag of the object containing the cavity (Rowley et al, 2005).

2.6 Cavity flow simulations

Computer simulations involving computational techniques such as DNS, DES and LES have been used to model cavity flows. Unsteady conditions are being simulated in order to predict and examine the feedback resonance set up within the cavity. Due to the complexity of simulated three-dimensional flows most of the simulations involve only two-dimensional rectangular cavities with h/L ratio ranging from about 0.5 to 0.1 (Colonius, 2001). These models are then used in combination with control theory to design and validate different control mechanisms (Hamed et al 2003, Rizzetta and Visbal 2003, Rowley et al 2005). As mentioned in Section 2.5, suppression of cavity feedback resonance is most important, since it occurs at a lower frequency than other resonant modes. Supersonic along with subsonic flow conditions are simulated in most computer codes since cavity feedback resonance occurs mostly for $M > 0.2$. The use of Particle Image Velocimetry (PIV) has allowed velocity fields to be generated inside and around the cavity. Simulated results can now be directly compared to experimental data with regard to velocity fields along with surface pressure measurements (Grace et al 2004, Ashcroft and Zhang 2005).

2.7 Summary

The previous section highlighted some key features of cavity flows. Classification of these types of flows is very important as they pertain to all types of cavities and not only to rectangular ones, from which the terms originated. Important

parameters such as drag, lift and acoustic resonance are all related to the type of flow regime of a particular cavity. In general, open cavities have been known to cause low drag and can be associated with distinct resonating fluctuations, as well as cavity feedback resonance, while closed cavities are related to higher drag and can produce broadband oscillations. The L/h ratio is the most important parameter, which determines the flow regime of a specific cavity configuration. Other parameters such as Mach number (M), upstream boundary layer thickness (δ) and cavity width (W) can also have a substantial effect on the flow regime. In general, higher velocity flows lead to lower drag while increasing the boundary layer thickness decreases the drag of that particular cavity. Changing the width of a cavity was thought to create a two-dimensional flow pattern. However three-dimensionalities may still exist in some cavities with large W/L ratios.

Cavity oscillations are classified into 3 distinct types, fluid-resonant, fluid-dynamic and fluid-elastic. Standing wave patterns related to the cavity geometry may be present, along with cavity feedback resonance. The latter is a special case of resonance where the feedback loop is set up between the downstream cavity edge and the free shear layer spanning the cavity opening. These resonant frequencies can be predicted by several empirical models. For this resonance to occur some of the following requirements must be present: cavity wall edges perpendicular to the flow direction, a thin upstream boundary layer and high velocity flows (M > 0.2). Although resonance under these conditions has been known to exist they are not limited to these specific configurations. Other parameters such as cavity width and increasing upstream boundary layer thickness have been observed to reduce the amplitude of these oscillations.

The current investigation attempts to broaden the knowledge of the flow regimes associated with elliptical cavities with regards to comparisons to rectangular and circular cavities. Although several key differences and similarities have been documented between circular, rectangular and elliptical cavities, the lack of data for different yaw and depths limits the available comparisons. Three-dimensional effects will be examined as the curvature of the cavity edge is assumed to produce a three-dimensional flow field. This is an unresolved issue as good agreement to rectangular cavities, displaying two-dimensional effects, is found for aligned configurations. The effects of yaw need to be

addressed on the resulting cavity drag and lift since non aligned external flows are common in most cavity applications.

The cause of asymmetric flow associated with high drag in circular cavities for certain depths remains an unresolved issue. Examining the wake and flow regime in yawed elliptical cavities might lead to a better understanding of the causes of this asymmetry. Along with circular cavities, yawed elliptical cavities might be a useful tool in cavity tone suppression, due to the wall radius of curvature of the cavity.

3 Experimental Details

3.1 Introduction

The following chapter describes the different experimental equipment and methodology used to obtain the data presented in the Results and Discussion chapter (Section 5). The main equipment and methodology used in the three different experiments are very similar to those developed and followed by Dybenko (2005), who performed his experiments in the same wind tunnel. Therefore, only key points and main differences will be highlighted here.

The resulting pressure field on the cavity walls and surrounding ground plane was examined using pressure transducers, which had a low frequency response. High frequency pressure oscillations within the cavity were studied using microphone measurements. Wake measurements were then completed at two different locations downstream of the cavity using hot-wire anemometry.

3.2 Wind tunnel dimensions and boundary layer parameters

A dual fan closed loop wind tunnel in the Boundary Layer Wind Tunnel Laboratory at the University of Western Ontario was used for all the experiments. The tunnel dimensions were 6500 mm (120.8D) in length, width of 611 mm (11.4D) and height of 214 mm (4.0D), where D is the length of the minor axis of the elliptical cavity. Due to the design of the closed loop tunnel, it was very difficult to mount the cavity on the tunnel floor. Therefore all measurements were conducted with the cavity situated in the tunnel roof, seen in Figure 3-1.

The boundary layer parameters and profiles were well documented by Dybenko, (2005) and were verified by the author as part of the hot-wire measurements, seen in Figure 3-2. The turbulent boundary layer was developed along the tunnel length and no tripping devices were used to create the thick turbulent boundary layer used in the current study.
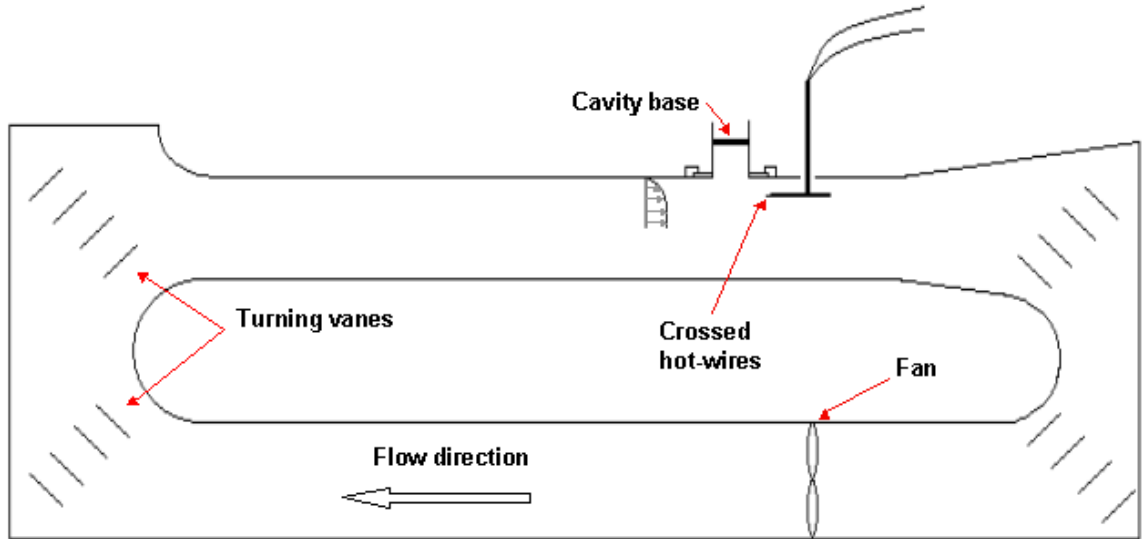
Figure 3-1 Schematic of dual fan closed loop wind tunnel

The free stream velocity (U_o) was 27 m/s (M = 0.08) and varied by ± 0.5% across the span of the tunnel for all the measurements conducted. This resulted in the Reynolds number equal to 9.07×10^4, based on the minor axis (D) of the cavity. A schematic of the

The boundary layer parameters and their corresponding ranges across the span are compared to Dybenko (2005) in the following Table:

Table 3-1 Boundary layer parameters

	Current Investigation	Dybenko (2005)	Uncertainty
δ (mm)	57.8	59.0	± 4.9
δ_* (mm)	7.8	8.0	± 0.8
δ_θ (mm)	5.7	5.9	± 0.6
u_* (m/s)	0.981	1.044	± 0.021
c_f	0.0026	0.0029	± 0.0002
H	1.37	1.36	± 0.20
u_* / U_o	0.036	0.039	± 0.001
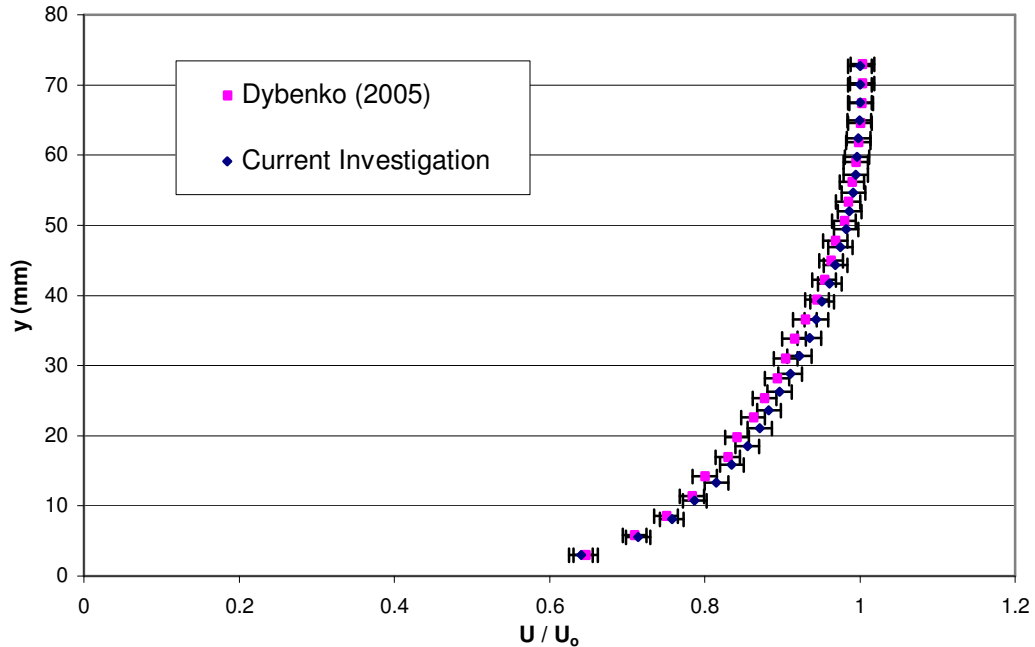
Figure 3-2 Comparison of wind tunnel boundary layer profile

3.3 Cavity geometry and dimensions

The elliptical cavity model had a 2:1 ratio of major axis to minor axis length and had the same planform area as the circular cavity studied by Dybenko (2005). The minor axis was 53.75 mm, resulting in the major axis equalling 107.5 mm. The minor axis length (D) was used as the reference length scale. The ellipse was mounted on a circular turntable, which had a radius of 390 mm (7.3D). Two models were created, one for acoustic (microphone) data and the other for pressure data. Both models incorporated a movable cavity base and the cavity was assembled by stacking several cylindrical parts on top of one another, seen in Figure 3-3. The stacking served two purposes. It reduced manufacturing costs significantly and also allowed different pressure tap configurations to be applied on the cavity sidewall for different depths.

One key component of the pressure tapped model was the special procedure followed to insert the pressure taps. The pressure taps (brass tubing) had an inner diameter of 0.8 mm and an outer diameter of 1.2 mm. This allowed the smaller diameter hole to be drilled into the model, extending to the pressure measurement surface and the outer diameter hole was only drilled approximately 3.2 mm into the model, as seen in

Figure 3-4. Therefore, pressure taps did not have to be filed smooth near the pressure measurement surface, reducing assembly time. This was especially helpful on the curved cavity sidewalls.

The pressure tap locations were carefully selected in order to capture expected regions of high pressure gradients. Thus, in order to observe the shear layer impingement point, the first tap location was 0.8 mm from the lip on the cavity sidewall. This was the limiting value of the current design. On the ground plane, the first row of taps was placed about 5 to 6 mm from the cavity lip, another region of high expected pressure gradients. The cavity sidewalls contained a pattern of 8 rows of taps evenly spaced around the circumference along half of the circumference. The ground plane and base also contained taps, but only on one side. The entire model was rotated by 180° in order to capture the entire pressure field during the experiments. The cavity base contained a single row of pressure taps along the entire major axis of the cavity, seen in Figure 3-4. This row was used to check for any changes in the flow field after the rotation was complete.
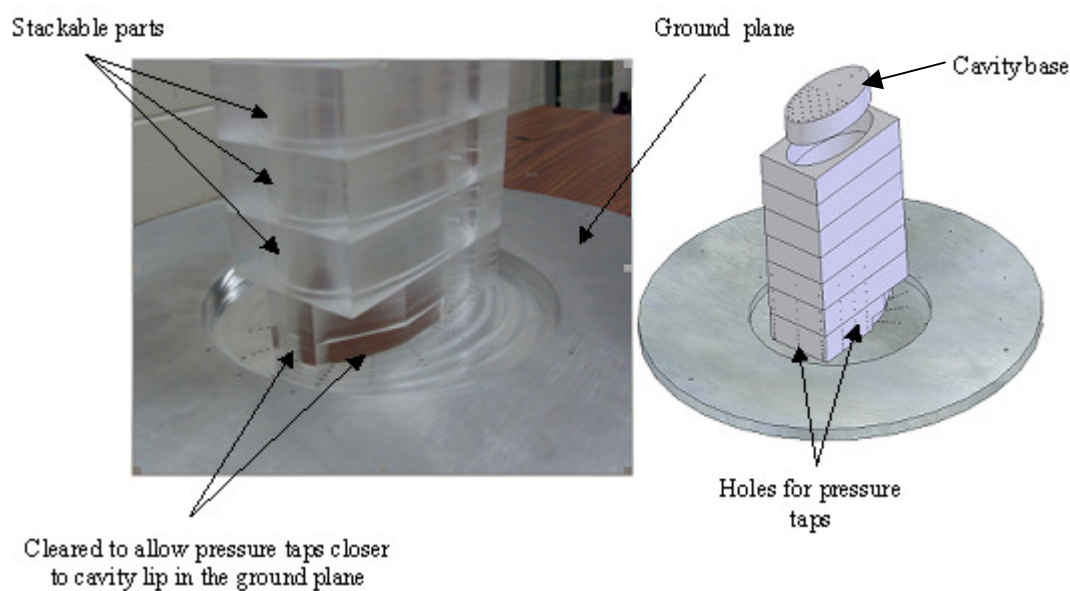
Figure 3-3 Cavity pressure tap model
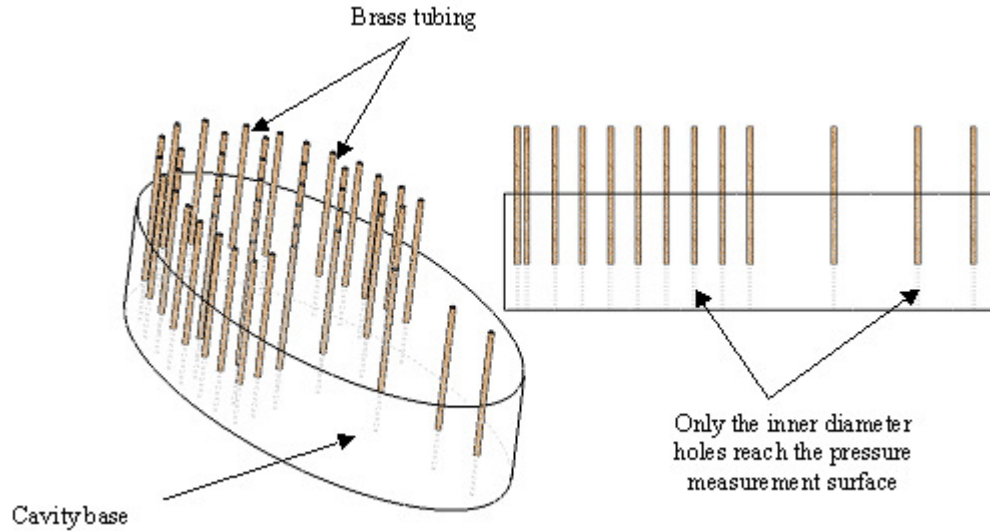
Figure 3-4 Special pressure tapping technique

The cavity base was also movable and had a clearance of less than 1mm from the cavity sidewall. A threaded rod was attached to the cavity base in order to allow transition between cavity depths, seen in Figure 3-5. Masking tape was applied to the side of the base, around the circumference to produce a good seal with the cavity sidewall. This was to ensure a tight seal, although Roshko (1955) found negligible difference in the pressure distributions in rectangular cavities between completely sealing the cavity base and with some clearance between the base and sidewall. The tape allowed for smooth transitions between the different cavity depths tested. The model was made from acrylic while the ground plane was machined from aluminium since the thickness was reduced near the cavity lip. The stackable part closest to the cavity lip was machined in a special way in order to allow access to the ground plane near the cavity lip region, seen in Figure 3-3. This was required to place pressure taps in the expected large pressure gradient regions on the ground plane. The model was pressure tapped only on one side, thus it had to be rotated 180° for each depth in order to acquire the entire pressure field data.
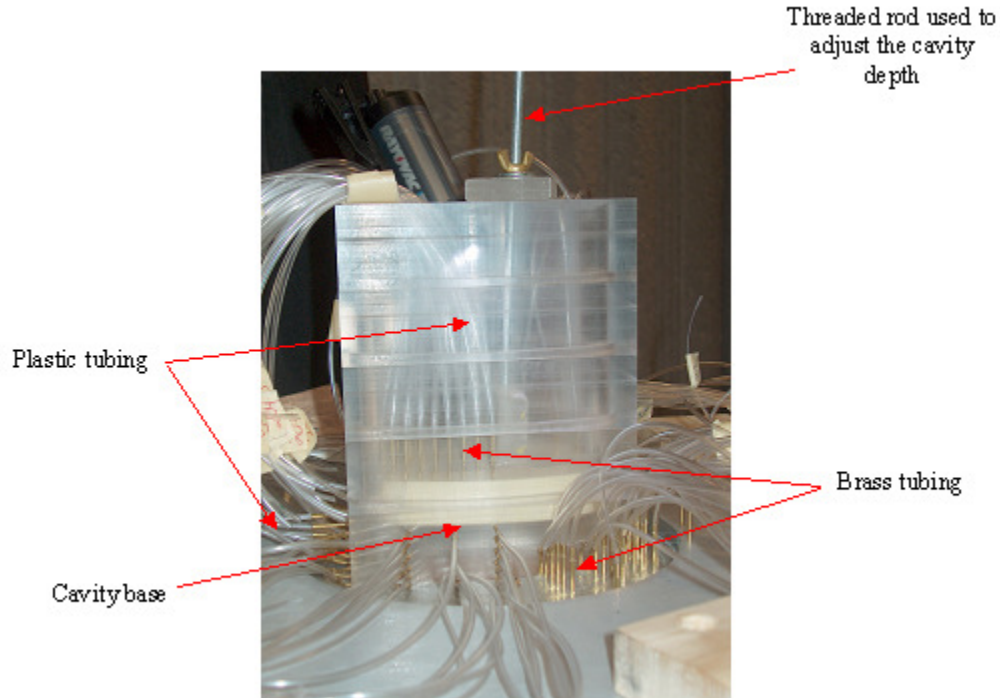
Figure 3-5 Pressure tapped model side view

A similar approach was taken for the microphone measurements. The model only included the cavity sidewall and base. The model was machined in order to be compatible with the pressure tap model ground plane, thus no new turntable was required for the microphone measurements. The microphones were embedded flush within the cavity walls. There were 14 microphones used in all, with 4 placed in the cavity base and 8 were distributed along the cavity sidewall. The concept of placing the microphones on only one side of the model and then rotating 180° was also employed. Locations of the pressure taps and microphones in their corresponding model surfaces can be found in Appendix A.

3.4 Pressure transducer measurement

The pressure tap measurements used 14 Honeywell DC001NDR4 linear differential pressure transducers and one large range digital display manometer. The 14 low range transducers were designed to measure differential pressures between ± 1" of water (250 Pa), with a linear response. 13 of the transducers were connected to the

pressure taps in the model with #16 PVC tubing, seen in Figure 3-5. The tubing was split in half and contained a brass constrictor in order to maintain the frequency response over the entire 24" tubing length. This length gave good frequency response up to about 80 Hz as noted by Dybenko (2005). Beyond this frequency attenuation of pressure fluctuations is observed. One port on each pressures transducer was left open to atmospheric pressure.

The free-stream velocity was measured by a pitot-static tube connected to a 1400 Datametrics electronic digital display manometer using #16 PVC tubing. The dynamic pressure was recorded before each 30 second sampling period and remained steady for that period. The last Honeywell DC001NDR4 linear differential pressure transducer was used to measure the static pressure in the free stream by monitoring the static pressure port of the pitot-static tube. This transducer was also referenced to atmospheric pressure. The air temperature inside the tunnel was also recorded simultaneously with the dynamic pressure by a liquid mercury thermometer with one degree intervals.

Data acquisition from the pressure transducers was accomplished by a National Instruments PCI 6052E Data acquisition card. Coordination between the sensing equipment and data acquisition was accomplished by programs written in the Labview software. The transducers were sampled in a single ended referencing mode for 30 seconds at 1000 Hz for each of the pressure measurement points. The sampling time was the same as in other investigations of thick boundary layer flow over circular cavities (Savory et al 1996, Dybenko 2005).

The sampling time was kept constant for all three different measurements completed. As previously mentioned the pressure transducers had good frequency response up to around 80 Hz and any frequencies beyond that would be attenuated. The transducers were over sampled, at 1000 Hz, in order to pick up any attenuated frequencies, which might appear in the data. The highest frequency which could be examined with the sampling rate was 500 Hz, according to the sampling-rate theorem (Wheeler Ganji, 2004). Mean, rms and instantaneous voltage values for all pressure transducers were written to a data file by Labview for each test conducted. The transducers were calibrated each day in order to account for any minor drift in the calibration constants.

3.5 Microphone measurement

The methodology followed for microphone measurements were similar to that completed for the pressure transducers and the same data acquisition equipment was used along with the same free stream monitoring setup. 14 Panasonic WM-61A miniature microphones were used. The output voltage from the microphones was analysed for their frequency content to examine acoustic frequencies inside the cavity. The detailed microphone setup and acquisition strategy is described in the master's thesis document by Dybenko (2005). The microphones were sampled at 5000 Hz for 30 seconds during the tests. The sampling frequency was chosen to coincide with the sampling frequency of the hot-wire measurements.

3.6 Crossed hot-wire measurement

Crossed hot-wire measurements were completed with the equipment outlined by Lin (2005). A Dantec Dynamics 55P61 cross wire probe was used with a 55H25 straight probe holder. The probe holder was held in place by a custom mounting rod to a Velmex 2 axis stepper motor traversing unit. The custom mounting rod allowed the straight probe holder to be moved along the streamwise direction (x-axis). The hot-wires were able to move in a three-dimensional field as the traversing mechanism moved the probe holder along the span (z-axis) and vertical directions (y-axis). A Miniature Constant Temperature Anemometry system from Dantec Dynamics, MiniCTA 54T30, was connected to the hot-wires. This system was then sampled by a National Instruments PCI-6071E card.
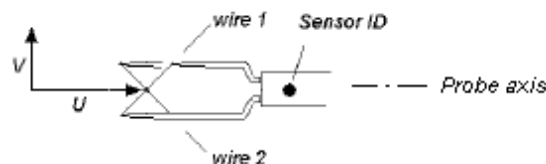
Figure 3-6 Velocity components of a crossed hot-wire (Jorgensen, 2002)

A crossed hot-wire probe is able to measure two orthogonal velocities, u and v, as shown in Figure 3-6. The coordination of the hot-wire sampling and traversing mechanism was accomplished by a Labview software program, written by PhD candidate W. Lin. The hot-wires were traversed in a plane normal to the stream-wise direction. Due to the custom mounting rod a range of planes could be traversed behind the cavity. Two planes were chosen, one at the downstream lip of the cavity and the other at 2.6D downstream of the cavity centre.
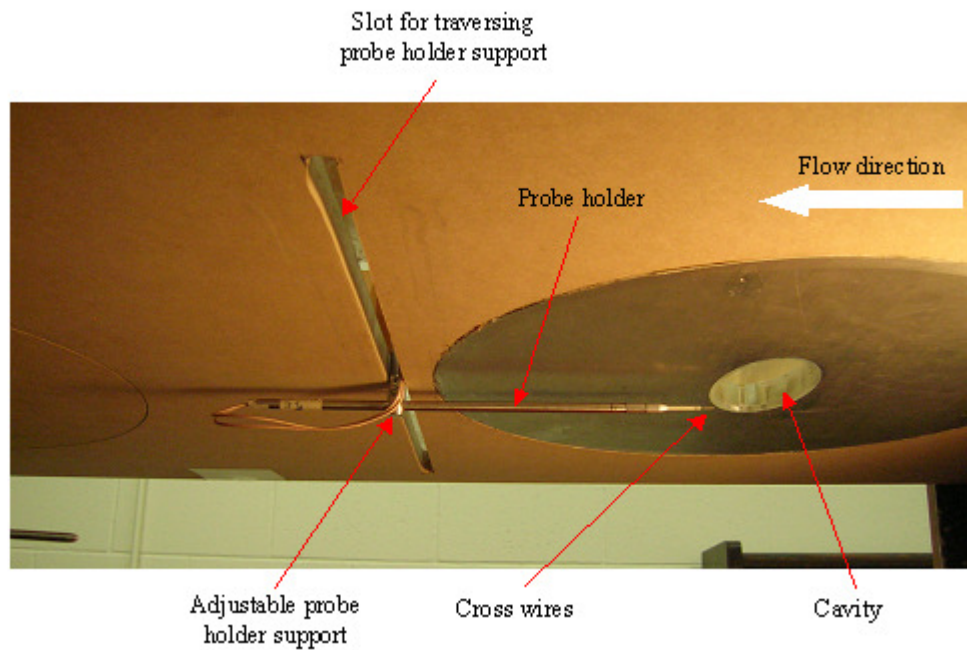
Figure 3-7 Hot-wire setup

The crossed hot-wires were sampled at a frequency of 5000 Hz for 30 seconds at each data location, thus frequencies up to 2500 Hz could be observed in the data. This high sampling frequency was chosen in order to examine high frequency oscillations in the shear layer. Data points were taken in a rectangular configuration ranging from approximately +2D to –2D in the span wise direction and from approximately 0.07D to 0.75D in the vertical direction. The nearest point in the vertical direction was 3.5 mm away from the ground plane due to the diameter of the probe holder. The hot-wire measurement setup is shown in Figure 3-7.

The free-stream velocity was measured in the same location and by the same pitot-static tube as for the pressure transducer measurements. A Honeywell

DC002NDR4 linear differential pressure transducer was used to monitor the dynamic pressure as opposed to the digital display electronic manometer, which was used in the pressure measurements. This transducer had a range of ± 2" of water (~500 Pa), also with a linear response. A liquid mercury thermometer with one degree intervals was used to monitor the free stream temperature inside the wind tunnel during the course of each test. This was necessary in order to be able to temperature correct the data during analysis.

Before any hot-wire measurements were conducted, a yaw calibration with the Dantec Streamline Yaw Calibrator Unit was completed outside of the wind tunnel. This was necessary in order to determine the angles between the crossed wires, needed later during analysis. A highly controlled velocity calibration was also completed with the Streamline Yaw Calibrator Unit with the hot-wire probe aligned with the flow for a wide range of velocities.

After these preliminary calibrations, the hot-wires were placed back into the tunnel and an *in situ* velocity calibration was completed before and after each test. Free stream temperatures were also recorded during the velocity calibrations and tests in order to be able to temperature correct later in the analysis.

3.7 Summary

This chapter outlined the main equipment and procedures used in the three different types of experiments performed. These experiments served as a basis to investigate the flow field in the cavity and its corresponding oscillations. Data from these experiments were converted to their corresponding physical quantities as described in the following chapter.

4 Experimental Measurement and Processing

4.1 Introduction

The following sections describe the methodology and data processing completed in order to generate the data seen in the results and discussion chapter (section 5) for the three different experiments. All of the programming was carried out in MATLAB (ver. 7) and surface contour plots were generated using TecPlot (ver.10)

4.2 Coordinate system for the wind tunnel

A right hand coordinate system was applied to all three conducted experiments. The resulting measurements were mapped from the tunnel roof onto the ground plane in order to be consistent with previous studies, defined by the coordinate system shown in Figure 4-1.
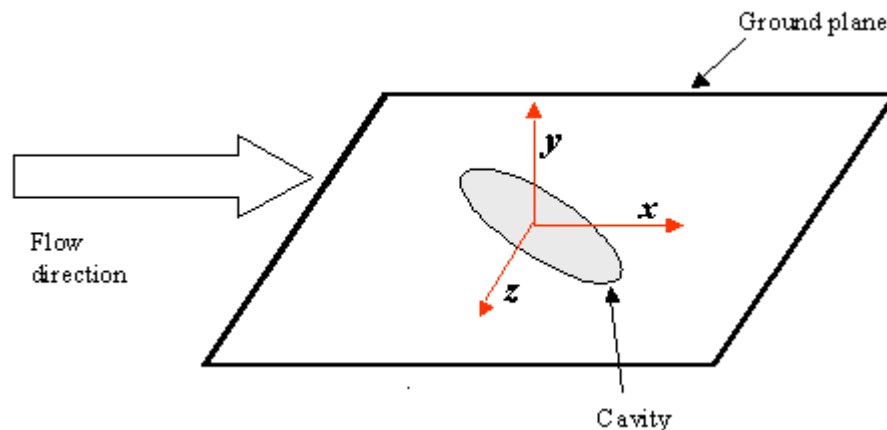
Figure 4-1 Coordinate system used in all 3 different measurements

4.3 Pressure measurements

In order to examine the effects of yaw angle and cavity depth a set of h/D ratios were examined for each yaw angle. The yaw angle increased by 15° from 0° (major axis normal to the flow) to 90° (major axis aligned with the flow). The corresponding depths tested were 0.1, 0.25, 0.35, 0.5, 0.7 and 1.0. In order to compare to other studies, for

example Dybenko (2005), the h/D ratio of 0.2 was also examined for yaw angles of 0°, 45° and 90°.

Once raw voltages were acquired they were converted to gauge pressures by a linear fit to the calibration data. The transducers were linear differential transducers, thus all gave gauge pressures referenced to atmospheric pressure inside the laboratory due to the one port being open to the atmosphere during acquisition.

Mean pressure coefficient (Cp) values were calculated by applying the following equation:

$$Cp = \frac{P - P_{static}}{P_{dynamic}}$$

Equation 4-1

where P is the pressure at the location of the pressure tap. The values of P and P_{static} were calculated by converting the voltage to pressure values from the corresponding calibration files. $P_{dynamic}$ was already in pressure form, from the display of the digital manometer. Although P and P_{static} were gauge pressures, the atmospheric pressure was not monitored since it would cancel out due to the subtraction in Equation 4-1. The Cp_{rms} (root-mean-square pressure coefficient) values were calculated by taking the rms voltage values and converting them to corresponding pressure values. This was then normalized by the mean dynamic pressure in order to create Cp_{rms}. Since the transducers were linear, the order of conversion did not matter. Converting voltages to pressure values before or after calculating mean and rms values had no effect on the final outcome.

Once the pressure coefficients were calculated for all the pressure taps they were plotted on their corresponding surfaces. A new variable, θ was created which represented a location along the circumference of the ellipse. The cavity side wall was unwrapped with the most upstream point located at θ = 0° and the furthest downstream point located at θ = 180°. For yawed cavities, the location of θ = 0° and 180° was considered to be the intersection of the upstream cavity edge with the cavity centreline, seen in Figure 4-2. The variable θ increased in a clockwise direction for all cases.

For cavities yawed with respect to the free stream direction, cavities having their major axis normal to the flow were deemed 0° while cavities with their major axis aligned with the flow were labelled as 90° yaw. The yaw angle increases from 0° to 90° in a counter clockwise rotation when looking down onto the cavity, seen in Figure 4-2.
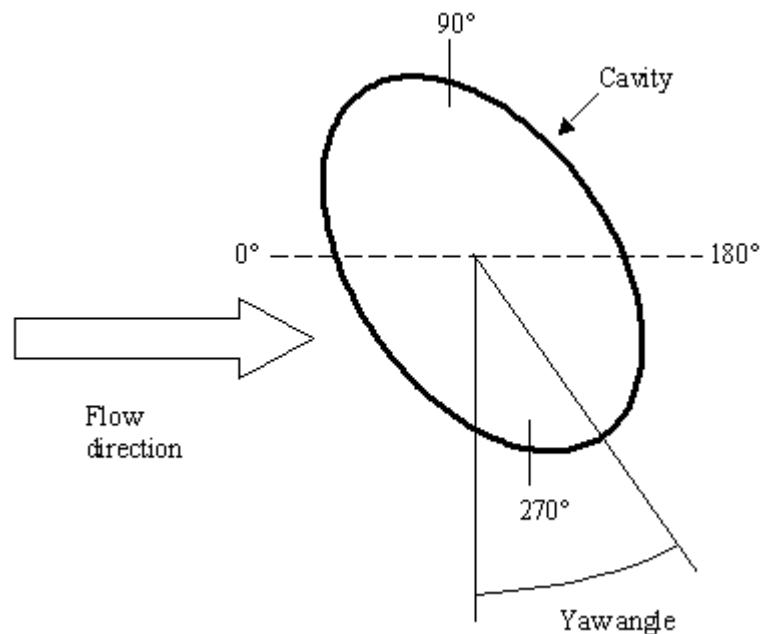
**Figure 4-2 Cavity yaw side wall variables and yaw angle definition
(top view)**

Due to manufacturing constraints, pressure taps could not be placed exactly at the cavity lip on the cavity sidewall. Therefore, to predict mean and rms Cp values in this region, a second order polynomial surface extrapolation scheme was applied using the methods described by Lancaster et al (1986). Four points from the original data set were used in the extrapolation of every new point. This method was also applied on the cavity sidewall at the depth of the cavity.

An extra set of data points was also interpolated using the same method as for the extrapolation between measured cavity sidewall taps. This was necessary as there was a lack of pressure taps along the circumference of the cavity sidewall. All the extrapolation and interpolation between sidewall taps was completed before contour plots were generated using Tecplot. Figure 4-3 shows the extrapolated and interpolated points along the cavity sidewall.

Data extrapolation was also applied to the base of the cavity in order to estimate the gaps in the data due to the positioning of the pressure taps on that surface. To show the continuous variation of pressure from the sidewall to the base, the extrapolated lowest sidewall values were placed on the cavity base as well, as shown by the red dotes in Figure 4-3. A variation of this method was carried out by Roshko (1955), who connected

Cp values along the cavity centreline between the upstream cavity wall, cavity base and downstream cavity wall to produce continuous pressure values.
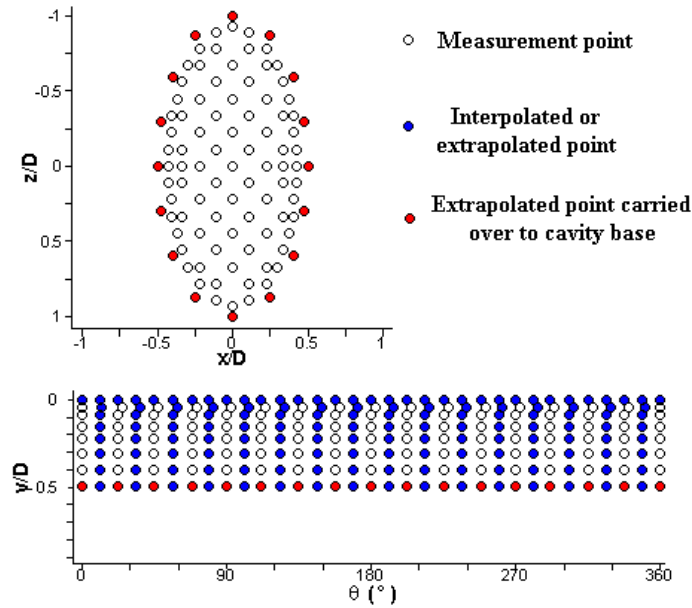
Figure 4-3 Extrapolated / interpolated points on the cavity walls

The next step was to calculate corresponding drag coefficient:

$$C_D = \frac{F_D}{\frac{1}{2}\rho U_o^2 A_{base}}$$

Equation 4-2

where F_D is the drag force, ρ is the density of air, U_o is the free stream velocity and A_{base} is the planform area of the ellipse. The lift coefficient was calculated according to:

$$C_L = \frac{F_L}{\frac{1}{2}\rho U_o^2 A_{base}}$$

Equation 4-3

where F_L is the lift force.

In order to calculate the drag force, the cavity sidewall was divided into small areas, which were then multiplied by their corresponding Cp magnitudes. This generated force coefficients, which were resolved in the streamwise direction (x-axis). Surface integration of the force coefficients was then completed. First using Simpson's rule, the force coefficients were integrated along the circumference for each row of taps. The result was then interpolated in the vertical direction using a cubic spline interpolation scheme. The interpolation values were then integrated from the base to the lip in order to

obtain the total force coefficient of the cavity in the streamwise direction. The final step was to divide the value by the planform area of the cavity, which resulted in the drag coefficient as defined by Equation 4-2. The friction drag of the cavity walls and base were not included in the drag coefficient calculation since Roshko (1966) found them to be two orders of magnitude lower than the pressure drag coefficient.

The net drag due to the presence of the cavity was then calculated according to the following equation:

$$\frac{\Delta C_D}{c_f} = \frac{C_D - c_f}{c_f}$$

Equation 4-4

where c_f is the local skin friction coefficient of the ground plane at the model location, as noted in Table 3-1.

The lift force was calculated in a similar manner as the drag coefficient, except that the force coefficients were resolved on the cavity base in the vertical (y-axis) direction. Since there was no apparent pattern of the pressure taps on the cavity base, the total area was divided into small rectangular areas, each containing one pressure tap. Thus, a lift force coefficient was calculated at each pressure tap location in the vertical direction by multiplying the pressure coefficient by its corresponding rectangular area. Addition of all of these small forces coefficients and dividing by the cavity planform area resulted in the corresponding lift coefficient.

The same concept of examining only the effect of the presence of the cavity was applied to the lift coefficient. Thus the lift coefficient obtained from setting the cavity to zero depth was subtracted from the calculated lift coefficients for all the depths measured. This produced a net lift coefficient due to the presence of the cavity:

$$\Delta C_L = C_L[cavity] - C_L[no\_cavity]$$

Equation 4-5

4.4   Microphone measurements

Raw microphone voltages were checked for their frequency content by computing the power spectral density function (PSD) of the signal. The function was created using 4096 points for the Fast Fourier transform with an overlap of 2048 points. The bin resolution was also adjusted in order to gain a better understanding of the broad band

amplitude regions. This was applied to all the measurements to examine the high frequency components in the cavity.

4.5 Crossed hot-wire measurements

Due to time constraints a limited number of yaw angles and depths were examined with the hot-wire equipment. Yaw angles of $0°, 45°$ and $90°$ were tested at three depths corresponding to h/D = 0.2, 0.5 and 0.7.

After obtaining the raw voltages from the hot-wires the first step in the analysis was to apply a temperature correction factor to the acquired voltages (E_a), defined by Jorgensen (2002) as:

$$E_{corr} = \left(\frac{T_w - T_o}{T_w - T_a} \right)^{0.5} E_a$$

Equation 4-6

where T_w is the sensor hot temperature, T_o is the reference ambient temperature, T_a is the temperature acquired during the test and E_{corr} is the resulting temperature corrected voltage of the hot-wires. The sensor hot temperature refers to the constant temperature of the hot-wires. The reference ambient temperature was chosen as the average temperature during the test performed.

The temperature correction factor was necessary since the free stream temperature inside the tunnel fluctuated by more than $\pm 0.5°C$ over the course of the *in situ* velocity calibrations (limit defined by Jorgensen, 2002). Although the effects of temperature correction did not greatly alter the values collected from the tests themselves, it did have a great effect on *in situ* velocity calibrations values. The temperature difference between the fastest and slowest velocity in the calibrations was, on average, about $5°C$. In most cases this would have resulted in a relative error of about 1.5% in terms of the streamwise velocity component without the temperature correction applied.

The next step was to convert the temperature corrected hot-wire voltages to corresponding velocities. Due to the non-linear nature of the hot-wire output a 6th order polynomial fit was used for the velocity calibration values. Since a 6th order polynomial is only valid in the range where data points exist, Jorgensen (2002) recommended a calibration range varying from 10% of the minimum velocity expected to 1.5 times the

maximum velocity expected. Due to velocity restrictions of the tunnel, this proposed range could not be attained. The upper calibration velocities were acceptable since the hot-wire would be traversed inside the boundary layer and would not measure velocities near the free stream value. Also the upper range of the calibration points included a point at $1.1U_o$. But at the lower velocity values the lowest calibration velocity attainable with the current tunnel was $0.4U_o$, which was much higher than the lowest expected velocity in the measurements. To overcome this lack of data points in the lower *in situ* velocity calibration range, a power law curve fitting scheme known as King's Law (King, 1914) was applied to extrapolate data points to lower velocity values below the lowest velocity calibrated in the tunnel. The constant n, in the King's Law power fit is highly dependent on the wire Reynolds number (Jorgensen, 2002) and therefore the four lowest calibrated velocities were used to estimate this constant for the lower velocity range. This power law fit was able to be extrapolated to the lower velocities needed in the analysis of the data and showed good agreement with the wide range calibrated velocities attained from the Streamline Calibration unit.
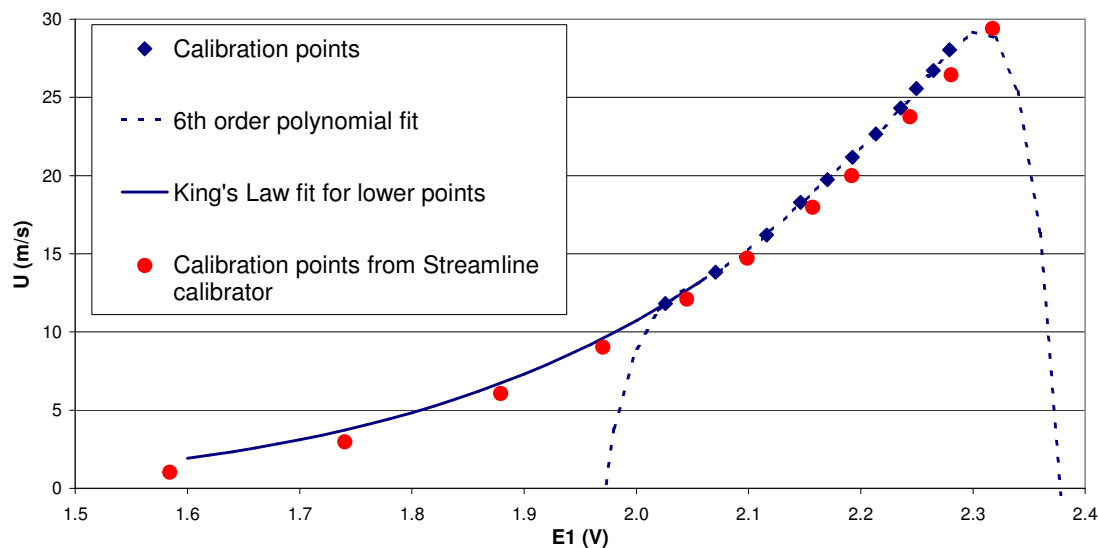
Figure 4-4 Lower velocity King's Law extrapolation

A comparison is seen in Figure 4-4, which displays the extrapolated curve along with the other calibration curves. The problem of applying a 6th order polynomial fit to the data is reiterated here as the curve is not valid in areas where no calibration points exist. The figure also shows that the King's Law extrapolation for the lower unattainable

calibration velocities follows a curve similar to the curve obtained from the high accuracy velocity calibration using the Streamline Calibration unit. The difference between the Streamline Calibration Unit and the *in situ* calibration curve is due to the error associated with measuring the velocity with the pitot-tube for the *in situ* velocity calibration.

From the yaw calibration data the angles between the wires was computed by using a least-square fit expression. By combining the velocity calibration curves and knowing the angles between the two wires, instantaneous velocity values in the two velocity direction were then calculated. The calculation procedure assumed a cosine response of the probes, thus the maximum velocity is sensed normal to each of the wires. After computing instantaneous vectors in the two axis directions, mean and turbulence quantities of interest were calculated. The free stream velocity was calculated from the dynamic pressure obtained from the linear differential pressure transducer as described in the previous section.

In order to examine the effects of the presence of the cavity, the no cavity case was subtracted from all the values obtained with the cavity in place. Also, to account for small fluctuations in the free stream velocity during the experiments, all measurement points were first normalized by the free stream velocity before the subtraction. For example, the streamwise velocity defect due to the cavity was calculated as:

$$\frac{\Delta U}{U_o} = \left(\frac{U}{U_o}\right)_{cavity} - \left(\frac{U}{U_o}\right)_{no\_cavity}$$

Equation 4-7

where U is the mean velocity in the streamwise direction and U_o is the freestream velocity.

When plotting the corresponding contour plots for the hot-wire measurements, the no-slip condition was also applied at the wall. Thus a zero velocity deficit was seen in all the measurements at the wall. This methodology was used to extrapolate the contour plots of the velocity deficit.

4.6 Error analysis

An extensive error analysis was completed by Dybenko (2005) on the experimental techniques and equipment used throughout the current investigation. The

errors associated with each measurement are displayed in Table 4-1. The microphones could not be calibrated to any known pressure and, thus, the errors associated with them represent the uncertainty in the voltage measurement. The root of the sum of the squares (RSS) method described by Wheeler and Ganji (1996) was applied in order to estimate errors associated with the calculated values. The results are summarized in Table 4-2.

Table 4-1 Errors associated with the different measurement equipment

	Pressure Coefficient(Cp)	Streamwise Velocity (u)	Frequency measurement (microphones) (V)
Based on	0.15	27 m/s	0.003 V
Total Uncertainty	± 0.0034	± 0.34 m/s	0.00038 V

Table 4-2 Resulting uncertainty associated with resulting parameters values

Parameter	$\Delta C_D / c_f$	ΔC_L	U / U_o
Resulting Total Uncertainty	± 1.35	± 0.00312	± 0.0154

4.7 Summary

The processes and details of the data collected from the three different experiments were discussed in the previous chapter. The processes described how voltage readings from each experiment were converted to their corresponding physical quantities. For all experiments wherever possible the no cavity case was subtracted, this was necessary in order to isolate the effects of the presence of the cavity on the flow in the wind tunnel. The results of each experiment are discussed in the following chapter.

5 Results and Discussion

5.1 Introduction

This chapter describes the different flow types observed for the different cavity configurations by varying the cavity depth and yaw angle. According to the limited information about elliptical cavities, the resulting drag and lift coefficient seem to resemble the trends observed for yawed rectangular cavities. It is postulated that the resulting flow field for yawed elliptical cavities will therefore be similar to those associated with rectangular cavities. Thus, the wall radius of curvature for elliptical cavities is assumed to have negligible effects on the resulting flow field. It has also been shown by the results of Friesing (1936) that the effect of aspect ratio is negligible on the resulting drag of very deep elliptical cavities. This suggests that the flow regimes for the different aspect ratios are similar for this depth range. Therefore, the effect of yawing the cavity for these depths should also be negligible, as yawing the cavity with respect to the flow is a form of changing the effective span to streamwise length ratio of the cavity. The following section describes the results from the three different sets of experiments and how they contribute to the identification of the different flow types of each of the cavity configurations examined.

5.2 Flow regimes

Surface contour plots were created to examine mean pressure coefficient distributions on all measured surfaces as mentioned in the Section 4, in order to describe some key features of the flow field. Shear layer impingement has been linked to a sudden rise in pressure on a surface, while a low pressure region may indicate shear layer separation (Adams and Johnston, 1988). As mentioned in Section 2.2, an important flow structure inside deep cavities is the existence of a captive vortex along the span of the cavity. Many investigators have found that a large scale vortical structure may be identified by looking for approximately circular low pressure regions (Dubief and Delcayre, 2000). The vortex centre of rotation is found to be located at the minimum

pressure at the centre of the circular pressure pattern, which is followed by increasing pressure in the radial direction. Examining the mean pressure contours will allow for several key observations to be made with regards to the captive vortex inside deep cavities and shear layer impingement on the downstream cavity wall as mentioned by previous investigators.

The two main parameters affecting cavity flow regimes examined in the current investigation were yaw angle and the cavity depth. The regimes were grouped according to similar trends observed in the surface pressure and the wake velocity measurements. These included location of shear layer impingement on the sidewall, existence of a captive vortex, areas of high pressure fluctuations, location and size of velocity defect in the streamwise direction and the existence of asymmetric flow. According to these
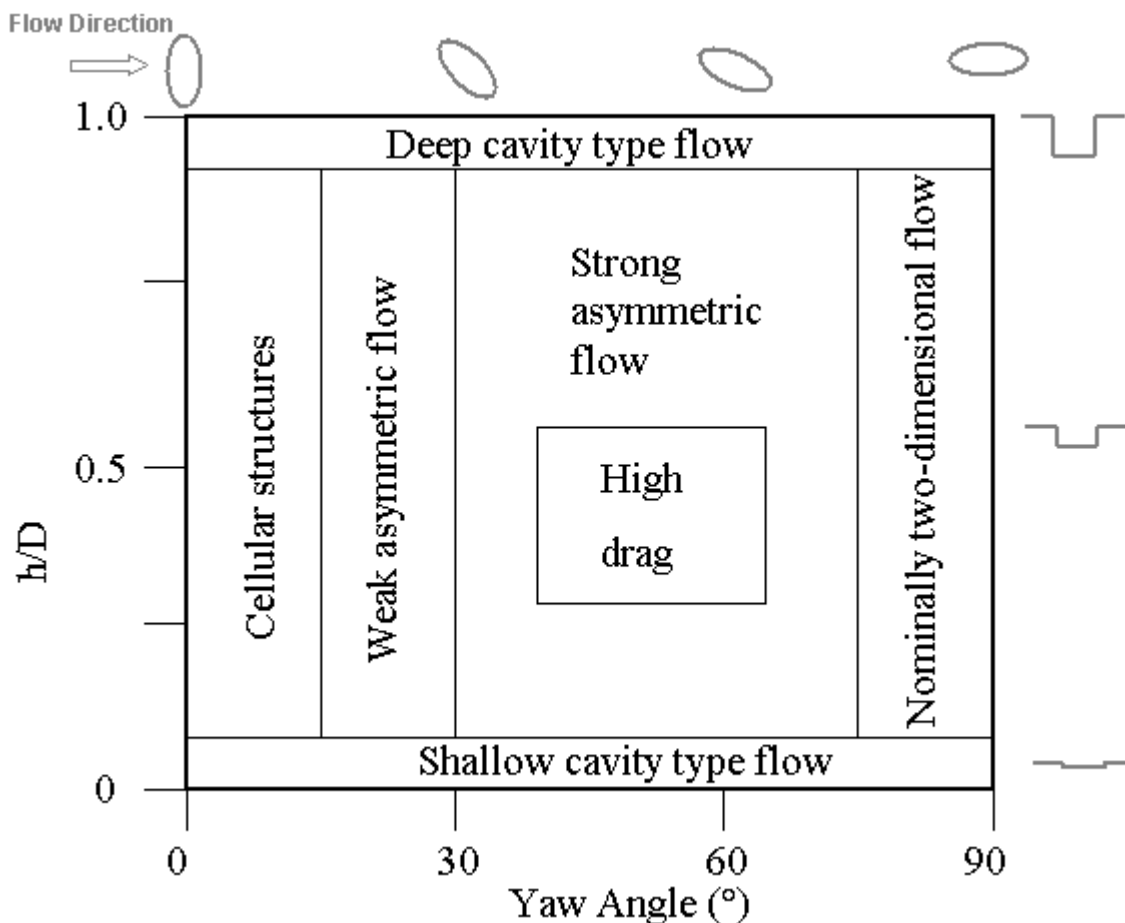
Figure 5-1 Cavity flow types observed for elliptical cavities

observations the different cavity configurations were grouped into corresponding flow regimes by approximate boundaries as indicated in Figure 5-1. These flow types will be explained in the following sections.

The extrapolation scheme used in creating the pressure contours allowed an estimation to be made along the lip of the cavity and should only by used as a prediction of the possible pressure patterns near the lip. Please note that for all the diagrams the flow direction was along the x-axis, from left to right. The mean and rms pressure coefficient distributions and wake velocity defects for all the configurations examined are shown in Appendix B and Appendix C, respectively.

5.2.1   *Nominally two-dimensional flow*

These flow types occur for cavities with their major axis aligned with the flow (yaw 90°). The flow pattern is highly two-dimensional and shows good agreement with the flow types found for two-dimensional rectangular cavities. These cavities had the longest streamwise length when compared to all the other cavity configurations. Thus they were normalized by the effective streamwise length (D') equal to 2D. This was also required in order to compare the results to previous experiments of cavities aligned with the flow.

The mean pressure distribution on the cavity walls was first compared to the work by Savory and Toy (1993a), another 2:1 elliptical cavity investigation which contains pressure distributions, as seen in Figure 5-2. The figure shows the pressure distribution for h/ D' = 0.25 (h/D = 0.5) for the two investigations. Good agreement is found between the two sets of data in terms of the overall pattern on the cavity walls. The slight differences on the cavity sidewall near the lip and depth have to do with the extrapolation scheme used to plot the contours of the current investigation. The current results seem to be consistently lower in Cp values by approximately 0.05. This constant may be a cause of the difference in the location where the static pressure used in the calculations of the Cp values was measured between the two studies. It may also be a result of the difference in the thickness of the approaching boundary layer. The current investigation was performed in a thinner boundary layer, $\delta/D = 1.08$ as opposed $\delta/D = 4.57$ used by

Savory and Toy (1993a). The thinner boundary layer would result in a larger Cp value as higher velocity fluid would be entrained into the cavity from the shear layer spanning the cavity.
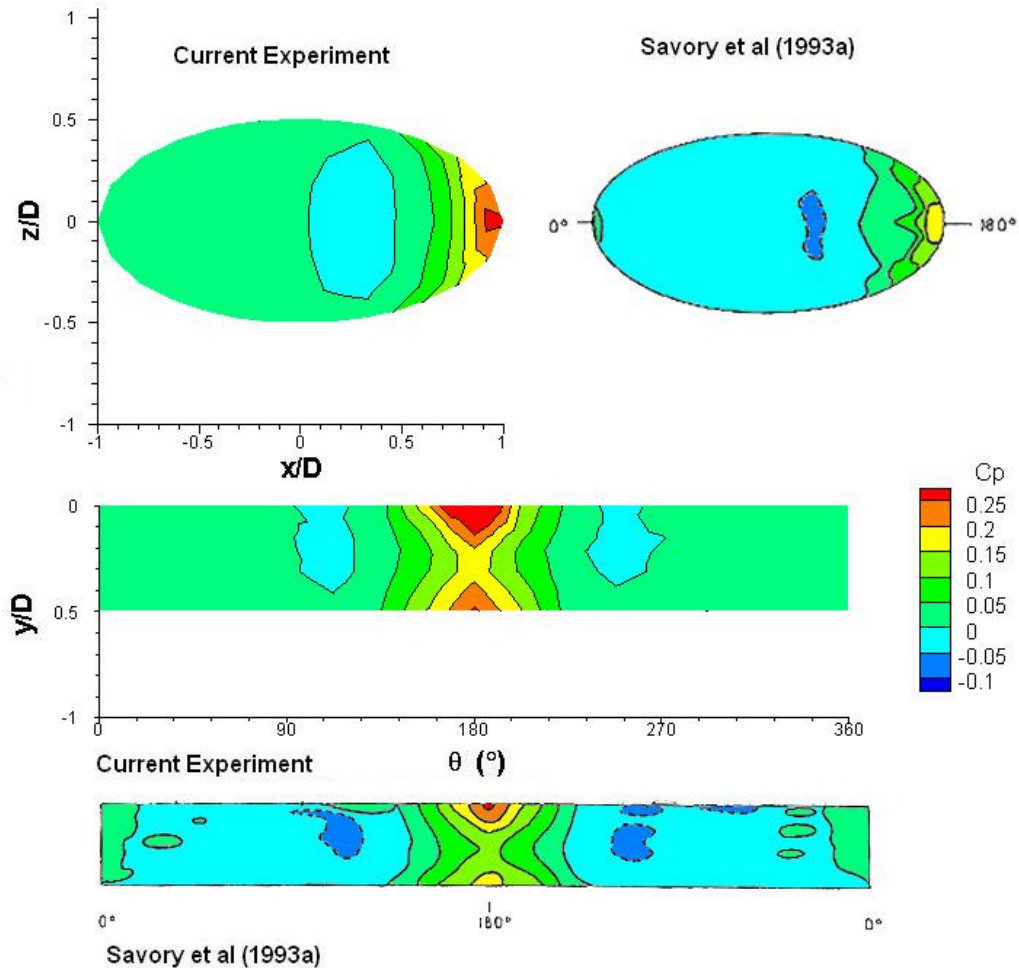
Figure 5-2 Comparison of Cp$_{mean}$ contours to Savory and Toy 1993a) for cavities aligned with the flow (yaw 90°), h/D' = 0.25

The classification of open, closed and transitional flows by Plentovich et al (1993) for rectangular cavities is applicable for this configuration, due to the low three-dimensional flow observed in the cavity base pressure distributions. The pressure data along the cavity base displays only small effects of the sidewall and is highly symmetric for all cavity depths along the span of the cavity. Also the single captive vortex with its axis normal to the flow for deep cavities was also very noticeable for this yaw angle. Thus, comparing the centreline profiles is useful in classifying the flow type as open,

closed or transitional. As mentioned before the cavity depths were normalized by D' (effective cavity streamwise length) in order to make a direct comparison to Plentovich et al's (1993) diagrams. The profiles are shown in Figure 5-3.

The smallest cavity depth contains a very distinct centreline profile, which is not observed for any of the other depths. When comparing to the distinct patterns in Figure 2.2.2, the profile seems to represent a closed cavity, although the pressure rise near the centre of the base is not as defined as found by Plentovich et al (1993) for rectangular cavities. For their cavity depths, Plentovich et al (1993) found open cavity flow to occur for L/h < 10 (h/D' > 0.1) and closed flow to occur for L/h >13 (h/D'< 0.08). This is in very good agreement to the trends seen in Figure 5-3. The depth ratio of h/D' = 0.05 seems to correspond to a closed flow configuration, while the next three depths of h/D' =0.1, 0.13 and 0.18 seem to indicate a transitional flow. The open flow configuration is evident for h/D' = 0.25. As the cavity depths increase beyond this depth, an open cavity type is seen in the profiles.
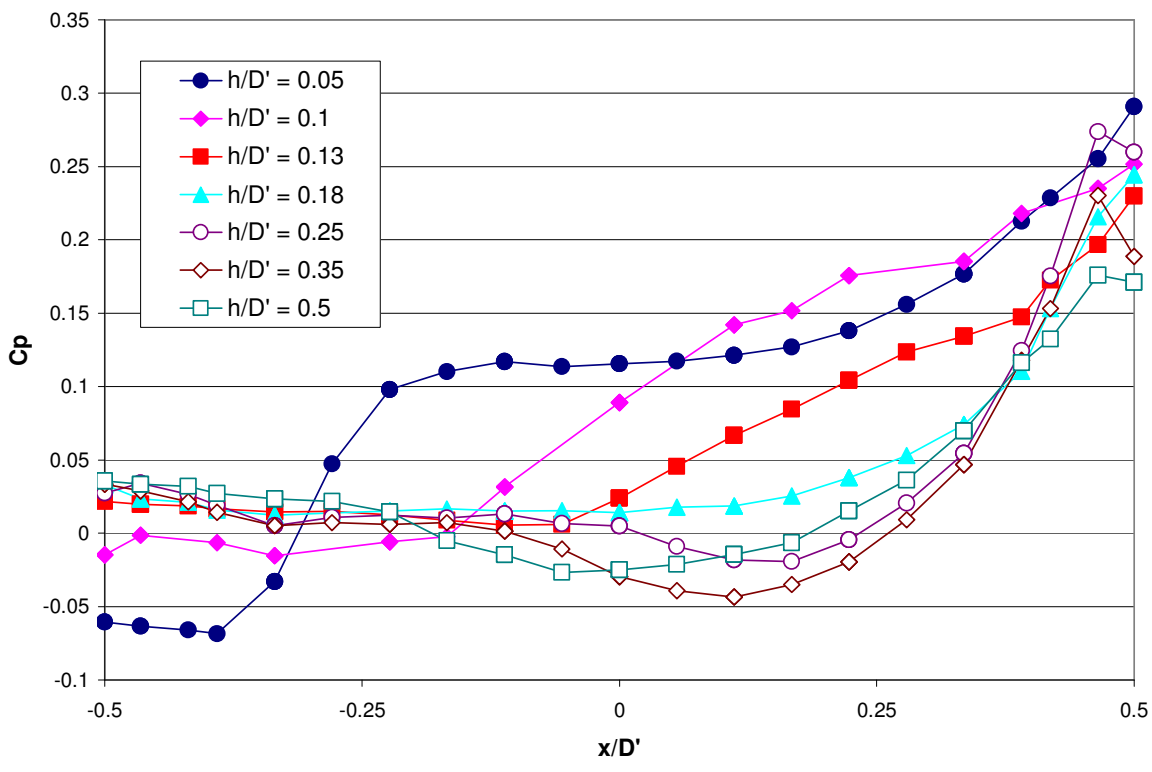
Figure 5-3 Cp$_{mean}$ Centreline profiles for yaw 90°

There exists a low pressure region in the downstream half of the cavity base which moves upstream with increasing depth, as seen in Figure 5-3. This was also observed by Savory et al (1993b) and Ashcroft and Zhang (2005) for rectangular cavities. The low pressure region is a result of the captive vortex which appears to be formed at approximately h/D' = 0.25. Thus, as the cavity depth is increased the captive vortex initially forms in the downstream region of the cavity. Then the vortex centreline moves upstream toward the centre of the cavity as the depth is further increased.
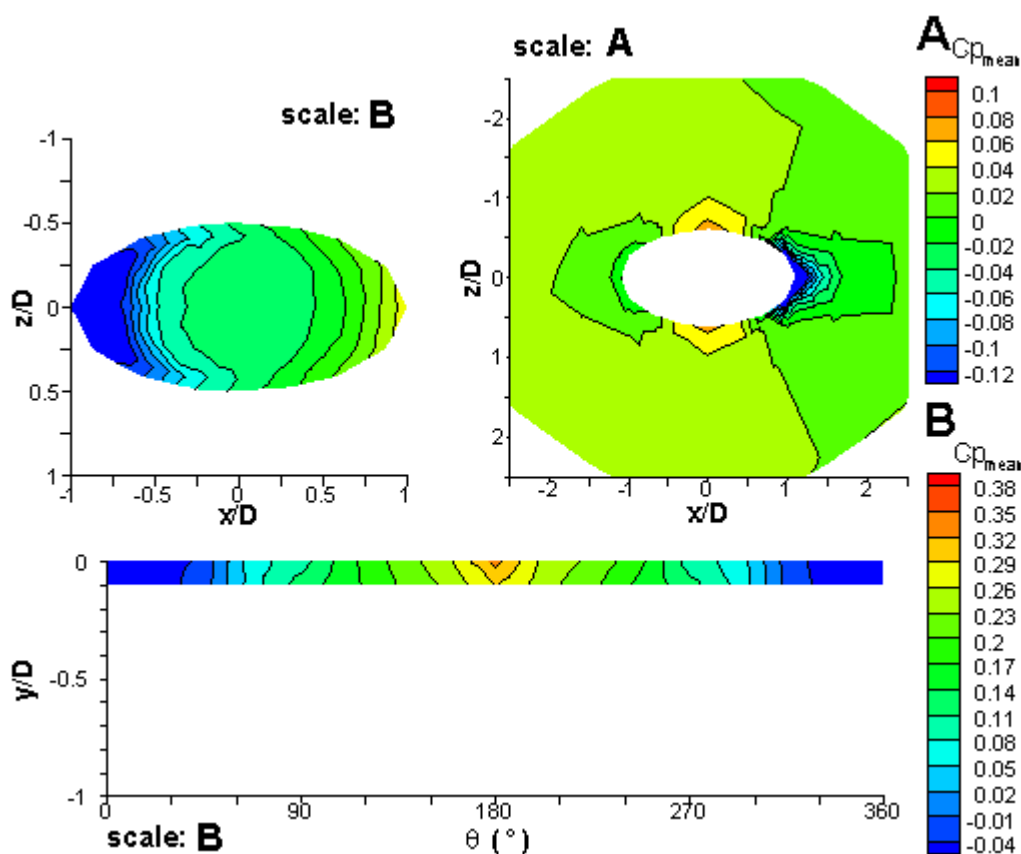
Figure 5-4 Cp$_{mean}$ contours for yaw 90°, h/D' = 0.05, cavity base (top left), ground plane (top right), cavity sidewall (bottom)

The "weak" closed flow configuration for h/D' = 0.05 is seen in Figure 5-4. It is termed "weak" closed flow as the pressure rise due to shear layer impingement on the base is not as pronounced as that seen by Plentovich et al (1993), but the centreline profile indicates a much different pattern than the transitional cavities. The shear layer separation at the upstream cavity edge is indicated by the large negative pressure region observed in the upstream region of the cavity base and on the sidewall at θ ≈ 0. The

second shear layer separation is seen on the ground plane by the second large negative pressure region, directly downstream of the cavity in the same z/D location. When comparing these regions to the other depths, this configuration contains the lowest pressure values in these regions, due to the strong resemblance to a closed flow.
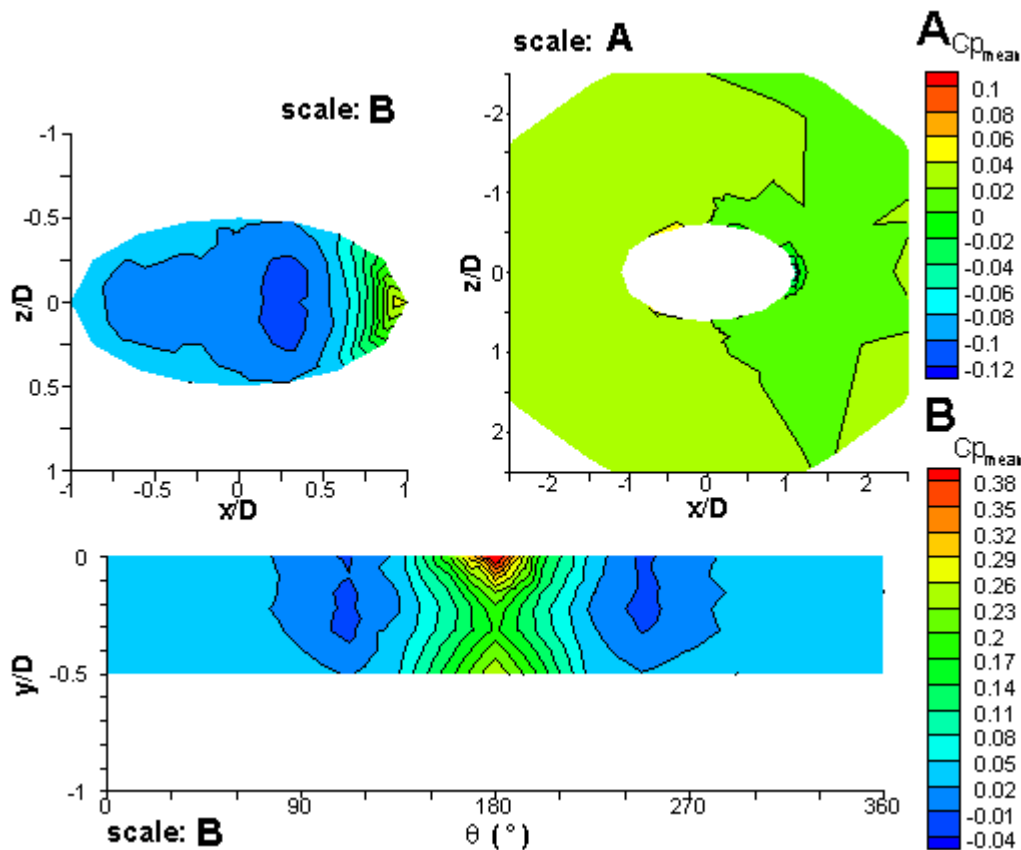
Figure 5-5 Cp$_{mean}$ contours for yaw 90°, h/D' = 0.25, cavity base (top left), ground plane (top right), cavity sidewall (bottom)

Open flow is seen for h/D' = 0.25 which indicates a captive vortex. A single captive vortex can be identified as previously mentioned by circular low pressure regions on the sidewall. In Figure 5-5 the incomplete circular patterns are a cause of the extrapolation scheme used near the lip of the cavity. The vortex seems to be rooted to the cavity sidewall at approximately 110° and 250°. The vortex tube orientation is observed on the cavity base by the negative pressure region aligned with the z-axis at approximately x/D = 0.25. This indicates a vortex tube, which is normal to the freestream direction. The vortex is also contained in the downstream region of the cavity and moves upstream with increasing depth as mentioned earlier in this section.

The separated shear layer is the main driving force of the captive vortex (Roshko 1955, Ukeiley and Murray 2005). The shear layer separates at the upstream cavity edge and spans across the opening of the cavity before impinging near the lip on the cavity sidewall at $\theta = 180°$. After impingement the shear layer is redirected downward toward the base, where a secondary impingement point exists near the downstream tip of the cavity base. This was also observed for rectangular cavities by Czech (2000) and Savory and Toy (1993b). The stagnation pressure is weaker here, as the flow has slowed down compared to the initial impingement. The base further directs the flow in the upstream direction as seen by the adverse pressure gradient on the base. By this process the separated shear layer drives the large recirculation inside open cavities.

As the cavity flow regime changed from closed to transitional to open, the maximum magnitude of the pressure coefficient associated with the initial shear layer impingement increases up to approximately 0.42 for $h/D' = 0.25$ with increasing depth, before it drops off slightly for $h/D = 0.7$ and 1.0. The higher stagnation pressures indicate that higher velocity fluid is being drawn into the cavity (Dybenko, 2005) as opposed to open cavities, which contain a lower stagnation pressure on the sidewall. For deep cavities low velocity fluid is being drawn into the cavity, which is contained closer to the ground plane in the shear layer. Thus the presence of the cavity affects a smaller portion of the shear layer, which reduces the drag of the cavity.

The distribution of pressure fluctuations is very similar qualitatively to the mean pressure distributions. High pressure fluctuations are observed in areas where shear layer impingement was predicted on the cavity sidewall and base from the mean pressure data. These large Cp_{rms} values are caused by the velocity fluctuations in the approaching boundary layer, which is drawn into the cavity. Other areas of relative high pressure fluctuations are seen in the areas where the captive vortex is rooted to the sidewall, seen in Figure 5-6. Fluctuations in this area are associated with the circulation velocity of the vortex as noted by Ashcroft and Zhang (2005).

The wake profiles for this configuration ($h/D' = 0.25$) also showed similar results to rectangular cavities. Velocity defects in the streamwise direction indicate the existence of side vortices, seen in Figure 5-7. These vortices are only seen for this yaw angle. Surface oil visualization technique for rectangular cavities showed that flow is

entrained into the cavity along the side walls once the shear layer flows over the leading cavity edge (ESDU, 2004). It was also noted that as the cavity width was decreased for rectangular cavities, the entrainment over the sidewall increased, which may lead to the formation of these side vortices. This is in agreement to the current configuration as it had the highest streamwise length to span length ratio of all the cavity configurations examined.

Figure 5-6 Cp$_{rms}$ contours for yaw 90°, h/D' = 0.05, cavity base (top left), ground plane (top right), cavity sidewall (bottom)

These side vortices were observed to create a larger velocity defect as the cavity depth was increased in the current investigation, indicating a dependence on the cavity flow type. Thus, for open cavities the side vortices appear to cause a stronger defect indicating larger flow entrainment along the side than for transitional flows. As mentioned earlier only cavities aligned with the flow showed these side vortices. This is due to the large effective streamwise length to width ratio of this cavity.

Cavities aligned with the flow closely resembled some key features of rectangular cavity flow. The main reasons for the similarities include the highly two-dimensional flow when compared to other elliptical configurations, which lead to good agreement to open and closed cavity classifications. The transition flow types occurred around similar h/D' ratios as found by Plentovich at al (1993) for rectangular cavities. The existence of side vortices was also seen for this configuration due to the small width of the cavity compared to the streamwise length.
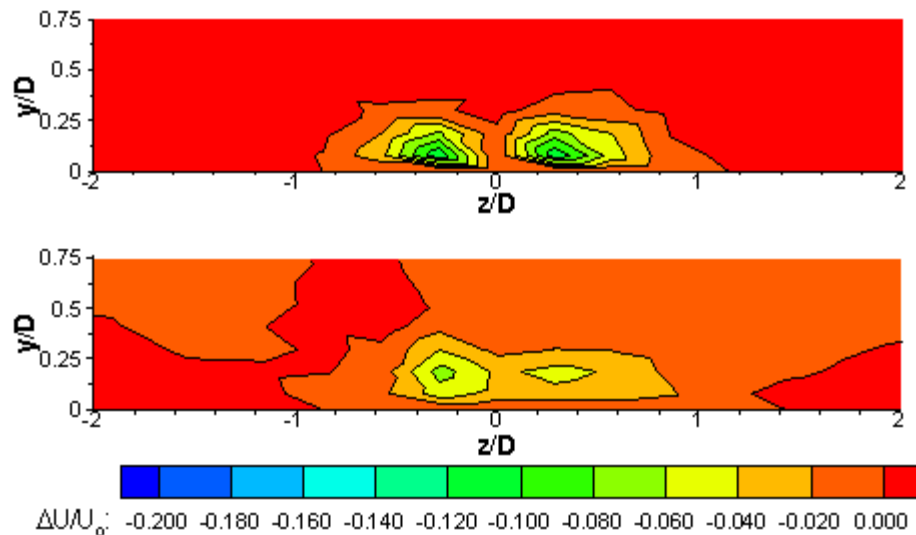
Figure 5-7 Streamwise velocity defect at x/D' = 0.5 (top) and x/D = 2.6 (bottom) for yaw 90°, h/D' = 0.25

5.2.2   Deep cavity type flow

The flow regime associated with h/D = 1.0 show similar trends for all yaw angles examined. The flow was an open type, where a large captive vortex is observed along the span of the cavity and shear layer impingement, predicted by high Cp values was seen around 180° near the lip on the cavity sidewall. Although this was most evident in the yaw 90° case, the other yaw angles all contained a similar large captive vortex. Small changes with yaw angle showed the vortex being slightly slanted in the vertical direction as seen for the yaw 30° case. The change in the normalized drag coefficient was also small, as it varied only form approximately 5 to 9 with yaw angle. This was small compared to the drag coefficient changes of the other cavity flow types with yaw angle.

The small changes with yaw angle might be due to the limiting depth of this flow regime being slightly larger than h/D = 1.0. This was the largest depth examined and therefore there were no deeper cavities top compare to. Thus, the effect of increasing the depth even further may lead to even smaller discrepancies between the yaw angles. Shear layer impingement was also noticed near lip region on the sidewall at approximately θ = 180°, which did not vary significantly with yaw angle.
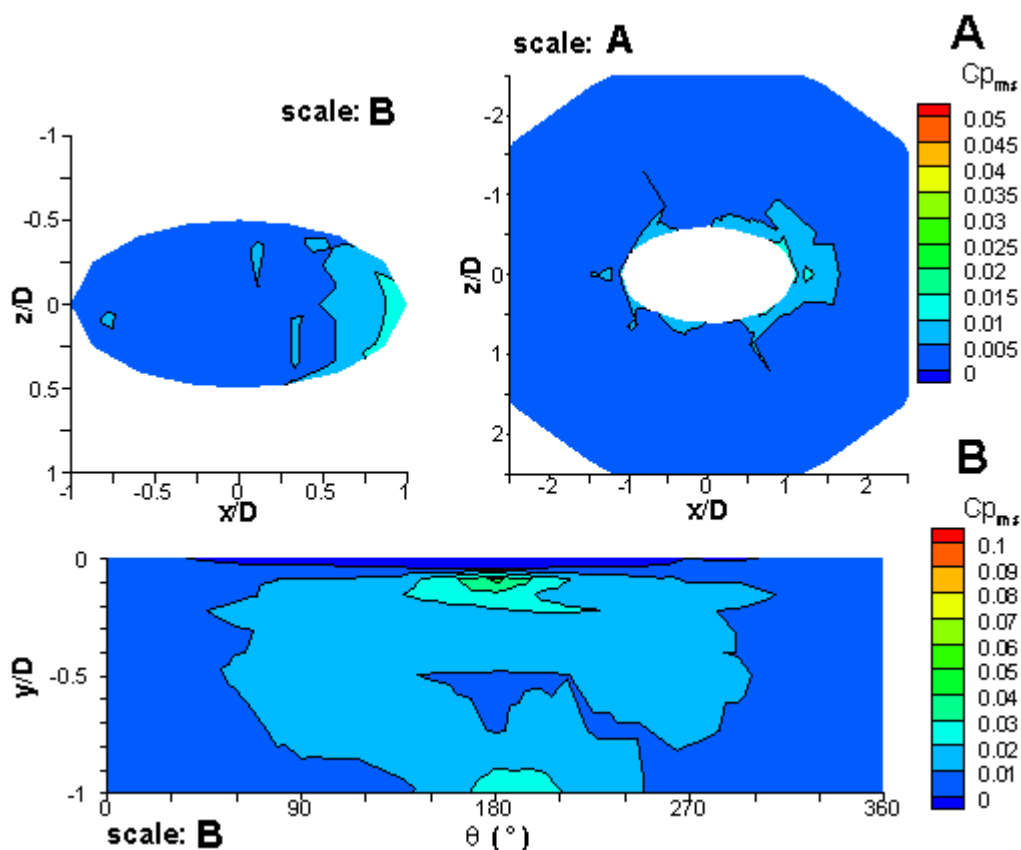
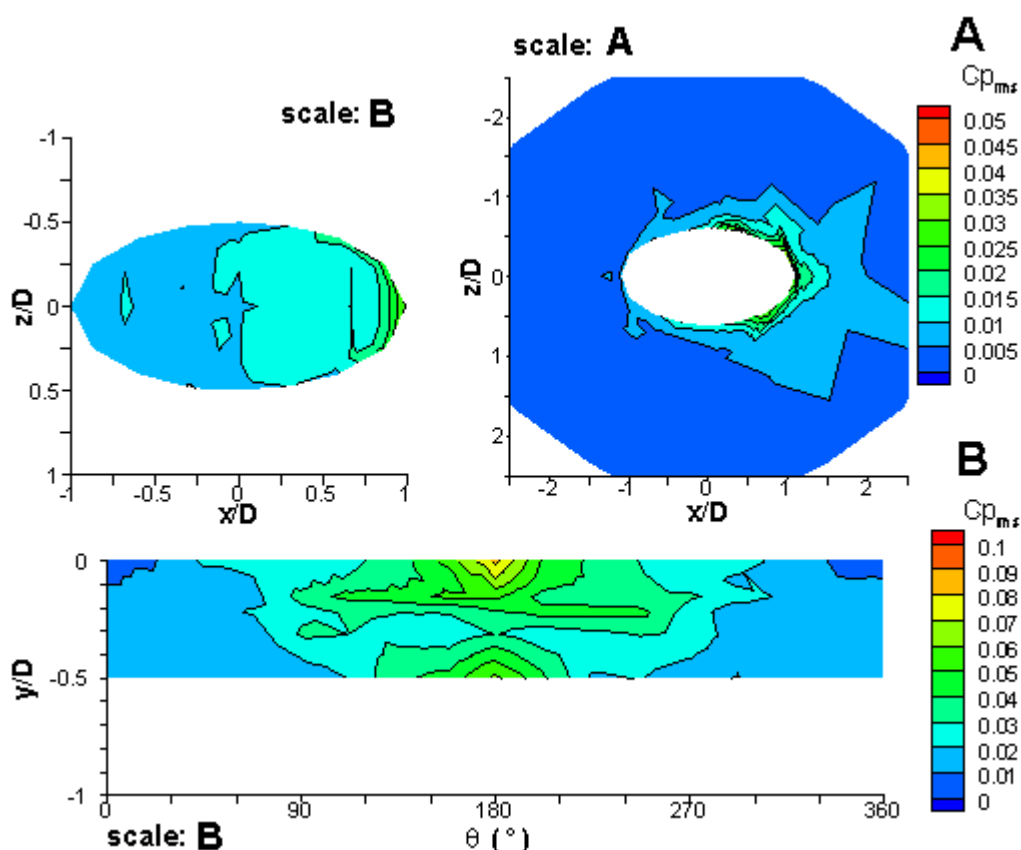**Figure 5-8 Cp$_{rms}$ contours for yaw 90°, h/D' = 0.5, cavity base (top left), ground plane (top right), cavity sidewall (bottom)**

Pressure fluctuations in terms of Cp$_{rms}$ were also the lowest for this depth compared to the other depths. The highest fluctuations were seen in the shear layer impingement region in Figure 5-8, and thus, these fluctuations are attributed to fluctuations in the shear layer (Czech 2000). Although the magnitude of the pressure fluctuations was approximately 0.1 Cp lower than the highest fluctuations observed in the other depths containing a captive vortex for the given yaw angles. Pressure fluctuations in the vicinity of the vortex tube being rooted to the sidewall were also low compared to

other flow types. This indicated a stable structure inside the cavity volume, which was also observed by PIV measurements of rectangular deep cavities (Ukeiley and Murray 2005). Ukeiley and Murray (2005) found that by increasing the h/D' from 0.19 to 0.67, the fluctuations in streamwise velocity decreased from $0.25U_o$ to $0.14U_o$. The effect of yaw angle thus seems to be negligible due to a constant shear layer impingement location on the sidewall and the presence of the stable captive vortex for all yaw angles. The lower Cp and Cp_{rms} values compared to other depths indicate that the flow has a smaller effect on the shear layer above the cavity, which results in lower drag.

5.2.3   *Shallow cavity type flow*

For the smallest depth, h/D = 0.1, the effects of yaw angle are also negligible as for the deep cavity flow regime. The flow resembles mostly a transitional cavity, although for high yaw angles similarities to closed flow are also seen. The pressure contours on the base indicate a transitional flow since a low pressure region is found near the upstream side of the cavity (x/D $\approx$ 0.75), seen in Figure 5-9. This indicates a recirculation region (Czech 2000), which is associated with the initial shear layer separation, which was observed for all yaw angles. Shear layer impingement is not observed on the base as a high pressure region is not evident on this surface. The high stagnation pressures on the sidewall indicates shear layer impingement near the lip on the furthest downstream region on the sidewall (maximum x/D value of the sidewall) for all yaw angles.

A large region of negative pressure is also observed on the ground plane directly downstream of the cavity in the same z/D location as the shear layer impingement on the sidewall. This low pressure region indicates the secondary shear layer separation and the recirculation zone associated with it. The pressure associated with this region was the lowest for all the configurations examined.
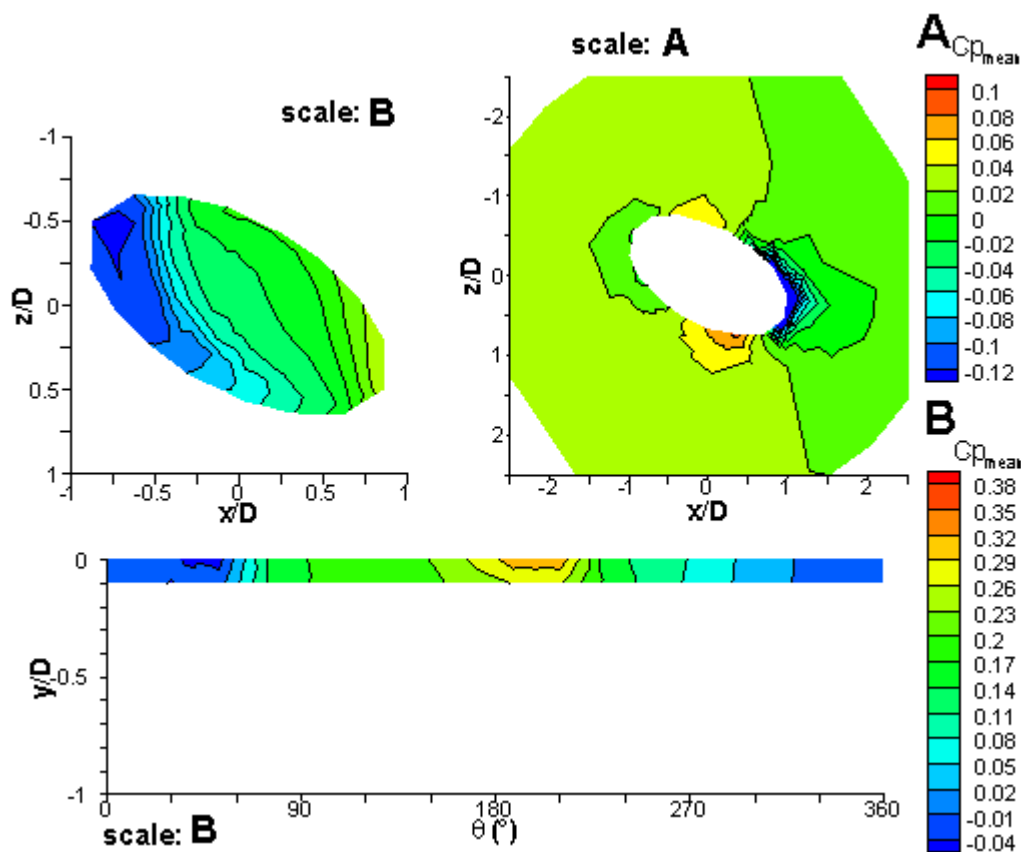
Figure 5-9 Cp$_{mean}$ contours for yaw 60°, h/D = 0.1, cavity base (top left), ground plane (top right), cavity sidewall (bottom)

For yaw angles of 75° and 90° a "weak" closed flow is seen, as described in Section 5.2.1.   A small rise in pressure on the base near the cavity centre indicates that the shear layer dips into the cavity near the centre but does not impinge on the base. Examining the Cp$_{rms}$ contour plots, the fluctuations on the base are much lower than seen for the secondary shear layer impingement on the sidewall. This also suggests that shear layer impingement on the base is not seen for these configurations, but the shear layer rather dips into the cavity without any impingement on the cavity base.

The consistency of these key features over all the yaw angles suggests that yaw effects are also negligible for this depth. Although the effects of yaw do not change the flow type there is a larger change in the resulting drag with yaw angle than for the deep cavities, h/D = 1.0. This is in contrast to cavities with 0.1< h/D <1.0 where the yaw angle has a significant effect on the resulting flow regime and drag coefficient.
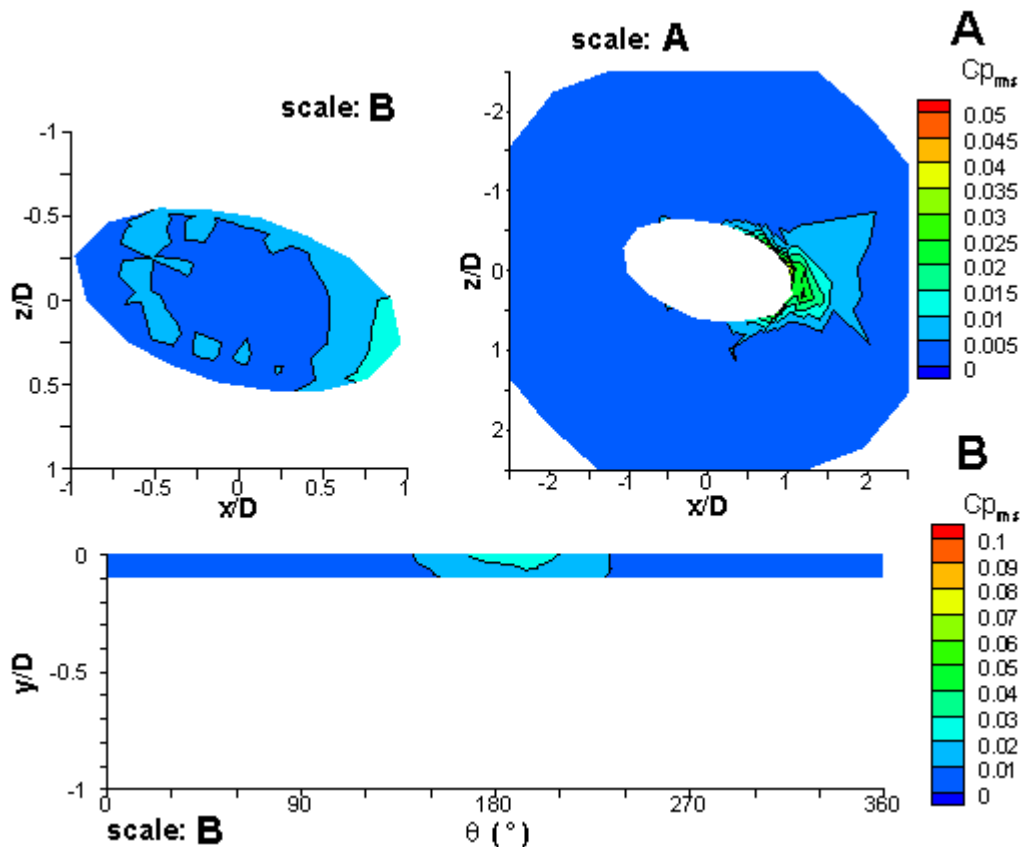
Figure 5-10 Cp$_{rms}$ contours for yaw 75°, h/D = 0.1, cavity base (top left), ground plane (top right), cavity sidewall (bottom)

The flow regimes examined so far have included nominally two-dimensional flow (yaw 90°), which is similar to rectangular cavity flow regimes. The cavity flow type ranges from "weak" closed flow, h/D' =0.05 to open flow for h/D' = 0.5. A captive vortex was observed for depths h/D' ≥ 0.25. This lead to the second flow regime which contained a large captive vortex for all yaw angles for cavity depths of h/D = 1.0. Pressure fluctuations were lower than for smaller depths as a stable captive vortex was observed inside the cavity. For very shallow cavities, h/D = 0.1 yaw effects were also negligible as the flow regime mostly resembled a transitional cavity flow. Low pressure fluctuations were observed as the shear layer only dipped into the cavity slightly and did not case a captive vortex to form. All of these regimes contained large Cp values located at θ = 180° on the sidewall indicating shear layer impingement.

5.2.4   *Cellular structure (yaw 0°)*

This flow type occurs for the largest aspect ratio cavity configuration examined as seen in Figure 5-1. Rectangular cavities with large aspect ratios may exhibit three-dimensional flow far away from the sidewalls as mentioned in Section 2.2.1. This cell like structure was also seen in the data for yaw 0°, h/D = 0.2 to 0.7, which had the largest span to streamwise length ratio compared to the other configurations.

Cavities normal to the flow (yaw 0°) were first compared to Savory and Toy's (1993a) data, as seen in Figure 5-11. The difference between the two investigations was once again approximately 0.05 Cp, same as for cavities aligned with the flow. This verifies that the difference is independent of cavity configurations and must be due to the different static pressure location and thickness of the approaching boundary layer.
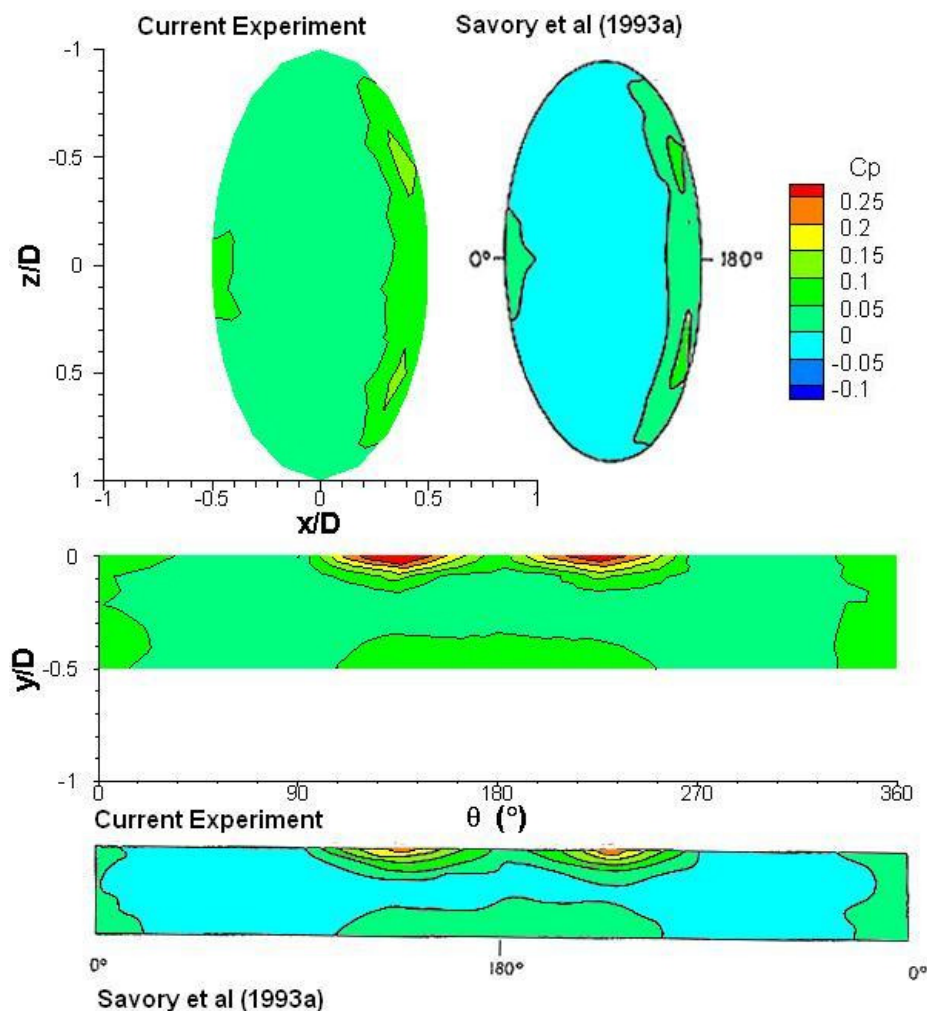
**Figure 5-11 Comparison of Cp$_{mean}$ contours to Savory and Toy
(1993a) for cavities normal to the flow (yaw 0°), h/D = 0.5**

The flow regimes for this yaw angle are highly three-dimensional compared to the previous three flow regimes discussed. This flow type is very similar to rectangular cavities with larger aspect ratios as documented by Maull and East (1963) and Czech (2000). The sidewall contains two regions of shear layer impingement as opposed to the single one for all the other configurations. The impingement regions occur roughly at 135° and 225° for all depths of this flow type. Although the flow is highly three-dimensional, there is strong symmetry along the span of the cavity (z-axis) inside the cavity as well as on the ground plane, seen in Figure 5-12. The two impingement zones on the downstream cavity wall were also observed by Czech (2000) for rectangular cavities, but occurred only for aspect ratios equal to 3.18 or greater.

**Figure 5-12 Cp$_{mean}$ contours for yaw 0°, h/D = 0.35, cavity base (top left), ground plane (top right), cavity sidewall (bottom)**

Along with the two shear layer impingement zones, a captive vortex seems to form inside the cavity along the span starting at h/D = 0.35. The pressure contour on the cavity base indicates a "wave" like effect on this single captive vortex, as mentioned by

Maul and East (1963). Low pressure zones are found on the base at the same z/D location as the shear layer impingements on the sidewall. The shear layer impingement zones on the sidewall along with their corresponding low pressure zones on the base indicate the same mechanism as for open flows, where the shear layer is drawn into the cavity and drives the stable vortex, indicated by the low pressure region. The other regions of the stable vortex which do not have a shear layer impingement associated with them are not driven directly by the shear layer. Thus, the recirculation velocity in these regions is lower do to the indirect drive of the recirculating velocity in these regions by the shear layer. This results in the "wave" like stable vortex configuration found by Maull and East (1963) for this yaw angle.

The wake velocity profiles showed only a significant velocity defect near the cavity centreline, z/D = 0, seen in Figure 5-13. This was somewhat unexpected due to the two shear layer impingement regions located further away from the centreline along the span of the cavity. The velocity defect was lower in magnitude than for the yaw 90° case, indicating that the overall drag for cavities normal to the flow seems to be less than for cavities aligned with the flow. The stagnation Cp associated with the two impingement regions was approximately 0.05 lower than for the single impingement region found for yaw 90° depths. The drag associated with these cavities will be further discussed in Section 5.3.
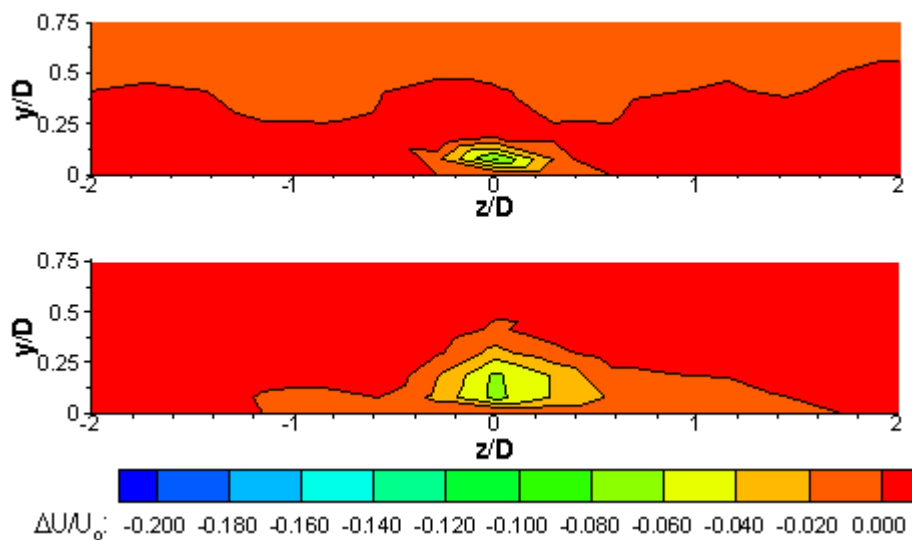
Figure 5-13 Streamwise velocity defect at x/D = 0.5 (top) and x/D = 2.6 (bottom) for yaw 0°, h/D = 0.5

The previous flow regimes were all yaw independent or were configurations with their major axis aligned or normal to the flow. All flow regimes displayed highly symmetric flow. These flow regimes displayed shear layer impingement in the same region on the sidewall for all depths and contained a captive vortex for depths greater than h/D = 0.5. The following flow regimes vary with yaw angle as well as cavity depth.

5.2.5   *Weak asymmetric flow*

This flow regime occurs for yaw angle of 15°, as seen in Figure 5-1. The flow field only changes slightly when yawing the cavity to 15° from 0° for depths h/D = 0.25 to 0.7. The captive vortex forms at a similar h/D ratio and the vortex axis is also aligned with the major axis of the cavity as for yaw 0° configurations. The major difference between the two yaw angles is that only a single shear layer impingement region is observed for yaw 15° as opposed to the two impingement points seen for yaw 0°. The single shear layer impingement was located at approximately $\theta = 140°$ on the sidewall, seen in Figure 5-14. This location corresponds quite well with one of the shear layer impingement points for yaw 0° found at approximately $\theta = 130°$. The elimination of one of the impingement points suggests that this flow type does not contain cell structures. This also indicates that the cell structures are highly affected by yaw changes, as a 15° change did not alter the flow field this significantly in the other configurations. The impingement Cp was also lower on average by 0.06 compared to the yaw 0° case. This again, seemed to indicate a lower drag associated with these cavities.
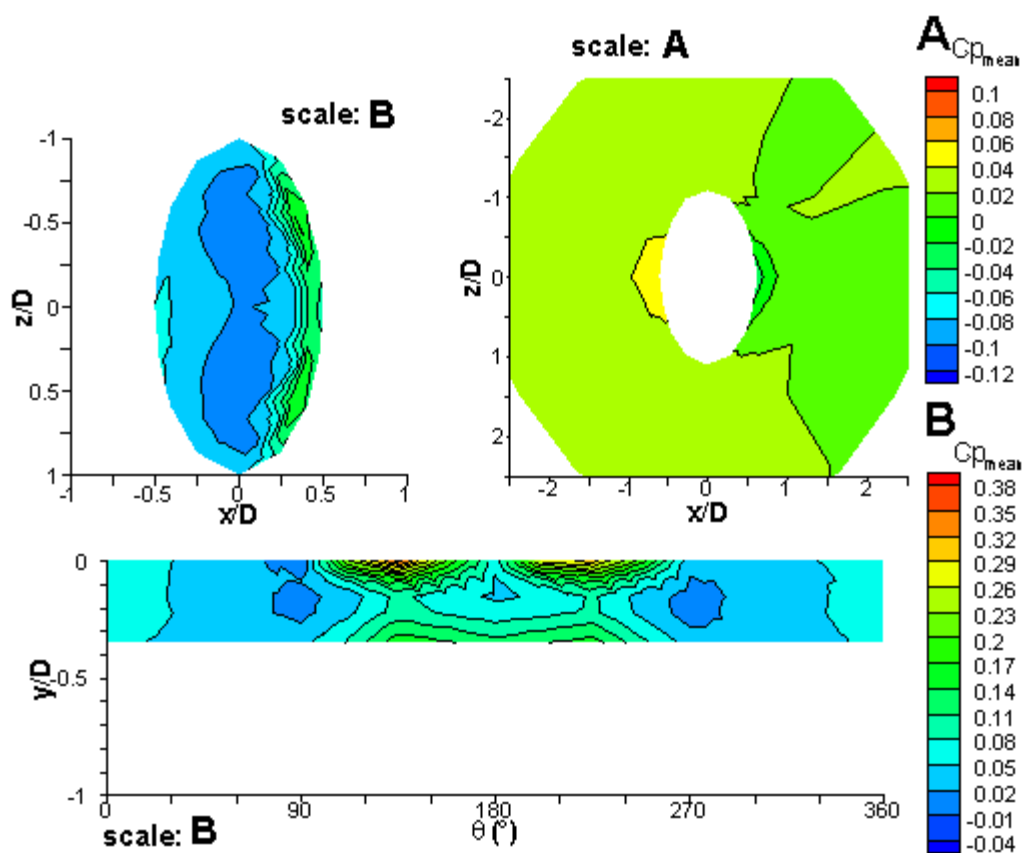
**Figure 5-14 Cp$_{mean}$ contours for yaw 15°, h/D = 0.35, cavity base
(top left), ground plane (top right), cavity sidewall (bottom)**

5.2.6   *Strong asymmetric flow*

The increase in yaw angle form 15° to higher values results in the flow being diverted to one side of the cavity, which creates a strong asymmetric flow pattern. For these yaw angles the flow is altered significantly by the downstream cavity sidewall, which forces the flow to one side of the cavity. This asymmetry also causes the stable vortex to be slanted in the vertical direction and so a trailing vortex is seen for certain depths.
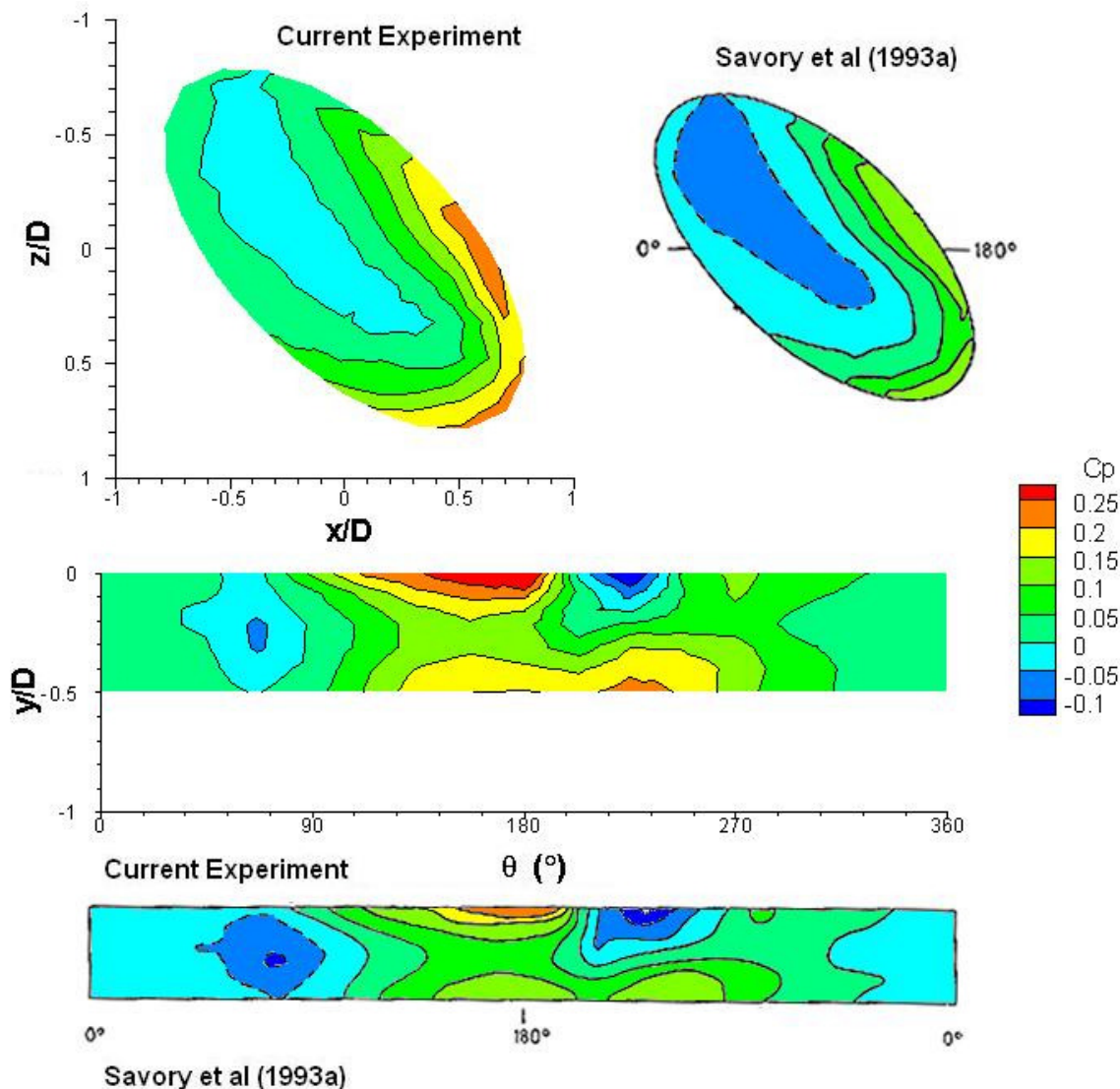
Figure 5-15 Comparison of Cpmean contours to Savory and Toy (1993a) for cavities yawed to the flow (yaw 45°), h/D = 0.5

When comparing the results of yawed cavities, only the case of yaw 45° could be compared as no other yaw angles were examined in any other experiments. Once again good agreement was found between the results of Savory and Toy (1993a) and the current experiment. The constant offset of approximately 0.05 Cp is also evident for this yaw angle.

Increasing the yaw angle past 15° resulted in very different flow regimes when compared to the yaw 0° and 90° configurations. The location of the initial shear layer impingement transitioned smoothly from approximately θ = 140° to 180° as the cavity

was rotated from yaw 15° through yaw 75°. After shear layer impingement at this location the shear layer was directed downward as well as along the sidewall. This caused the secondary impingement location to occur over a wider region on the downstream part of the cavity base, as compared to the aligned and normal cases, seen in Figure 5-17. The flow pattern is very similar to the flow regimes found for rectangular yawed cavities at these yaw angles. Czech (2000) showed a schematic of the aerodynamic phenomena within yawed rectangular cavities, seen in Figure 5-16. As the figure illustrates a vortex forms along the major axis of the cavity caused by the shear layer which is directed along the sidewall as well as downward toward the base.
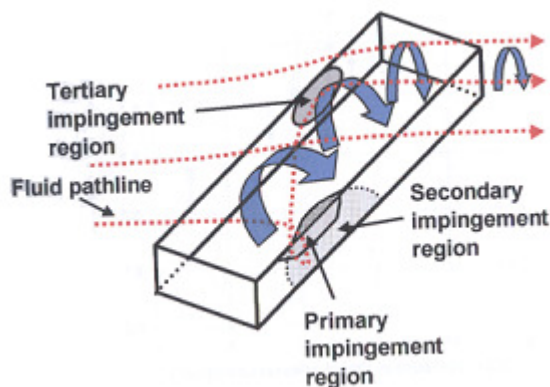
Figure 5-16 Schematic model of the flow structure inside a yawed rectangular cavity (Czech 2000)

The increased positive pressure near the bottom of the sidewall, in the downstream part of the cavity caused by the shear layer forces the captive vortex out of the cavity. This is seen in Figure 5-17, where the captive vortex seems to be rooted at approximately $\theta = 70°$ on the sidewall and a large negative pressure region exists near the lip of the cavity at $\theta = 230°$. This negative half circular pressure region indicates that part of the captive vortex is leaving the cavity. This is further confirmed by the negative pressure region seen downstream of the cavity on the ground plane. The negative pressure region is not as low as the pressures associated with the second shear layer separation for the "weak" closed flow for yaw 90, h/D = 0.1. The axis of the vortex also appears to be angled with regard to the horizontal when examining the sidewall plot in Figure 5-17. The centres of the two circular negative pressure regions are located at different y/D values.
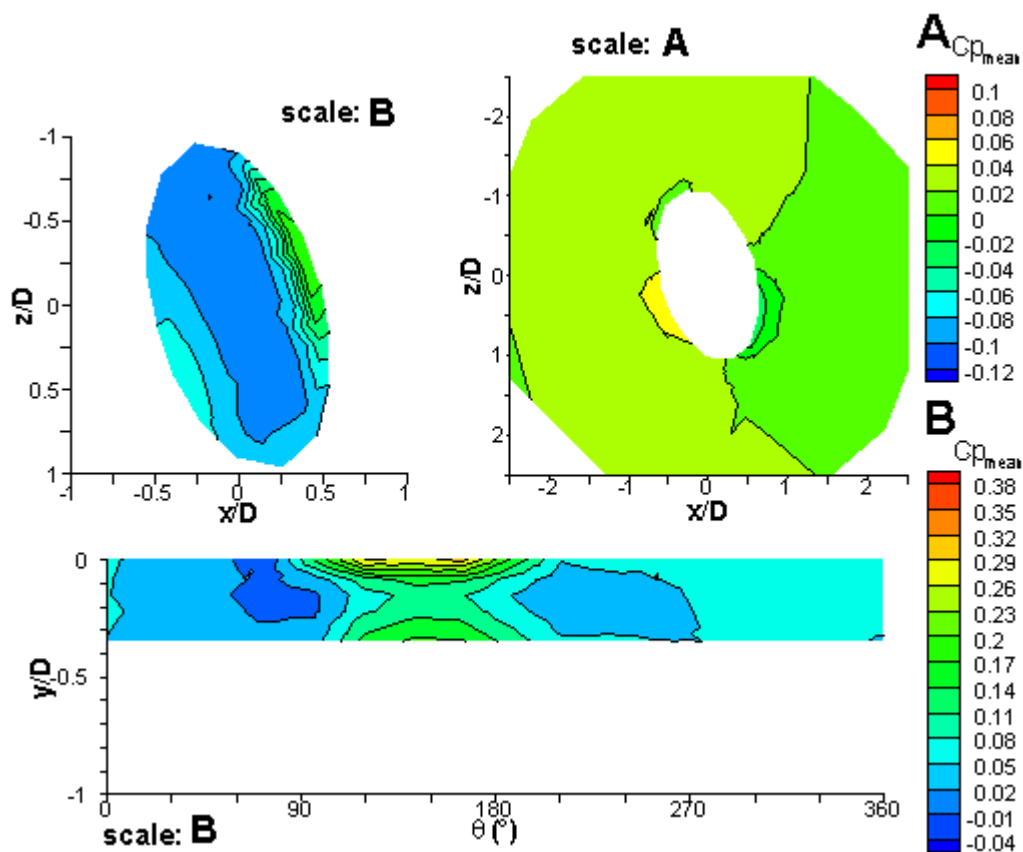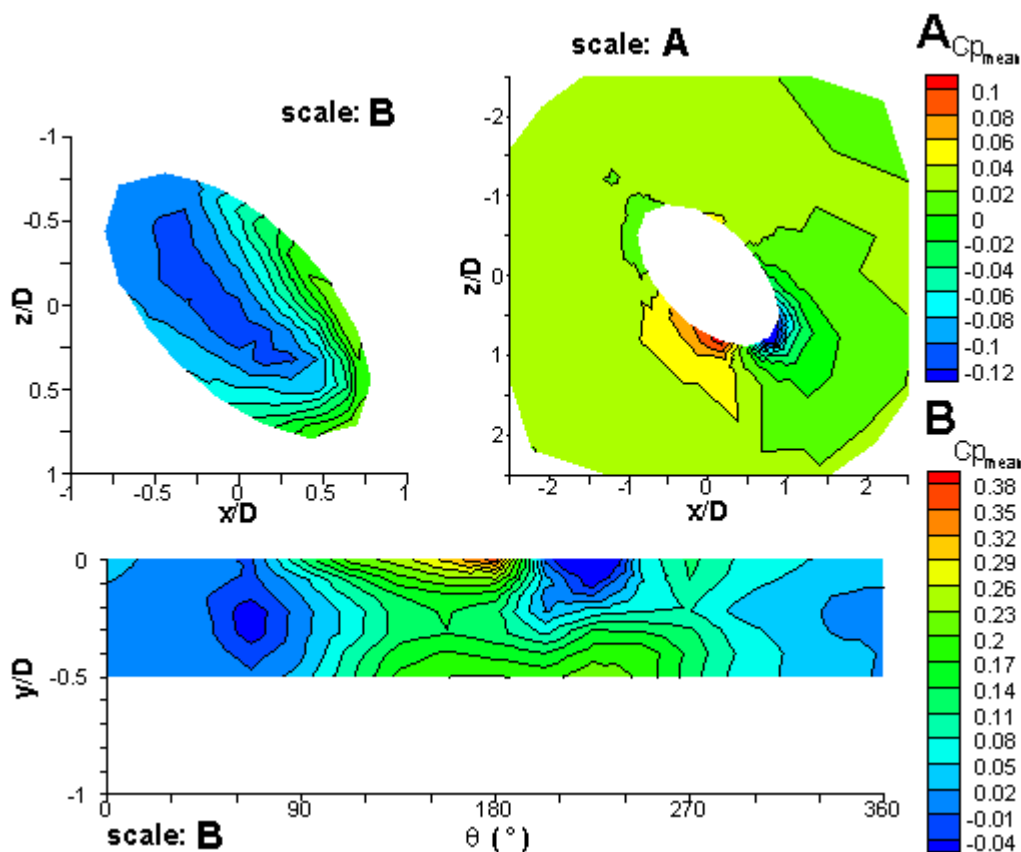
Figure 5-17 Cp$_{mean}$ contours for yaw 45°, h/D = 0.5, cavity base (top left), ground plane (top right), cavity sidewall (bottom)

Evidence of the trailing vortex was also observed in the wake measurements for yaw 45°, seen in Figure 5-18. The velocity defect is much stronger than that observed for yaw angles of 0° and 90°, indicating a higher drag coefficient. For all three velocity components this yaw angle creates the largest defect compared to the other yaw angles for all depths. Although the trailing vortex extends out of the cavity at a 45° angle compared to the freestream direction, the spanwise (z axis) velocity of the vortex is very small compared to the freestream velocity. This is suggested as the vortex centre appears to be in the same z/D location for both downstream measurement locations.

This trailing vortex configuration is seen up to h/D = 1.0, when the vortex is once again contained inside the cavity and a more "open" flow type is seen, as mentioned in Section 5.2.2. This is due to a lower stagnation pressure in the downstream cavity base region, which is not strong enough to force the vortex out of the cavity at the trailing edge.
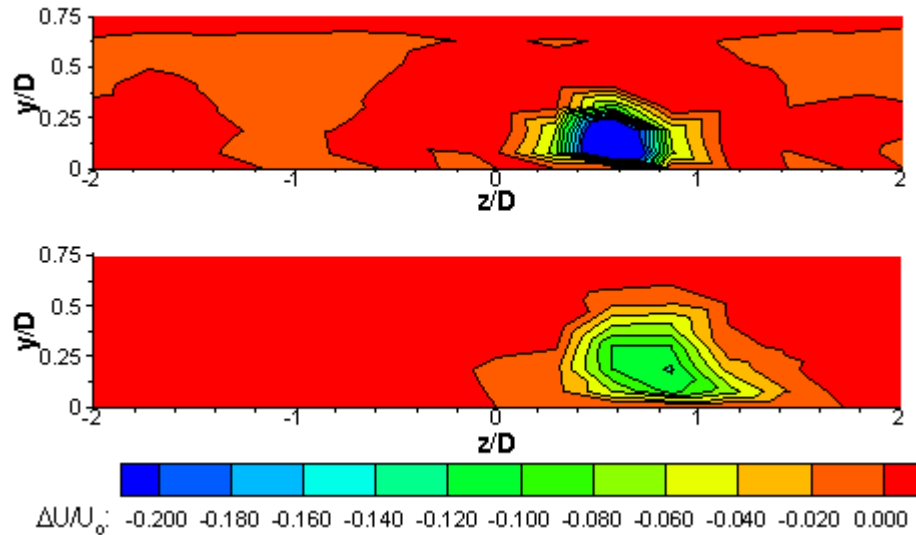
Figure 5-18 Streamwise velocity defect at x/D = 0.7 (top) and x/D = 2.6 (bottom) for yaw 45°, h/D = 0.5

5.2.7   High drag flow regime

The last flow type associated with yawed elliptical cavities is the high drag flow regime, which occurs for strong asymmetric flows at approximately h/D = 0.35 to 0.5 for yaw angles 45° and 60°. This configurations contains the largest Cp values at the initial shear layer impingement region and the lowest Cp values seen on the ground plane where the trailing vortex exits the cavity on the ground plane as compared to the other asymmetric flows. Cp values as high as 0.35 are observed near the lip on the sidewall at approximately θ = 170°, while Cp values as low as - 0.16 are seen on the ground plane. The drag associated with these cavities is the highest of all the configurations. The wake velocity plots show the large trailing vortex for all three depths of h/D = 0.2, 0.5 and 0.7. The strongest velocity defect is seen for h/D = 0.5, which corresponds well with the high drag coefficient of this configuration.

5.3 Resulting Drag and Lift coefficients

The different flow regimes are now compared in terms of the resulting drag and lift coefficient. Examining the mean pressure distributions along the cavity sidewall and base allowed the corresponding drag and lift coefficients to be calculated by the method

described in Section 4.3. Subtracting the corresponding drag and lift coefficient of the ground plane from the total drag and lift coefficients obtained with the cavity in place isolated the effect of the presence of the cavity. Thus, the net effect of the cavity is examined in the following section.

5.3.1   Drag associated with yaw angles 0° and 90°

The resulting normalized drag coefficients were plotted along with previous results for rectangular, circular and elliptical cavities. Only yaw angles of 0° and 90° were compared, as these configurations had a comparable definition of effective cavity length and their planform shapes were symmetric about the streamwise axis. In the following graphs D' is equal to the cavity length in the streamwise direction along the cavity centreline.
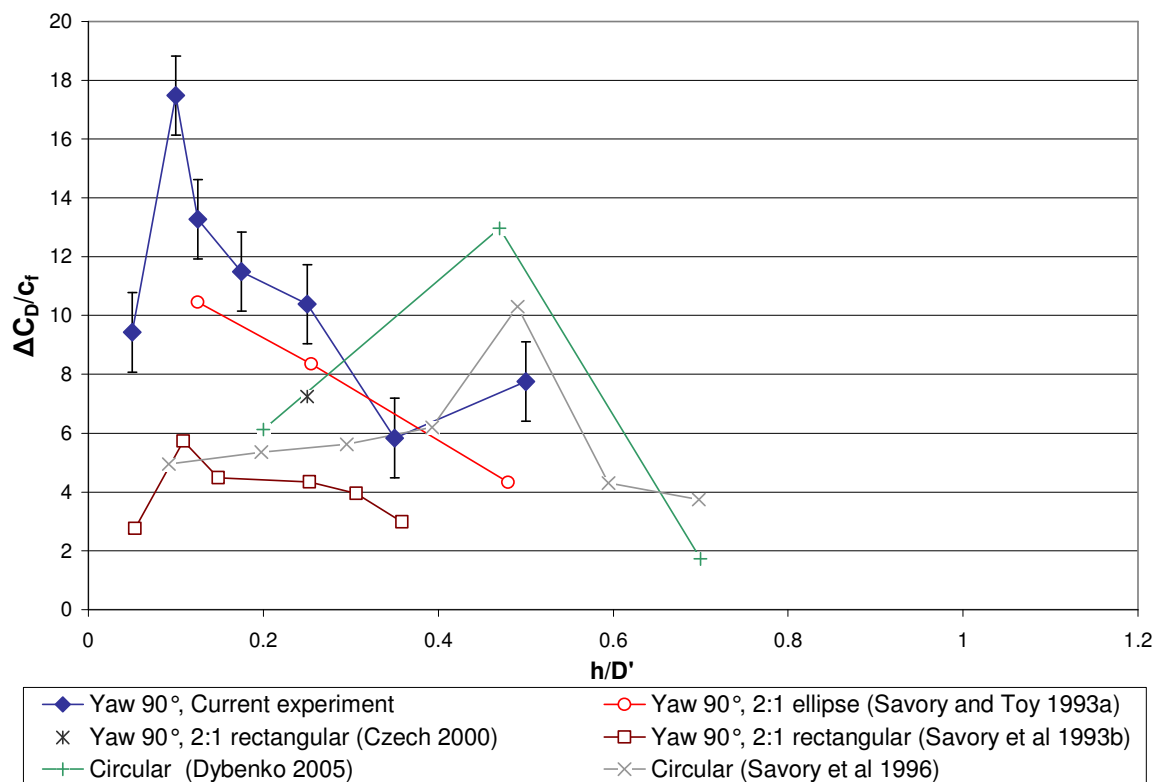
Figure 5-19 Comparison of resulting drag of yaw 90° configuration

The yaw 90° case seen in Figure 5-19 shows similar trends to previous data for elliptical and rectangular cavities at the same yaw angle. The drag decreases as the flow regime changes to an open type. As mentioned in Section 5.2.2, open flow regimes have lower shear layer impingement pressures associated with them than shallower depths, which indicate transitional flow. Therefore, less of the shear layer is effected by the presence of the cavity, which results in a lower drag coefficient. The peak in the drag coefficient at h/D' = 0.1 corresponds quite well with the small peak observed for rectangular cavity data around the same h/D' value.

The trends associated with yaw 0° cavities are also very similar to rectangular cavities with increasing depth, seen in Figure 5-20. The change in drag over the depths examined is much smaller than for yaw 90° cavities. The smaller velocity defects observed in the wake measurement also correspond quite well to the resulting drag coefficient, as the drag of all yaw 0° cavities is much lower than those of yaw 90°.
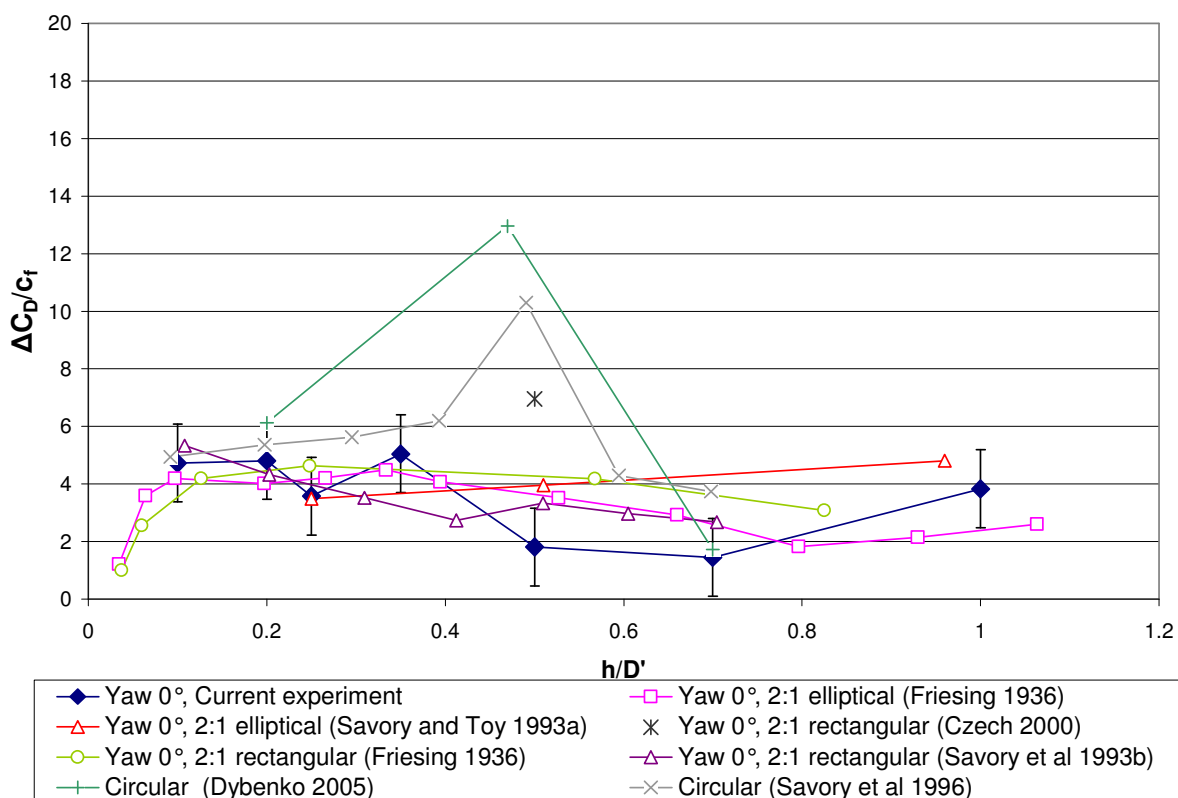
Figure 5-20 Comparison of resulting drag of yaw 0° configuration

The large increase in drag coefficient seen for circular cavities is not observed for elliptical cavities at yaw 0° and 90° around similar depths. The resulting asymmetric flow pattern in circular cavities has been attributed to the cause of this drag peak at h/D ≈ 0.5. Asymmetric flow patterns are not seen for the yaw 0° and 90° cavities.

5.3.2   *Drag of asymmetric flow regimes*

The drag associated with the yawed cavities is seen in Figure 5-21. The general contour pattern is similar to that found by Savory et al (1993b) for rectangular cavities. The maximum drag occurs for cavities of h/D ≈ 0.5 with yaw angles 45° to 60°. The mean pressure patterns for these configurations are very similar to those of circular cavities at h/D' = 0.47 (where D' is the diameter). At these depths an asymmetric flow pattern is seen for the circular cavities, which has been linked to cause the increased drag.

The results from Dybenko (2005) are shown in Figure 5-22 for circular cavities with h/D' = 0.47. These are compared to the results from an strong asymmetric flow regime cavity with yaw 45° and h/D = 0.5, seen in Figure 5-23. The boundary layer and freestream parameters between the two studies were the same, as was the planform area of the cavities, as both studies were conducted in the same wind tunnel. There are several key similarities between the two figures. The trailing vortex appears to be rooted to the sidewall for both geometries around $\theta = 75°$ and is seen leaving the cavity at approximately $\theta = 220°$.
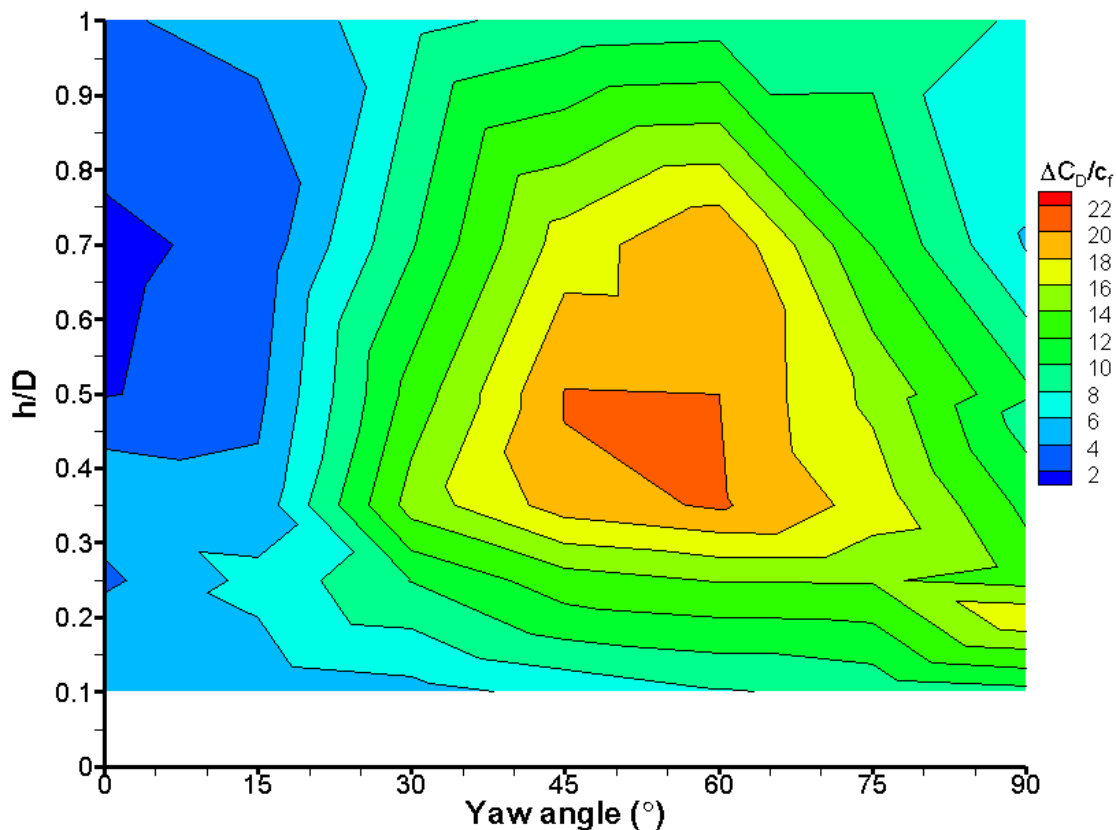
**Figure 5-21 Effect of yaw angle and depth on resulting normalized
drag coefficient (associated error ± 1.35)**

Dybenko (2005) associated the other small circular low pressure region on the sidewall of the circular cavity to a minor vortex tube, which terminated on the main captive vortex. This smaller vortex tube was not seen in the current study. The shear layer impingement also occurs in the same region for the two geometries. The asymmetric flow pattern is seen on the cavity base and ground plane in both figures. Similar trends were also seen in the data for 2:1 rectangular cavities with yaw 45°, h/D = 0.5 (Czech 2000). An asymmetric flow occurred which resulted in the maximum drag coefficient. Due to the square sides a direct comparison could not be made with the current experiment. These similarities all lead to the conclusion that this trailing vortex must be a key component to the increase in drag for these geometries.
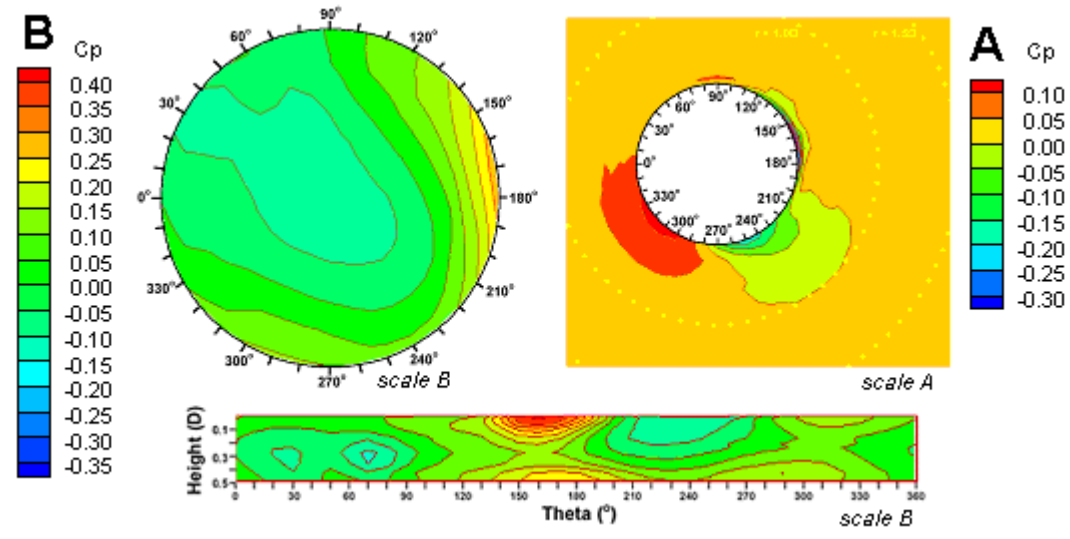
**Figure 5-22 Cp*mean* contours for circular cavities, h/D' = 0.47
(Dybenko 2005)**
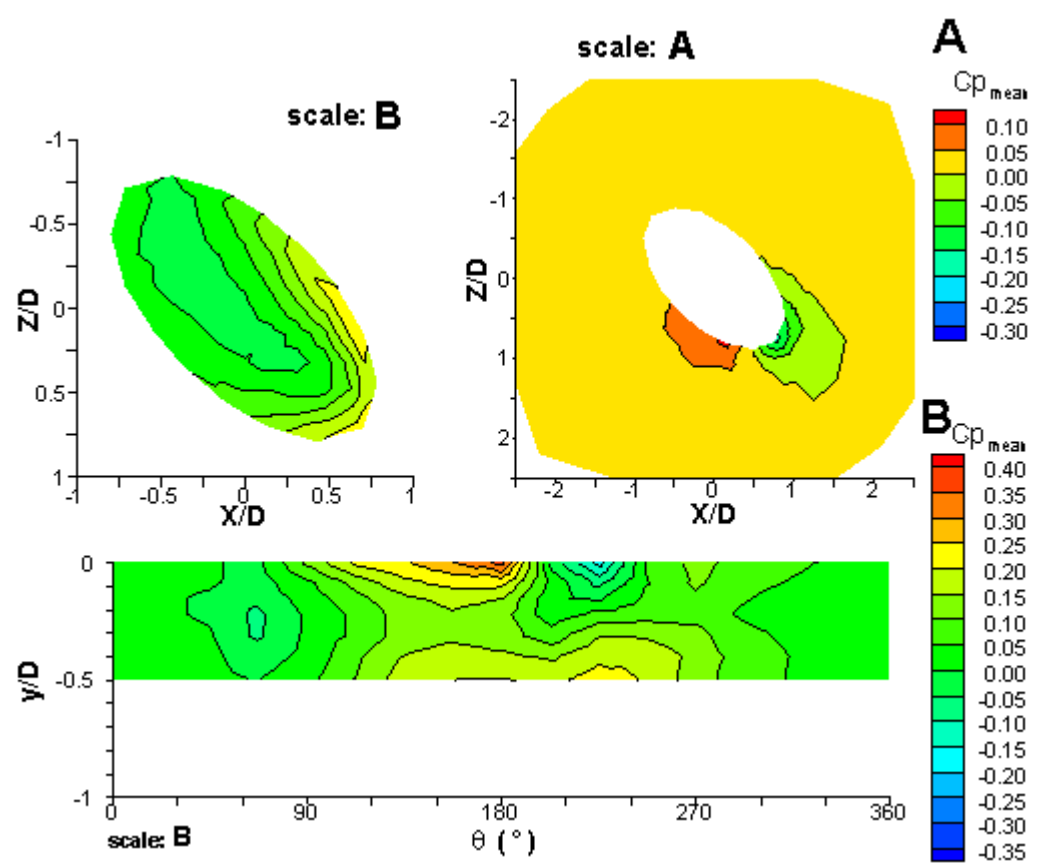
**Figure 5-23 Cp*mean* contours for yaw 45°, h/D = 0.5, cavity base
(top left), ground plane (top right), cavity sidewall (bottom)**

5.3.3   Lift of cavities

The resulting lift coefficients of the cavity configurations were compared to previous results for 2:1 rectangular cavities with h/D ratios of 0.5, as seen in Figure 5-24. Although similar trends are seen between the rectangular and elliptical cavities, the effect of the cavity was not clearly distinguished as the lift produced by the ground plane was not subtracted for these studies. Thus only a qualitative comparison can be made.
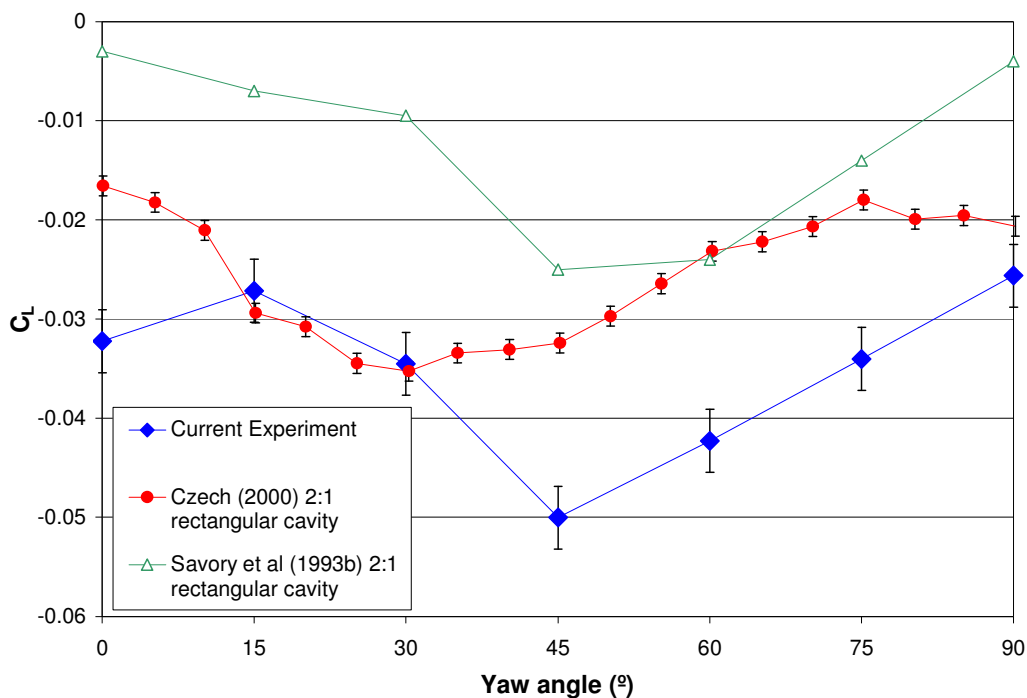
**Figure 5-24 The effect of yaw angle on the resulting lift coefficient
for h/D = 0.5 for varies types of cavities**

The effect of yaw angle and depth on the resulting net lift coefficient of the current experiment is shown in Figure 5-25. In the figure, the effect of the cavity is isolated as the lift coefficient of the ground plane is subtracted from the lift coefficient obtained with the cavity in place. Most of the lift coefficients are negative, indicating a force downward on the cavity base. The only configuration to experience a positive lift (upward force) was yaw 75°, h/D = 1.0 with a value of 0.002. The strongest downward force is seen for h/D' = 0.05 for a yaw angle of 90°. This is due to the large positive mean pressure seen on the cavity base, which creates a larger downward force than for the other cavity configurations. The lift is unaffected by yaw angle up to about 30° for

small h/D ratios. This is a result of the minor changes in the flow for these yaw angles, as described in Section 5.2.6.
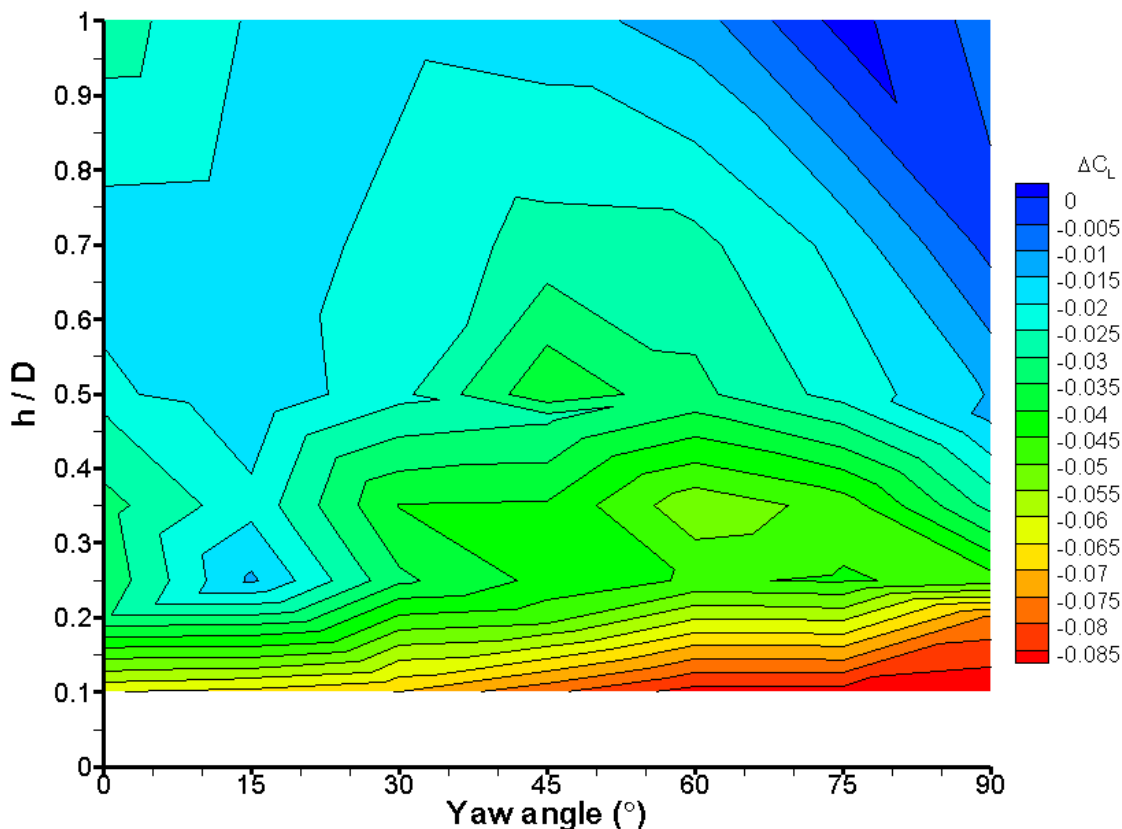
Figure 5-25 Effect of yaw angle and depth on resulting net cavity lift coefficient (associated error ± 0.00312)

5.4 Cavity oscillations

The previous section discussed the resulting flow regimes observed from changes in the mean and fluctuating pressure and velocity data, which were strongly dependent on yaw angle and cavity depth. The resulting drag and lift coefficient was also found to depend highly on the flow regime associated with each configuration.

In order to further understand the different flow regimes the existence of fluid dynamic and acoustic tones will be examined using frequency analysis. The identification of cavity feedback resonance is also vital, as it can dramatically increase the resulting drag of the cavity (McGregor and White, 1970).

The specific frequencies associated with the different cavity flow fields are discussed in the following section. Only cases with yaw angles of 0°, 45° and 90° with h/D = 0.2,0.5 and 0.7 were analysed as these corresponded to the configurations examined with the hot-wire equipment. Power spectral density (PSD) plots were created, which were then made non-dimensional with the corresponding freestream dynamic pressure or velocity.

5.4.1 Pressure fluctuations

Pressure fluctuations were first examined using the time series of the pressure transducers. Dominant frequencies were identified by creating power spectral density plots with bin resolution of 0.98 Hz for all the taps used in the measurements. Due to the frequency response of the pressure transducers the analysis was limited to a maximum of about 80 Hz. For each configuration a few selected taps along the cavity centreline (x-axis) are shown for each of the three surfaces of the experiment. For each configuration the residual noise of the tunnel is also plotted, which was located upstream and in the negative span wise direction from the centre of cavity on the ground plane. The resulting spectra for this tap is labelled "no cavity case" in the following figures.

For yaw 0° case, dominant frequencies were identified for the two deep cavities of h/D = 0.5 and 0.7. The dominant frequencies were 15.6 Hz and 9.8 Hz for the two depths, respectively. The PSD of each tap was normalized by their corresponding rms^2 pressure values in order to examine where these frequencies occur on the cavity walls. These peaks in the PSD do not correspond to any identifiable length scale of the cavity and were also not seen in the undisturbed ground plane surface pressure spectra.

There were also other peaks observed in the PSD spectra for the yaw 90° case. As for the yaw 0° case these frequencies were only seen in the data for h/D = 0.5 and 0.7. The dominant frequencies were 14.7 Hz for h/D = 0.5 and 11.7 Hz for h/D = 0.7. In a similar manner as for the yaw 0° case the normalized PSD values were plotted on the cavity walls, seen in Figure 5-27.
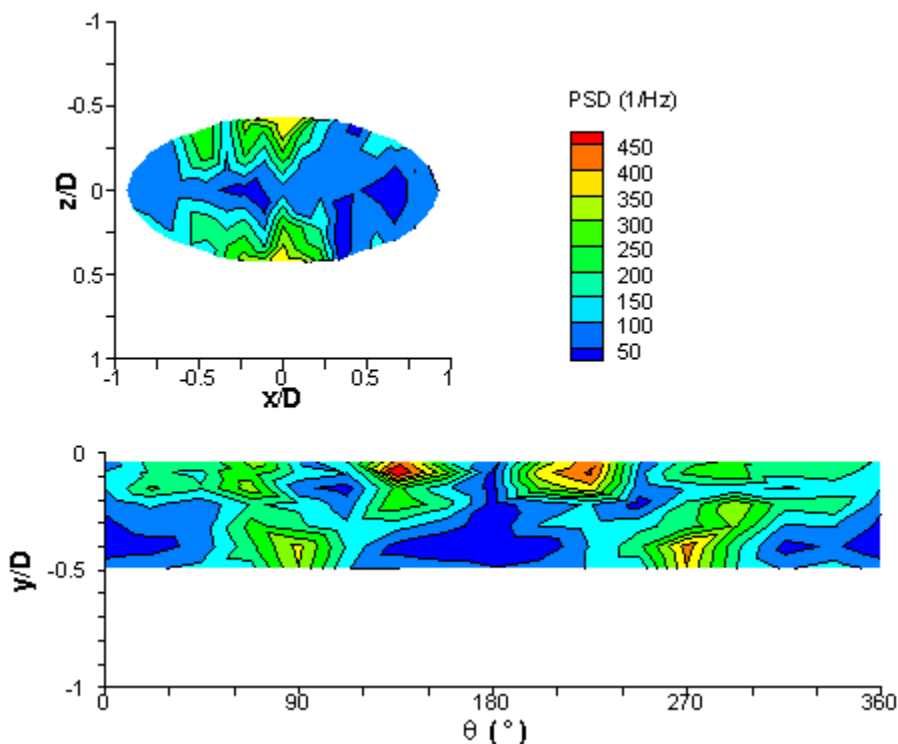
**Figure 5-26 Normalized PSD contours for 14.7 Hz for yaw 90° and
h/D = 0.5, cavity base (top), cavity sidewall (bottom)**

These frequencies must be a cause of the captive vortex observed in the cavity for these depths due to several important observations. First, these peak frequencies only occurred for deep cavities in which a captive vortex was observed in the mean pressure data. The shallowest cavity of h/D = 0.2, contained no dominant frequencies and also did not contain a captive vortex. Second, none of the depths at yaw 45° contained any of the dominant frequencies due to the non captive vortex exiting the cavity or not present for the shallow depth. Third, according to the contour plots of the normalized PSD, these frequencies were not observed in the impingement region of the separated shear layer. Thus, they can not be attributed to fluctuations associated with the separated shear layer. This is different from the frequencies observed by Czech (2000), between 15 and 45 Hz for rectangular cavities. Czech (2000) attributed these to fluctuations associated with the shear layer based upon near wall flow properties since they occurred at all yaw angles. Also for deep cavities the recirculation inside the cavity is steady compared to shallow cavities as noted by Ukeiley and Murray (2005). All these aspects indicate that these dominant frequencies are associated with captive vortex contained inside the cavity.

These dominant frequencies might be a result of the angular velocity associated with the captive vortex, as suggested by Ashcroft and Zhang (2005). Although, the angular velocity of the vortex may change across the span of the cavity due to vortex stretching. The angular velocity associated with the captive vortex could not be identified by the current experimental methods. A preliminary CFD study of the flows associated with circular cavities was undertaken by the use of FLUENT (Appendix D). The study modelled the flow parameters and cavity geometry associated with the work of Dybenko (2005), which was then used to validate the results of the steady state solution. The study used the same boundary layer and freestream values as the current investigation. Examining a plane along the centreline of the cavity of the numerical results, the time scale for a particle to circulate along a streamline within the cavity was found to be 0.032 s. This resulted in a frequency of approximately 31 Hz, which is higher than the dominant frequencies seen in the yaw 0° and 90° data. Thus, the frequencies are not a result of the recirculating flow inside the cavity and must be a cause of some other mechanism associated with the captive vortex.

To examine higher frequency pressure oscillations, time history from the microphone data was analysed. This was necessary due to the limited frequency response of the pressure transducers up to a maximum of approximately 80 Hz. As for the pressure transducer data, PSD plots of the microphone time series were generated. Although the microphones provided high frequency PSD data, there was no means to reliably calibrate them to corresponding pressure values, thus they could not be used to provide rms pressure values to compare to pressure transducer data. The PSD spectra of the microphones and pressure transducers could also not be correlated, as there was significant attenuation of the microphone data below approximately 200 Hz. This limit was well above the maximum 80 Hz frequency response range of the pressure transducers.

Once the PSD spectra were generated for the microphones they were compared to the fluctuations found in the tunnel without the cavity in place. This would allow distinct frequencies caused by the presence of the cavity to be identified. Table 5-1 summarizes the predicted resonance frequencies that might appear in the microphone data according to the different resonance mechanisms discussed in Section 2.4. For

standing wave resonance only the minor and major axis lengths were used in the calculations, although due to the curvature of the ellipse several different length scales might be present.

Table 5-1 Predicted frequencies by different resonance mechanisms

	Air column resonance (Equation 2-3): based on		Open end air column resonance (Equation 2-5) : based on		Rossiter's Equation (Rossiter 1966) (Equation 2-6)			Modified Rossiter equation (Block 1976) (Equation 2-7)		
yaw 0	**Predicted Frequency (Hz)**									
h/D	length	width	length	width	mode 1	mode 2	mode 3	mode 1	mode 2	mode 3
0.2	3259	1629	3259	2036	204	476	748	296	593	889
0.5	3259	1629	2037	1481	204	476	748	294	589	883
0.7	3259	1629	1629	1253	204	476	748	293	586	879
yaw 90	**Predicted Frequency (Hz)**									
h/D	length	width	length	width	mode 1	mode 2	mode 3	mode 1	mode 2	mode 3
0.2	1629	3259	2036	3259	102	238	374	147	295	442
0.5	1629	3259	1481	2037	102	238	374	145	291	436
0.7	1629	3259	1253	1629	102	238	374	144	288	433

For all the yaw angles examined the PSD plots showed qualitatively similar results to the Cp_{rms} distributions. Higher PSD values are seen from about 50 to 650Hz in regions where high Cp_{rms} values are also found on the cavity walls near the lip around $\theta = 180°$ on the sidewall and in the downstream region of the cavity base. Figure 5-27 is representative of the increase in fluctuations in regions of predicted shear layer impingement. The figure shows the PSD spectra of the acquired voltages which were normalized by the rms^2 of the fluctuations for yaw 90°, h/D = 0.2. The location of the microphones is shown in the figure. The pink curve is the PSD spectra associated with the most upstream microphone location on the cavity base. This microphone did not pick up any shear layer fluctuations, as it closely resembled the no cavity case spectra. Since the location of these higher PSD values was similar to shear layer impingement locations, these large broadband fluctuations seem to be caused by the separated shear layer, which is drawn into the cavity and are not associated with any cavity generated frequencies. This was also seen for h/D = 0.5 and 0.7 as the PSD amplitude was much larger for microphones located in the downstream region of the cavity near the lip.
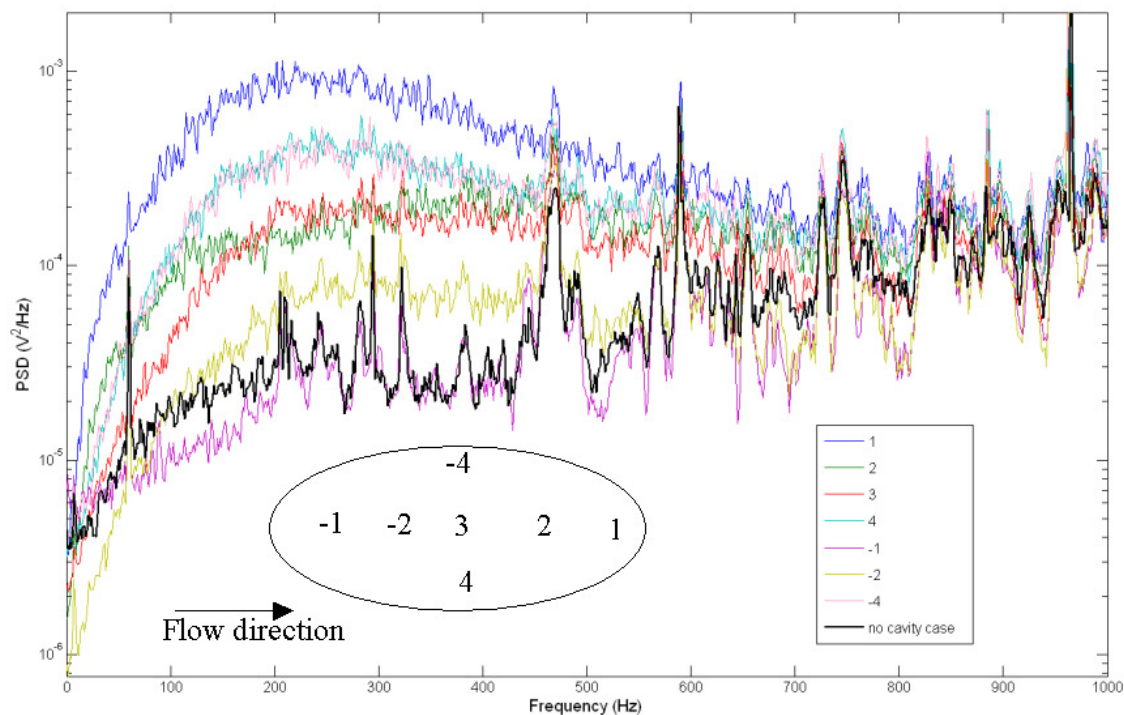
**Figure 5-27 Normalized PSD spectra for microphone data on the
cavity base for yaw 90°, h/D = 0.2**

In order to examine any specific frequencies the furthest upstream microphone on the base was compare to the PSD plot without the cavity in place. This location on the base contained the smallest broadband amplitude and, thus, provided a good plot to compare to the no cavity case oscillations. Table 5-2 summarize the peaks in the PSD spectra, which are not observed for the no cavity case for each yaw angle examined.

The frequencies associated with the cavity feedback resonance and predicted by Rossiter's (1966) and Block's (1976) modified Rossiter equation was not observed for any of the cavity configurations. This is an expected outcome as there are several flow and geometry configurations, which are not met in order for feedback resonance to occur. The three most important factors not satisfied by the current experiment for cavity feedback resonance are: a thin upstream boundary layer, high velocity (above M = 0.2) and a straight upstream cavity edge perpendicular to the flow direction. Ahuja and Mendoza (1995) noticed that at M = 0.4 all cavity feedback resonance was suppressed for δ/L > 0.066. In the current experiment δ/D = 1.08 for yaw 0° cavities and δ/D = 0.54 for

yaw 90° cavities, which was much larger than the value found by Ahuja and Mendoza (1995).

As mentioned by East (1966), a transition occurs from cavity feedback resonance to depth mode resonance at approximately M = 0.2. Depth mode resonance is not observed for shallow cavities, but a peak at 1252 Hz is observed for h/D = 0.7 yaw 0° which corresponds very well with the predicted value of 1253 Hz. Although this frequency is not observed for the same depth at the other yaw angles, as for the yaw 90° case a small broadband peak is seen around this frequency and for the 45° case the peak is missing completely. This indicates that this peak is yaw dependent and therefore could not be the depth mode resonance.

Table 5-2 Frequencies which are not observed in the no cavity case

	Yaw angle 0				**Yaw angle 45**		
h/D	0.2	0.5	0.7	**h/D**	0.2	0.5	0.7
	Frequency Peak (Hz)				**Frequency Peak (Hz)**		
	1722	883	886		1722	885	887
		981	988.8			981	980-991
		988	1005			998	1005
		1001	1025			1002	1027
		1595	1187			1005	1208-1222
		1624	1208-1221			1595	1239
			1235-1248			1625	1295
			1252				1320
			1296				1364-1403
			1317				1476
			1361				1532-1558
			1526-1556				1603
			1602				

	Yaw angle 90		
h/D	0.2	0.5	0.7
	Frequency Peak (Hz)		
	1611	886	886
	1722	981	979
		988	987
		1003	1002
		1597	1024-1028
		1624	1042
			1208-1223
			1235-1255
			1320-1326
			1364-1385
			1475
			1531-1558
			1603

The depth mode resonance formula, Equation 2-5, has an end correction based on experimental results applied to it. Depending on the accuracy of the end correction, the peak at 1282 Hz, seen in all the yaw angles for h/D = 0.7, could also correspond to depth mode resonance. Equation 2-4 is based on an air column with a constant diameter. The current ellipse has a range of length scales associated with it when examining an appropriate diameter length. Therefore, the end correction might not be appropriate for the current geometry. Thus, this peak seen in all three yaw angles may be the depth mode associated with h/D = 0.7, since it does not appear to be yaw dependent. None of the other depths displayed any similar trends, therefore depth mode resonance was only observed for deep cavities.

Finally the curvature of the elliptical planform shape did not have a significant effect on the PSD plots. Block (1976) observed that circular cavities displayed no distinct resonant frequencies but showed more broadband amplitudes over a wide range of frequencies compared to square cavities with the same dimensions. This was not evident in the current experiment, as even by altering the yaw angle the PSD plots did not change much. This is unexpected as there is a significant difference between the upstream wall radius of curvature of a yaw 0° and yaw 90° cavity.

5.4.2   Wake Velocity fluctuations

The identification of specific dominant frequencies in the hot-wire time series data was conducted in a similar manner as the pressure fluctuations. The dominant frequencies seen in the pressure data associated with deep cavities for yaw angles of 0° and 90° could not be examined with the hot-wire equipment. This is due to the experimental setup of the hot-wire system, which was mounted on the roof of the wind tunnel and contained a long traversing rod into the wind tunnel. Dominant frequencies were found at approximately 7.2Hz and 14.7 Hz in the hot-wire time series. These dominant frequencies were independent of cavity geometry and velocity as they were seen at the same frequency even close to the ground plane. A simple examination of the natural frequencies associated with the mounting mechanism, including the rod, showed that these frequencies were due to an oscillation set up along the entire mounting

mechanism. A gentle impact test showed similar dominant frequencies in the PSD data of the hot-wires.

For the yaw angles of 0° and 90°, no other dominant frequencies are seen in the time series of the hot-wire measurements beside the frequencies associated with the vibration of the hot-wire mounting setup. This was not the case for deep cavities, h/D = 0.5 and 0.7 yawed to 45°.   For these configurations a broadband amplitude in the PSD data centred at approximately 215 Hz is seen at some locations in the wake in the streamwise velocity. The location of this broadband amplitude corresponds to the location of the trailing vortex where high velocity fluctuations are also observed. A few selected points were chosen for comparison and the PSD values were normalized by the rms^2 of the streamwise velocity (u) is shown in Figure 5-28.   The location of the points in the wake profile at the downstream cavity lip is shown in Figure 5-29.

As seen in Figure 5-29, the location of this broadband fluctuation which corresponds quite well with the trailing vortex configuration discussed in Section 5.2.6. The increased turbulence in all three velocity components seems to indicate that these broadband amplitudes in frequencies are associated with the increased turbulence in this area. Dybenko (2005) also noticed a broadband oscillation for circular cavities at depth to diameter ratio of 0.47 centred around 150 Hz, where a trailing vortex configuration was also present.
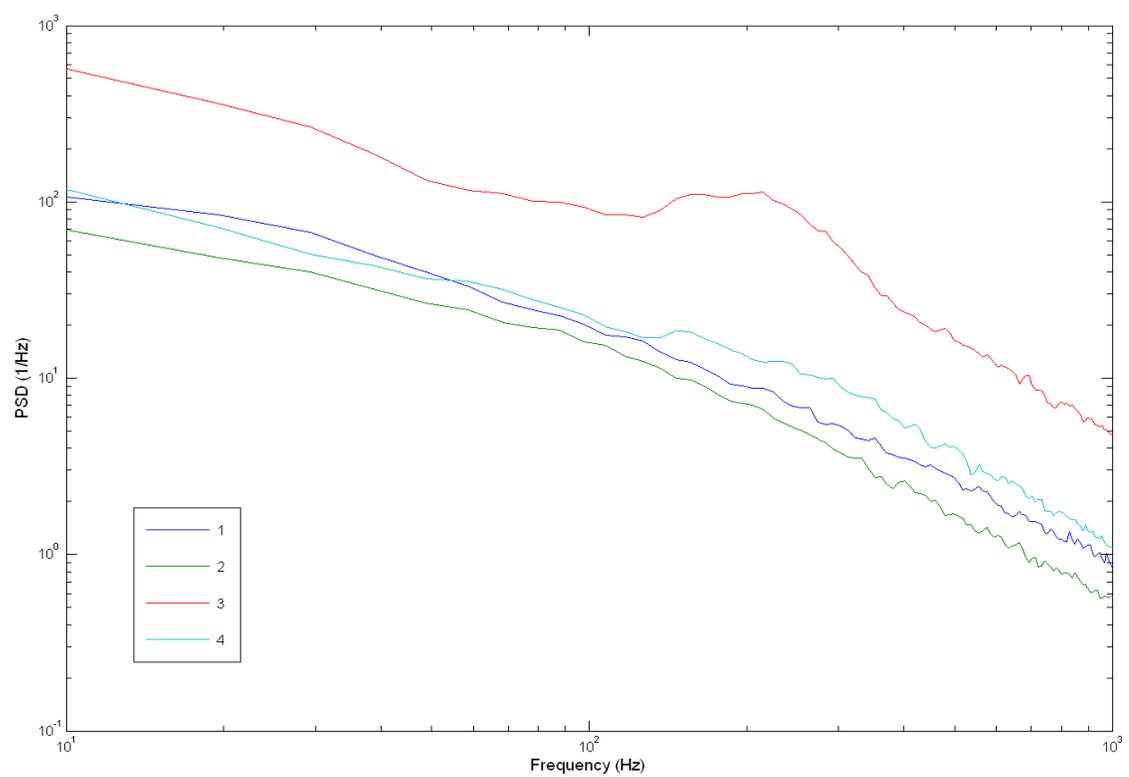
Figure 5-28 PSD normalized by (u')² for streamwise velocity fluctuations at x/D = 0.7 for yaw 45°, h/D = 0.5
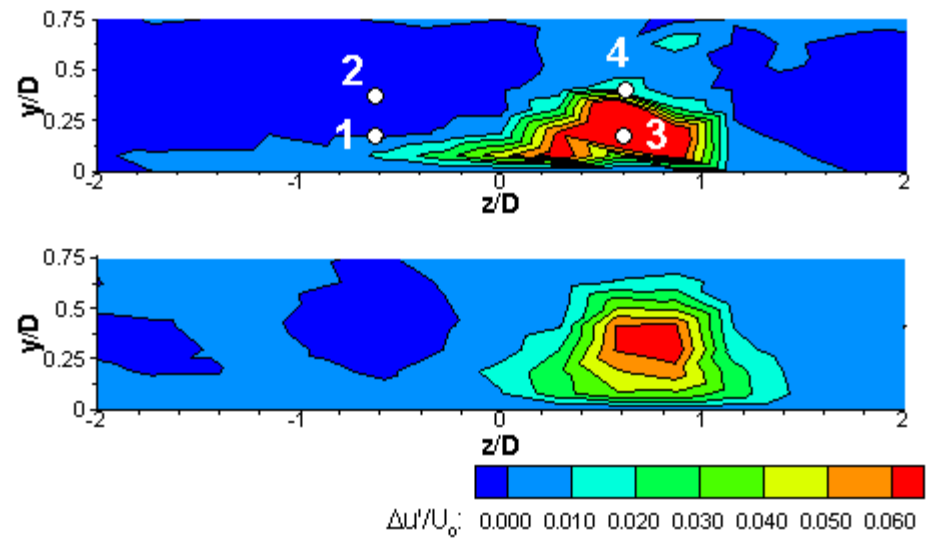

Figure 5-29 Streamwise velocity fluctuations for yaw 45°, h/D = 0.5

5.5 Summary

The previous sections outlined the basic flow patterns associated with yawed elliptical cavities. The flow regimes were determined mainly from the resulting mean pressure data on the cavity surfaces and surrounding ground plane. The flow regimes are very similar to those which occur for rectangular cavities. The classic definition of cavity flow types can be applied to some of the yaw angles and depths examined here. For very deep and shallow cavities the yaw angle has a negligible effect on the resulting flow.

An asymmetric flow pattern occurs for certain yawed cavities and results in an increase in drag. Maximum drag occurs for cavities at yaw 45° to 60° and depths around $h/D \approx 0.5$. For this configuration a strong resemblance is seen in the pressure contours to circular cavities during maximum drag, when h/D is also approximately 0.5. The resemblance confirms that the trailing vortex and the asymmetric flow pattern is a key component in creating a large increase in the resulting drag. The effect of yaw and depth on the resulting drag coefficient closely resembles the trends seen for rectangular cavities, where maximum drag also occurred at similar depths and yaw angle.

The lift coefficient indicates a downward force for most of the cavity configurations examined. The maximum drag and minimum lift do not occur for the same cavity configuration, which may be helpful in design considerations. Not much change is observed in the lift and the drag coefficient for yaw angles less than 30° for shallow cavities.

Specific dominant frequencies were observed in the pressure field inside the cavity for certain cavity configurations, which could not be attributed to any length scales associated with the cavity or to fluctuations in the shear layer. These frequencies were only observed for open type cavities aligned or normal to the flow. Thus, the frequencies must be somehow related to the captive vortex contained inside the cavity for these configurations.

Broadband peaks in frequency were observed inside the trailing vortex for the 45° yawed cavity. This has been attributed to the increase in turbulence in this region. This amplitude in a broad number of frequencies has also been observed for other trailing vortex flows in circular cavities.

6 Conclusions and recommendations

This chapter outlines the principal conclusions from the present work and discuses areas for further research.

6.1 Conclusions

The main aim of the present study was to examine the resulting flow types of yawed elliptical cavities with varying depths and relate them to flow regimes associated with cavities of circular and rectangular planforms. The resulting flow patterns were grouped into different flow regimes, which varied with yaw angle and cavity depth. These regimes were very similar to those found for yawed rectangular cavities. The resulting drag and lift coefficients also varied in a similar manner with yaw and depth as rectangular cavities. This provided further support to the hypothesis that the flow regimes were similar and the effect of the wall radius of curvature has negligible effects on the resulting flow regimes.

For very shallow (h/D = 0.1) and deep cavities (h/D = 1.0) the effect of yaw angle was negligible. The results of the current investigation showed that for deep cavities a large stable vortex was evident in the cavity middle with low fluctuations compared to the other flow types. This configuration also resulted in low drag and a low negative lift coefficient. Similar conclusions could be drawn from very shallow cavities. Their resulting drag was also low compared to other cavity configurations although the lift associated with these cavities was the lowest of all the configurations examined. The resulting low lift was a result of the shear layer dipping into the cavity and causing a higher pressure region on the cavity base compared to deep cavities.

Cavities with their major axis aligned with the flow (yaw 90°) were nominally two-dimensional. The resulting flow types with varying depths were very similar to two-dimensional rectangular cavities and a direct comparison to open and closed type cavities could be made. The stable vortex was formed in the cavity at similar h/D ratios as also observed for rectangular cavities. A symmetric flow pattern was observed for all depths and the resulting drag was highly dependent on the cavity depth. Deep cavities were

associated with low drag and low negative lift coefficients. Distinct frequencies were observed for deep cavities of this regime, which appeared to be linked to fluctuations associated with the captive vortex contained in the cavity.

For Cavities normal to the flow (yaw 0°), the flow again resembled rectangular cavities as cellular structures were observed along the span of the cavity. This was also the only flow type, which contained two initial shear layer impingement points on the cavity sidewall. The streamwise length for this configuration was small compared to the yaw 90° case and thus most of the shear layer spanned the cavity opening. This resulted in lower impingement pressure, which lead to lower drag coefficients. The lift coefficient was also not as low as for the yaw 90° case. Dominant frequencies at similar depths were also found for this regime as for the yaw 90° case. The cause of these dominant frequencies also appeared to be the captive vortex contained across the span of the cavity.

The effect of yawing the cavity to yaw 15° resulted in only minor changes compared to the yaw 0° cases. Only one initial shear layer impingement region was observed compared to two in the yaw 0° case. The captive vortex was aligned along the major axis of the cavity and, thus, resulted in a weak asymmetric flow regime.

For larger yaw angles a trailing vortex configuration was observed for certain depths. Shear layer entrainment into the cavity resulted in a high pressure region on the cavity base, which forced the captive vortex out of the cavity near the downstream region of the sidewall. This caused a large velocity defect compared to the other configurations. The presence of the trailing vortex also resulted in high drag. This trailing vortex configuration was very similar to the flow regime found for asymmetric circular cavity flow also associated with high drag.

The trailing vortex was associated with broadband fluctuations due to the increased turbulence inside the wake of the cavity.

Cavity feedback resonance was not observed for any of the configurations examined mostly due to the low velocity thick boundary layer. Depth mode resonance was also only observed for deep cavities, $h/D = 0.7$. For the trailing vortex configuration, a large broadband peak centred around approximately 215 Hz in the frequency spectra of the streamwise velocity, was attributed to the large increase in turbulence in this region.

The results of this work were also useful in providing an extensive data set of flow quantities in identifying the effects of depth and yaw angle on the flow field and resulting drag and lift of elliptical cavities.

6.2 Recommendations for further work

- Similar experiments should be conducted for deeper cavities beyond the range examined in the present study. The use of deeper cavities may lead to identifying the exact limiting depth for yaw independence in deep cavities.

- In a similar manner, wake profiles using hot-wire anemometry should be conducted for the shallow cavities in order to examine the velocity defects and fluctuations associated with this depth. Examining the shallow cavities may lead to a better understanding of the how the shear layer flows over the downstream cavity lip and creates the negative pressure region associated with the recirculating field.

- PIV measurements of the resulting flow field inside cavities with thick boundary layers have not been examined in any of the literature found. This may be useful in establishing an effective recirculation velocity associated with the captive vortex for certain depths, as it is driven by the shear layer spanning the cavity.

- Flow visualization techniques or PIV measurements may also be helpful in identifying the cell structures for the yaw 0° case. Such techniques may also allow an examination of the effect of aspect ratio on the number of cells, as has been previously established for rectangular cavities.

- Establishing ways to eliminate the trailing vortex for the asymmetric flows may prove helpful in drag reduction. Placing the cavity base on an angle compared to the ground plane may prove to be helpful in keeping the stable vortex inside the cavity for the specific depths.

References

Adams E W, Johnston J P (1988) Effects of the separating shear layer reattachment flow structure Part1: Pressure and turbulence quantities. J Experiments in Fluids 6 (7) : 400-408

Ahuja K K, Mendoza J (1995) Effects of cavity dimensions, boundary layer and temperature on cavity noise with emphasis on benchmark data to validate computational aeroacoustic codes. NASA CR 4653

Ashcroft G, Zhang X (2005) Vortical structures over rectangular cavities at low speed. Physics of Fluids 17(1) : 1-8

Block P J W (1976) Noise response of cavities of varying dimensions at subsonic speeds. NASA TN D-8351

Cattafesta L, Garg S, Choudhari M, Li F (1997) Active control of flow-induced cavity resonance. 28th Fluid Dynamics Conf, Snowmass Village CO, AIAA 97-1804

Cattafesta L, Williams D, Rowley C, Alvi F (2003) Review of active control of flow-induced cavity resonance. 33rd AIAA Fluid Dynamics Conf, Orlando FL,
AIAA 2003-3567

Charwat A F, Roos J N, Dewey Jr. F C, Hitz J A (1961) Investigation of separated flows, Part I: The pressure field. J Aerospace Science 28(6-7) : 457-470

Colonius T (2001) An overview of simulation, modeling and active control of flow/acoustic resonance in open cavities. 39th Aerospace Science Meeting, Reno NV,
AIAA 2001-0076

Czech M (2000) The acoustics and aerodynamics of turbulent flow over yawed, rectangular cavities. University of Surrey, PhD Thesis

Dubief Y, Delcayre F (2000) On coherent-vortex identification in turbulence.
J Turbulence 1 : Article 011

Dybenko J (2005) An experimental investigation of turbulent boundary layer flow over surface mounted circular cavities. University of Western Ontario, Master's Thesis

East L F (1966) Aerodynamically induced resonance in rectangular cavities.
J Sound and Vibration 3(3) : 277-287

ESDU (2004) Aerodynamics and aero-acoustics of rectangular planform cavities.
Part I: Time-averaged flow. Data Item 02008, ESDU International

ESDU (2005) Aerodynamics and aero-acoustics of rectangular planform cavities.
Part II: Unsteady flow and aero-acoustics. Data Item 04023, ESDU International

Friesing H (1936) Measurement of the drag associated with recessed surfaces: cut-outs of rectangular and elliptical planform. ZWBFB 628 (RAE Library Translation 1614, 1971)

Gaudet L, Winter K G (1973) Measurements of the drag of some characteristic aircraft excrescences immersed in turbulent boundary layers. R.A.E. Technical Memorandum Aero

Geveci M, Oshkai P, Rockwell D, Lin J C, Pollack M (2003) Imaging of self-excited oscillations of flow past a cavity during generation of a flow tone. J Fluids and Structures 18 : 665-694

Gharib M, Roshko A (1987) The effect of flow oscillations on cavity drag. J Fluid Mechanics 177 : 501-530

Grace S M, Dewar W G, Wroblewski D E (2004) Experimental investigation of the characteristics within a shallow wall cavity for both laminar and turbulent boundary layers. Experiments in Fluids 36 : 791-804

Hamed A, Das K, Basu D (2004) Numerical simulations of fluidic control for transonic cavity flows. 42nd Aerospace Science Meeting, Reno NV, AIAA 2004-0429

Hankey W L, Shang J S (1980) Analysis of pressure oscillations in an open cavity. AIAA J 18(8) : 892-898

Hiwada M, Kawamura T, Mabuchi I, Kumada M (1983) Some characteristics of flow pattern and heat transfer past a circular cylindrical cavity. Bulletin of the JSME 26(220) : 1744-1752

Hoerner S F (1965) Fluid-dynamic drag: Practical information on aerodynamic drag and hydrodynamic resistance. Midland Park, New Jersey, USA

Jeong J, Hussain F (1995) On the identification of a vortex. J Fluid Mechanics 285 : 69-94

Jorgensen F (2002) How to measure turbulence with hot-wire anemometers – a practical guide. Dantec Dynamics publication no. 9040U6151.

King L V (1914) On the convection of heat from small cylinders in a stream of fluid: Determination of the convection constants of small platinum wires with application to hot-wire anemometry. Philosophical Transactions of the Royal Society of London, Series A, 214 : 373-432

Krishnamurty K (1955) Acoustic radiation from two-dimensional rectangular cutouts in aerodynamic surfaces. NACA TN 3487

Lancaster P, Salkauskas K (1986) Curve fitting and surface fitting: an introduction. Toronto, Academic Press

Lin J C, Rockwell D (2001) Organized oscillations of initially turbulent flow past a cavity. AIAA J 39(6) : 1139-1151

Lin W E (2005) Large-scale physical simulation of a microburst outflow using a slot jet. University of Western Ontario, Master's Thesis.

Maull D J, East L F (1963) Three-dimensional flow in cavities. J Fluid Mechanics 16 : 620-632

McGregor O W, White R A (1970) Drag of rectangular cavities in supersonic and transonic flow including the effects of cavity resonance. AIAA J 8(11) : 1959-1964

Panteny D J (2001) Aerodynamics of cavities. Final year project report at the University of Loughborough

Plentovich E B (1990) Three-Dimensional cavity flow fields at subsonic and transonic speeds. NASA TM 4209

Plentovich E B, Stallings R L, Tracy M B (1993) Experimental cavity pressure measurements at subsonic and transonic speeds. NASA TP 3358

Rizzetta D P, Visbal M R (2003) Large-eddy simulation of supersonic cavity flowfields including flow control. AIAA J 41(8) : 1452-1462

Rockwell D, Naudascher E (1978) Review – Self-Sustaining Oscillations of Flow Past Cavities.   J Fluids Engineering 100 : 152-165

Roshko A (1955) Some measurement of flow in a rectangular cutout. NACA TN 3488

Rossiter J E (1964) Wind-Tunnel Experiment on the Flow over Rectangular Cavities at Subsonic and Transonic Speeds. British ARC R&M no. 3428

Rowley C W, Juttijudata V, Williams D R (2005) Cavity flow control simulations and experiments. 43rd AIAA Aerospace Sciences Meeting, Reno NV, AIAA 2005-0292

Sarno R L, Franke M E (1994) Suppression of flow-induced pressure oscillations in cavities. J Aircraft 31(1) : 90-96

Savory E, Toy N (1993a) The flows associated with elliptical cavities. Symposium on Separated Flows, ASME Fluids Engng Conf, Washington DC, FED 149 : 95-103

Savory E, Toy N, Disimile P, Dimicco R (1993b)   The drag of three-dimensional rectangular cavities. J Applied Scientific Research 50 : 325-346

Savory E, Toy N, Gaudet L (1996) Effect of lip configuration on the drag of a circular cavity. Emerging Techniques in Drag Reduction, Mechanical Engineering Publications Ltd 317-335

Sen S N (1990) Acoustics: Waves and Oscillations. Wiley Eastern Ltd., New Delhi, India.

Stallings Jr. R L, Wilcox Jr. F J (1987) Experimental cavity pressure distributions at supersonic speeds. NASA TP 2683.

Tam K W, Block P J W (1978) On the tones and pressure oscillations induced by flow over rectangular cavities. J Fluid Mechanics 89(2) : 373-399

Tani I, Iuchi M, Komoda H (1961) Experimental investigation of flow separation associated with a step or a groove. Aero. Research Institute, Tokyo Univ. Rep. No. 364

Tillman W (1951) Additional measurements of the drag of surface irregularities in turbulent boundary layers. NACA TM 1299 (Translation of ZWB Untersuchungen und Mitteilungen Nr. 6619, 1944)

Tracy M B, Plentovich E B, Chu J (1992) Measurements of fluctuating pressure in a rectangular cavity in transonic flow at high Reynolds numbers. NASA TM 4363

Tracy M B, Plentovich E B (1993) Characterization of cavity flow fields using pressure data obtained in the Langley 0.3-meter transonic cryogenic tunnel. NASA TM 4436

Ukeiley L, Ponton M, Seiner J, Jansen B (2003) Suppression of pressure loads in resonating cavities through blowing. 41st Aerospace Science Meeting, Reno NV, AIAA 2003-0181

Ukeiley L, Murray N (2005) Velocity and surface pressure measurements in an open cavity. Experiments in Fluids 38 : 656-671

Wheeler A, Ganji A (1996) Introduction to Engineering Experimentation, 2nd edition, Prentice Hall Inc, NJ

Lin W E (2005) Large-scale physical simulation of a microburst outflow using a slot jet. University of Western Ontario, Master's Thesis

Young A D, Paterson J H (1981) (Jones J L, editor) Aircraft Excrescence Drag. NATO AGARD-AG-264